

## Supplementary Material for

### **Lattice light-sheet microscopy: Imaging molecules to embryos at high spatiotemporal resolution**

Bi-Chang Chen, Wesley R. Legant, Kai Wang, Lin Shao, Daniel E. Milkie, Michael W. Davidson, Chris Janetopoulos, Xufeng S. Wu, John A. Hammer III, Zhe Liu, Brian P. English, Yuko Mimori-Kiyosue, Daniel P. Romero, Alex T. Ritter, Jennifer Lippincott-Schwartz, Lillian Fritz-Laylin, R. Dyche Mullins, Diana M. Mitchell, Joshua N. Bembeneck, Anne-Cecile Reymann, Ralph Böhme, Stephan W. Grill, Jennifer T. Wang, Geraldine Seydoux, U. Serdar Tulu, Daniel P. Kiehart, Eric Betzig\*

\*Corresponding author. E-mail: betzige@janelia.hhmi.org

Published 24 October 2014, *Science* **346**, 1257998 (2014)  
DOI: 10.1126/science.1257998

**This PDF file includes:**

Supplementary Text

Figs. S1 to S26

Table S1

Full Reference List

**Other Supplementary Material for this manuscript includes the following:**  
(available at [www.sciencemag.org/content/346/6208/1257998/suppl/DC1](http://www.sciencemag.org/content/346/6208/1257998/suppl/DC1))

Movies S1 to S18

**Contents: Lattice Light Sheet Microscopy Supplementary Material**

<u>Section</u>	<u>Page</u>
Supplementary Notes	
1. Theoretical Relationships between Bessel Beams and 2D Optical Lattices.....	3
2. Calculating the SLM Pattern That Generates the Desired Lattice Light Sheet.....	9
3. Detailed Optical Path.....	12
4. SLM Operation.....	13
5. Sample Preparation.....	14
Supplementary Figures.....	19
Supplementary Table.....	42
Captions for Supplementary Movies.....	46
Full Reference List.....	64

## SUPPLEMENTARY NOTES

### 1. Theoretical Relationships between Bessel Beams and 2D Optical Lattices

#### a. Non-diffracting beams

The electric field  $\mathbf{e}(\mathbf{x},t)$  of any continuous-wave, coherent light beam of free-space wavelength  $\lambda_o$  propagating in a homogeneous medium of real refractive index  $n$  can be decomposed into a sum or integral over the electric fields  $\mathbf{e}_n$  of a set of planes waves propagating in various directions defined by their wavevectors  $\mathbf{k}_n$ :

$$\mathbf{e}(\mathbf{x},t) = \sum_{n=1}^N \mathbf{e}_n \exp[i(\mathbf{k}_n \cdot \mathbf{x} - \omega t)] \quad (1)$$

where  $\omega = 2\pi c / \lambda$ ,  $\lambda = \lambda_o / n$  is the wavelength in the medium, and  $c$  is the speed of light.

In the special case where all the wavevectors  $\mathbf{k}_n$  lie on the surface of a single cone (fig. S1A),  $\mathbf{k}_n \cdot \hat{\mathbf{e}}_y = k \cos \theta \quad \forall n$  where  $k = 2\pi / \lambda$  and the  $y$  axis is defined as the axis of the cone, which has a half-angle of  $\theta$ . Hence, Eq. 1 becomes:

$$\mathbf{e}(\mathbf{x},t) = \exp[i(ky \cos \theta - \omega t)] \sum_{n=1}^N \mathbf{e}_n \exp[i((k_x)_n x + (k_z)_n z)] = \mathbf{e}(x,z) \exp[i(ky \cos \theta - \omega t)] \quad (2)$$

In other words, the electric field of the light beam propagates in the  $y$  direction without any change in its spatial distribution or amplitude in the  $xz$  plane. Such a beam is termed *non-diffracting*. The constraint that all the wavevectors lie on a cone is equivalent to the constraint that the light entering the objective lens used to create the cone is confined to points on an infinitesimally thin ring in the rear pupil of the lens.

#### b. Bessel beams

Now additionally assume that the rear pupil is illuminated with a uniform, infinitesimally thin ring of light of constant phase and uniform polarization  $\mathbf{e}$ . The cone is then filled with a continuum of wavevectors, so in the scalar approximation Eq. 2 becomes:

$$\mathbf{e}(\mathbf{x},t) = A \mathbf{e} \exp[i(ky \cos \theta - \omega t)] \int_0^{2\pi} \exp[i k \sin \theta (x \sin \phi + z \cos \phi)] d\phi \quad (3)$$

where we have used  $\mathbf{k} = k \sin \theta \sin \phi \hat{\mathbf{e}}_x + k \cos \theta \hat{\mathbf{e}}_y + k \sin \theta \cos \phi \hat{\mathbf{e}}_z$  in spherical coordinates. If we also express  $\mathbf{x} = \rho \sin \phi' \hat{\mathbf{e}}_x + y \hat{\mathbf{e}}_y + \rho \cos \phi' \hat{\mathbf{e}}_z$ ,  $\rho = \sqrt{x^2 + z^2}$  in cylindrical coordinates, we get:

$$\mathbf{e}(\mathbf{x}, t) = A \mathbf{e} \exp[i(ky \cos \theta - \omega t)] \int_0^{2\pi} \exp[i k \rho \sin \theta (\sin \phi \sin \phi' + \cos \phi \cos \phi')] d\phi \quad (4)$$

or, with the aid of the trigonometric identity  $\sin \phi \sin \phi' + \cos \phi \cos \phi' = \cos(\phi - \phi')$ :

$$\mathbf{e}(\mathbf{x}, t) = A \mathbf{e} \exp[i(ky \cos \theta - \omega t)] \int_0^{2\pi} \exp[i k \rho \sin \theta \cos(\phi - \phi')] d\phi \quad (5)$$

We recognize the expression at right as the integral representation of the Bessel function of the first kind of order zero:

$$J_o(\alpha) = \frac{1}{2\pi} \int_0^{2\pi} \exp(i\alpha \cos \phi) d\phi \quad (6)$$

And thus we conclude:

$$\mathbf{e}(\mathbf{x}, t) = \mathbf{e}(\rho, y, t) = \frac{A}{2\pi} \mathbf{e} J_o(k \rho \sin \theta) \exp[i(ky \cos \theta - \omega t)] \quad (7)$$

In other words, a uniform ring of illumination in the rear pupil of an objective lens produces a non-diffracting light beam propagating along the axis of the lens and having an electric field whose amplitude in any plane transverse to this axis is described by the circularly symmetric Bessel function  $J_o(k \rho \sin \theta)$ . This is termed a *Bessel beam* (59). The size of the pattern scales linearly with the wavelength  $\lambda$  and inversely with the numerical aperture  $NA = n \sin \theta$ .

The more rigorous vector field of a Bessel beam can be approximated by subtracting the vector fields of two focused beams produced by uniform illumination (60) at the rear pupil at two slightly different numerical apertures. The electric field consists of a narrow central peak surrounded by an infinite series of concentric side lobes of opposite phase and decreasing amplitude (fig. S24). The narrow peak and infinite extent of an ideal Bessel beam make it an attractive candidate for light sheet microscopy, wherein the beam is scanned across the focal plane defined by an orthogonal detection objective.

### c. Two-dimensional optical lattices

Now instead consider a non-diffracting beam of the form of Eq. 2 where  $\mathbf{e}(x, z)$  is periodic in two-dimensions:

$$\mathbf{e}(\mathbf{x}, t) = \mathbf{e}(\mathbf{x} + m_1 \mathbf{a}_1 + m_2 \mathbf{a}_2, t) \quad (8)$$

where  $m_1, m_2$  can be any integer and  $\mathbf{a}_1, \mathbf{a}_2$  are two-dimensional *primitive vectors* that define the periodic pattern. There are only five such patterns of unique symmetry in 2D, termed *Bravais lattices*. A non-diffracting light beam having the cross-sectional symmetry of a 2D Bravais lattice is termed a 2D *optical lattice*. A 2D optical lattice is comprised of a minimum of three wavevectors  $\mathbf{k}_n$ , all of which must lie on the surface of a single cone (12), (fig. S1A). Note from

Eq. 1 that the spatial dependence of the lattice electric field is separable from the polarizations  $\mathbf{e}_n$  of its constituent plane waves, and thus the symmetry and periodicity of the lattice depends only on the  $\mathbf{k}_n$ , whereas the electric field pattern that repeats in every unit cell of the lattice depends on both the  $\mathbf{k}_n$  and the  $\mathbf{e}_n$  (12).

Multiple pairs of primitive vectors can be used to define a 2D lattice of given parameters (i.e., Bravais symmetry and, where appropriate, aspect ratio and angle). For each such pair, a wavevector set  $\{\mathbf{k}_1, \mathbf{k}_2, \mathbf{k}_3\}$  can be found that yields an optical lattice having these parameters (11). However, while the lattice parameters produced by these wavevector sets are the same, the periods of the resulting optical lattices, scaled to the excitation wavelength  $\lambda$ , take on any one of a series discrete values defined by the parameters (11). The smallest period, three wavevector lattice for a given parameter set is termed the *fundamental* one (fig. S1B), while larger period three wavevector lattices are termed *sparse* (fig. S1C).

Since the symmetry of a lattice is defined by the set of operations that transform the lattice onto itself, application of any valid symmetry operation to the wavevector set of a given optical lattice produces a new wavevector set and a new optical lattice of the same parameters and periodicity, but with an electric field in each unit cell also transformed by the chosen symmetry operation (fig. S1D). Adding multiple wavevector sets generated in this manner produces a *composite* 2D optical lattice of the same parameters, but comprised of more than three wavevectors (fig. S1E). Because these wavevectors converge from a broader range of azimuthal angles, they produce an electric field of higher 2D spatial frequency content  $\mathbf{k}_m - \mathbf{k}_n$ . Adding together all wavevector sets obtained by applying all valid symmetry operations to a given lattice produces a *maximally symmetric composite lattice* that has the maximum possible spatial frequency content for that particular Bravais symmetry (11), (fig. S1F).

When all input plane waves have the same phase and have their polarizations  $\mathbf{e}_n$  maximally projected onto the same desired state  $\mathbf{e}$ , constructive interference between all these waves produces an intense, highly confined intensity maximum at one point in each unit cell, while partial destructive interference yields a background of low intensity elsewhere in each cell. The more wavevectors that comprise the lattice, the higher the contrast of this maximum to the background, and the closer the maximum approximates an ideal, circularly symmetric, diffraction-limited spot. Having the greatest 2D symmetry, hexagonal and square lattices produce maximally symmetric composite lattices with the greatest number of wavevectors from the broadest range of directions, and hence tend to be the ones best suited to serve as multifocal excitation arrays (11).

#### d. Bessel-Gauss beams and bound 2D optical lattices

Neither an ideal Bessel beam nor an ideal 2D optical lattice is directly useful for light sheet microscopy. The ideal Bessel beam contains equal energy in the central peak and each side lobe (59). Hence, sweeping this beam in  $x$  across the  $xy$  detection focal plane produces excessive fluorescence excitation outside this plane. In a similar vein, the ideal 2D optical lattice extends across all 3D space, and must be somehow confined in  $z$  to limit the excitation to the  $xy$  detection

focal plane. Furthermore, like any ideal non-diffracting beam, both these constructs require illumination confined to an infinitesimally thin ring at the rear pupil of an excitation objective, which is not physically possible.

The solution in either case is to illuminate the rear pupil over an annulus of finite width. The resulting beam will no longer be strictly non-diffracting, but will still have a cross-sectional profile in the  $xz$  plane that remains nearly constant over a field of view in  $y$  defined by the annulus width. For Bessel beam plane illumination microscopy (7, 8, 57), the annulus is illuminated uniformly, resulting in a Bessel-Gauss beam having a mix of the characteristics of each: a suppression of higher order Bessel side lobes due to a Gaussian envelope provided by the continuum of wavevectors in  $\mathbf{k}_\rho$  across the annulus, and a much longer beam waist than a traditional Gaussian beam due to the elimination of wavevectors corresponding to  $\mathbf{k}_\rho$  values inside the inner diameter of the annulus.

For lattice light sheet microscopy, we wish to preserve the broad field of view of an ideal 2D optical lattice in the  $x$  direction as well as its high spatial frequency content in this direction to obtain the best possible resolution for the SIM mode. However, at the same time, we wish to confine the lattice in  $z$  in order to make the light sheet as thin as possible. The resulting *bound lattice* (15) is obtained by spreading the energy in the  $z$  direction at each of the discrete points in the rear pupil that create the lattice, creating a series of narrow parallel stripes (movie S1). The energy in these stripes remains constrained by the dimensions of the annulus, in order to ensure that the resulting light sheet covers the desired  $y$  field of view. However, within this constraint, increasing the length of these stripes creates an increasingly broad continuum of wavevectors in  $\mathbf{k}_z$  that confine the lattice in  $z$  within an increasing narrow envelope (movie S1). In particular, when the width of this envelope is comparable to or narrower than the period of the lattice in  $z$ , only one row of lattice maxima in a single plane is dominantly excited, creating a narrow lattice light sheet (**Fig 1C**).

Note that the illumination stripes associated with lattice wavevectors closest to the  $x$  axis can be extended in  $z$  by the greatest amount before they are clipped by the edges of the annulus. Hence it is often advantageous to choose the orientation of the lattice around its propagation axis  $y$  such that one or more pairs of its wavevectors symmetrically straddle the  $z$  axis while falling close to the  $x$  axis within the rear pupil. This not only permits the tightest possible  $z$  confinement for that particular lattice, it also results in the highest possible spatial frequencies in  $x$  yielding the highest possible spatial resolution in that direction in the SIM mode.

On the other hand, besides shortening the  $y$  field of view, another disadvantage of a thick annulus and long illumination stripes is that at very high confinement, the lattice maxima become broadened in  $z$ , creating a thicker light sheet yielding poorer  $z$  resolution in the dithered mode (**Fig. 1C**). It is therefore doubly important to choose an annulus no wider than is absolutely necessary to confine the lattice in  $z$  by the desired amount. Fortunately, for many lattices in both the dithered and SIM modes, it is not necessary to completely confine the excitation to a single lattice plane – in the dithered mode, the contribution of flanking lattice planes to the overall PSF is suppressed by the  $z$  envelope of the detection PSF (**Fig. 1D**, fig. S2), whereas in the SIM mode, the additional lattice planes increase the strength of the highest

$\mathbf{k}_z$  spatial frequencies in the excitation (fig. S3), yielding SIM reconstructions of higher SNR at lower power.

### e. Linear arrays of coherent Bessel beams

Another way to create a thin light sheet that spreads the excitation across the entire field of view in the same manner as a bound 2D optical lattice is to use a linear array of closely spaced Bessel-Gauss beams. Indeed, it was the effectiveness of using an array of seven such beams in reducing phototoxicity in Bessel beam structured plane illumination microscopy (8) that sparked our interest in finding a way of further spreading the illumination across the plane. With seven beams, the beam separation was large enough that the coherent interaction between the side lobes of adjacent beams was negligible. However, for a dense array of Bessel-Gauss beams, it is essential to model these coherence effects.

We consider two different cases: where all beams have the same phase at the central peak, and where adjacent beams have opposite phase. In either case, as the period of the linear array decreases, the side lobes of adjacent beams interfere, creating an alternating series of increasingly strong resonant and anti-resonant patterns of constructive and destructive interference (movie S18, right). Recall from above that the side lobes of a Bessel beam alternate in phase (fig. S24B). Thus, at specific periods:

$$T_j^{+-} = (j - 0.5)\lambda / NA_{\min} \text{ (beams of alternating opposite phase)} \quad (9)$$

$$T_j^{++} = j\lambda / NA_{\min} \text{ (beams of identical phase)} \quad (10)$$

$j \geq 1$ ,  $NA_{\min}$  being the numerical aperture associated with the inner diameter of the annulus, side lobes of the same phase from adjacent beams overlap in the  $xy$  plane, producing strong modulation in this plane. At the same time, the side lobes that overlap just outside this plane have different phases, and interfere destructively. The result is a tightly confined structured excitation plane (fig. S25) similar to those achieved with bound 2D optical lattices.

An alternative explanation for this confinement emerges when we consider the illumination patterns at the rear pupil plane of the excitation objective that give rise to these coherent arrays (movie S18, left). As the period of the array decreases, the initially continuous annulus of illumination that produces a single Bessel beam breaks into an expanding periodic array of stripes aligned along the  $z$ -axis, yet still bound by the dimensions of the annulus. At the specific periods  $T_j^{+-}$  and  $T_j^{++}$  from above, the outermost stripe of this periodic array that still fits within the annulus is tangent to the annulus inner diameter. As was the case with 2D lattices, at this location the stripe contains the broadest possible range of  $\mathbf{k}_z$  wavevectors within the constraint of annular illumination, creating the narrowest possible envelope confining the excitation, and thus resulting in a narrow structured light sheet suitable for light sheet microscopy in either the dithered or SIM modes.

### f. Bessel beam arrays are bound 2D optical lattices

As can be seen from movie S18, a coherent linear array of Bessel-Gauss beams is a periodic optical pattern created by illuminating an annular region within the rear pupil of an objective lens with a finite set of stripes narrow in  $x$  but broad in  $z$ , with the center of each stripe corresponding to a discrete wavevector  $\mathbf{k}_n$  on a converging cone of wavevectors. These Bessel-Gauss arrays indeed then *are* bound optical lattices. The discrete periods  $T_j^{+-}$  and  $T_j^{++}$  that produce patterns of the tightest confinement in  $z$  correspond to the discrete periods of specific fundamental and sparse 2D optical lattices of various symmetries and lattice parameters that have been oriented to produce wavevector sets symmetric about the  $z$ -axis, with one or more pairs of wavevectors near the  $x$ -axis. These latter wavevectors correspond to illumination points in the rear pupil near the inner diameter of the annulus, where the illumination can be spread in  $z$  to the greatest possible extent, thereby producing lattice light sheets that are confined to the same degree as the corresponding Bessel-Gauss beam arrays.

This connection between linear Bessel-Gauss arrays and bound 2D optical lattices is highlighted in fig. S26, where the two arrays of shortest period for each of the alternating or identical phase cases are shown to be nearly identical to the light sheets produced by specific bound 2D lattices. The illumination patterns in the rear pupil that create these comparable patterns are also nearly identical.

While every coherent array of Bessel-Gauss beams is equivalent to a 2D bound optical lattice, the converse is not true: Bessel-Gauss arrays are characterized by wavevector sets equally spaced in  $\mathbf{k}_x$  (*i.e.*, a set of parallel, equally spaced stripes in the rear pupil), whereas not all optical lattices satisfy this condition (*e.g.*, columns 3-5 of fig. S1F, fig. S2F). Thus, the optical lattice formalism provides solutions for lattice light sheets of unique abilities not found by the beam array formalism, such as the fundamental hexagonal lattice (fig. S3A) which permits high speed, three phase SIM imaging with near-optimal resolution extension in  $x$  and  $z$  (movie S5).

To summarize, thin light sheets suitable for lattice light sheet microscopy can be derived from any of three different physical pictures:

- a linear array of Bessel-Gauss beams, where the separation between the beams is such that side lobes of the same phase from adjacent beams overlap in the  $xy$  illumination plane;
- a linear array of Bessel-Gauss beams, resulting from stripes of illumination mutually parallel to an axis  $z$ , where such stripes are confined to an annulus in the rear pupil of an objective lens that creates the array, and where the separation between the beams is such that the pair of stripes furthest from and on opposite sides of the  $z$ -axis reside near the inner diameter of the annulus.
- a bound 2D optical lattice, where the circle of discrete illumination points in the rear pupil of an objective lens that creates the ideal 2D lattice falls within an annulus, and where the illumination at these points is spread across lines parallel to an axis  $z$ , but still bound by the

inner and outer diameters of the annulus. It is often advantageous to rotate the lattice about its propagation direction  $y$  such that two of its illumination points are positioned on or near the  $x$  axis and symmetrically about the  $z$ -axis, where they can be spread in  $z$  by the greatest possible amount within the confines of the annulus.

Lattice light sheets consisting of parallel stripes of illumination that provide confinement of excitation to a single  $xy$  plane might be designed by other paradigms, but are not considered in depth here. These include using linear arrays of other non-diffracting beams, such as the first order Bessel beam  $J_1(k\rho \sin \theta)$  (where the phase varies linearly with azimuthal angle  $\varphi$  around the annulus), or 3D optical lattices having additional wavevectors not confined to a single ring in the rear pupil. These would produce modulation along the propagation axis  $y$  as well as the usual modulation axis  $x$ , but a temporally uniform average intensity in  $y$  could be attained by dithering the pattern in  $y$ , either with an objective-mounted piezo, or with a relay lens of electrically adjustable focal length.

## 2. Calculating the SLM Pattern That Generates the Desired Lattice Light Sheet

We create a lattice light sheet by using a binary SLM that is conjugate to the front focal plane of the excitation objective (fig. S4A). The light diffracted by the SLM is filtered by an annular mask that is conjugate to the rear pupil plane. The mask filters out unwanted diffraction orders and ensures that the resulting light sheet covers the desired  $y$  field of view. We need to find binary SLM patterns for lattice light sheets of specific desired properties (e.g., field of view in  $y$ , excitation confinement in  $z$ , breadth of spatial frequencies in  $k_x, k_z$  (SIM mode), and overall resolution in  $z$  (dithered mode)), and confirm theoretically that light beams diffracted by these patterns and filtered by the annulus do indeed produce the desired light sheets within the specimen.

We start with an ideal 2D optical lattice of electric field  $\mathbf{E}_{ideal}(x, z)$ , initially using our intuition to select a lattice of symmetry, periodicity, and orientation about  $y$  as discussed above that we expect will produce a light sheet that can be optimized for our ends. We then calculate the real amplitude  $E_{real}(x, z)$  of the component of  $\mathbf{E}_{ideal}(x, z)$  that projects on the desired polarization state  $\hat{\mathbf{e}}_d$  (fig. S5A):

$$E_{real}(x, z) = \text{Re} \{ \mathbf{E}_{ideal}(x, z) \cdot \hat{\mathbf{e}}_d \} \quad (11)$$

Since the SLM pattern is imaged at the sample to create the confined light sheet,  $E_{real}(x, z)$  must be bound in  $z$  (fig. S5B):

$$E_{bound}(x, z) = \psi(z) \cdot E_{real}(x, z) \quad (12)$$

where the binding function  $\psi(z) \rightarrow 0$  as  $|z| \rightarrow \infty$ . Gaussian bounding,  $\psi(z) = \exp(-2z^2/a^2)$ , is a common choice. Choosing a more steeply bound function increases the confinement of the light sheet to a single plane (movie S1), thereby minimizing out-of-focus background, bleaching,

and phototoxicity. However, it also decreases the  $y$  field of view and reduces the effective  $z$  resolution by underweighting the highest  $k_z$  spatial frequencies in the pattern. Thus, part of the art of lattice light sheet microscopy involves judicious choice of the bounding function to balance these tradeoffs.

We use a binary phase ferroelectric SLM for its large number of pixels (necessary to cover a large field of view when projected at a Nyquist sampling interval consistent with diffraction-limited resolution) and fast switching time (necessary for rapid, sequential, plane-by-plane multicolor imaging). Thus, we need to convert  $E_{\text{bound}}(x, z)$  to a binary phase pattern (fig. S5C):

$$\varphi_{\text{SLM}}(x, z) = \pi \cdot H[|E_{\text{bound}}(x, z)| - \varepsilon] \quad (13)$$

where  $H(\xi)$  is the Heaviside step function ( $H(\xi) = 0$  for  $\xi < 0$ ,  $H(\xi) = 1$  for  $\xi > 0$ ) and  $\varepsilon < \max(|E_{\text{bound}}(x, z)|)$  is a threshold level that determines which pixels are set high ( $\varphi = \pi$ ) or low ( $\varphi = 0$ ). Increasing  $\varepsilon$  increases the confinement of the light sheet, with the tradeoffs discussed above. In practice, we typically set  $\varepsilon = 0.1 \cdot \max(|E_{\text{bound}}(x, z)|)$ .

While Eq. 12 gives us a candidate for the pattern we should apply to the SLM, we still need to verify that this pattern theoretically produces a lattice light sheet of the desired properties. We do this by calculating the resulting light pattern at successive stages from the SLM to the specimen. First, passage through a lens (fig. S4A) of the light that is phase modulated by the SLM produces a diffraction pattern (fig. S5D) at the plane of the annular mask given by:

$$I_{\text{diff}}(k_x, k_z) = |FT[\exp(i\varphi_{\text{SLM}}(x, z))]|^2 \quad (14)$$

where  $FT[F(x, z)] = (1/2\pi) \cdot \int_{-\infty}^{\infty} \int_{-\infty}^{\infty} F(x, z) \exp(ik_x x + ik_z z) dx dz$  is the 2D Fourier transform. After passage through the transmissive annulus of center radius  $a$  and thickness  $\tau$  (fig. S5E):

$$A(k_x, k_z) = H\left(\tau / 2 - \left|\sqrt{k_x^2 + k_z^2} - a\right|\right) \quad (15)$$

the intensity pattern that is then projected to the rear pupil of the excitation objective is given by (fig. S5F):

$$I_{\text{pupil}}(k_x, k_z) = A(k_x, k_z) \cdot I_{\text{diff}}(k_x, k_z) \quad (16)$$

while the electric field at the rear pupil is:

$$E_{\text{pupil}}(k_x, k_z) = A(k_x, k_z) \cdot FT[\exp(i\varphi_{\text{SLM}}(x, z))] \quad (17)$$

Finally, this field produces a lattice light sheet of cross-sectional intensity profile (fig. S5G):

$$PSF_{\text{exc}}(x, z) = \left|FT\{A(k_x, k_z) \cdot FT[\exp(i\varphi_{\text{SLM}}(x, z))]\}\right|^2 \quad (18)$$

after passage through the excitation objective. In most cases, the theoretical  $PSF_{exc}(x, z)$  closely resembles the experimentally measured one (Fig. S6).

We next need to evaluate the performance of the microscope when using this light sheet in either the SIM or dithered mode. The expanded optical transfer function (OTF) that defines the  $xz$  resolution after SIM reconstruction is given by:

$$OTF_{SIM}(k_x, k_z) = FT[PSF_{exc}(x, z) \cdot PSF_{detect}(x, z)] \quad (19)$$

where  $PSF_{detect}(x, z)$  is the point spread function of the detection objective as determined by a vector model of diffraction at the focus of a high NA lens (60). Alternatively, the cross-section of the dithered lattice light sheet is found by integrating  $PSF_{exc}(x, z)$  over one period  $T_x$  of the lattice in the dither direction (fig. S5H):

$$PSF_{dither}(z) = \int_0^{T_x} PSF_{exc}(x, z) dx \quad (20)$$

and the overall PSF that defines the  $xz$  resolution in the dithered mode is given by:

$$PSF_{overall}(x, z) = PSF_{dither}(z) \cdot PSF_{detect}(x, z) \quad (21)$$

The usable  $y$  field of view for the light sheet can be estimated by calculating the intensity  $I_{Bessel}(y)$  along the  $y$  axis of a Bessel beam created with an annulus of the same maximum and minimum NA as the lattice light sheet:

$$I_{Bessel}(y) = |\mathbf{E}_{focus}^{NA_{max}}(0, y, 0) - \mathbf{E}_{focus}^{NA_{min}}(0, y, 0)|^2 \quad (22)$$

where  $\mathbf{E}_{focus}^{NA}(\mathbf{x})$  is the 3D vector electric field near the focus under uniform illumination of the rear pupil (60).

In practice, we first choose according to Eq. 22 an annulus of maximum and minimum NA that produces a light sheet that spans the thickness of the specimen in the  $y$  direction. Choosing a light sheet that is longer than necessary risks creating an unnecessarily thick light sheet, and/or one with excessive sideband excitation beyond the central lattice plane. We then choose a particular lattice and bounding function  $\psi(z)$ , and use Eqs. 11-22 to calculate the cross-sectional profile  $PSF_{exc}(x, z)$ , SIM transfer function  $OTF_{SIM}(k_x, k_z)$ , and dithered mode overall point spread function  $PSF_{overall}(x, z)$  of the resulting lattice light sheet. Common choices for the lattice in the dithered mode are the maximally symmetric fundamental lattices of rectangular, square, and hexagonal symmetry of figs. S2A-C, respectively. Common choices in the SIM mode are the three beam fundamental hexagonal lattice (fig. S3A) and the maximally symmetric fundamental hexagonal and first sparse square lattices of figs. S3C & S3D. Next, we iterate through the calculation, keeping the initial seed lattice and annulus dimensions constant, while varying  $\psi(z)$  and observing the tradeoff between excitation confinement and  $z$  resolution in the SIM and dithered modes. If an acceptable compromise cannot be found, the process is repeated with a different annulus – for example, one of reduced maximum and minimum NA that

produces a somewhat thicker light sheet of the same  $y$  extent but with more strongly suppressed sidebands.

### 3. Detailed Optical Path

The schematic of the optical system is shown in Figure S4A. The beam from a laser combiner equipped with 405 nm (250mW, RPMC, Oxxius LBX-405-300-CIR-PP), 445 nm (100mW, RPMC, Oxxius LBX-445-100-CIR-PP), 488 nm (300 mW, MPB Communications, 2RU-VFL-P-300-488-B1R), 532 nm (500 mW, MPB Communications, 2RU-VFL-P-500-532-B1R), 560 nm (500 mW, MPB Communications, 2RU-VFL-P-500-560-B1R), 589 nm (500 mW, MPB Communications, 2RU-VFL-P-500-589-B1R) and 642 nm (500 mW, MPB Communications, 2RU-VFL-P-500-642-B1R) lasers is expanded to a  $1/e^2$  diameter of 2.5 mm by two lenses (8 mm FL/12.24 mm dia, Thorlabs C240TME-A, 20 mm FL/12.5 mm dia Edmund 47-661) before passing through a half wave plate (Bolder Vision Optik, BVO AHWP3) and an acousto-optic tunable filter (AA Quanta Tech, Optoelectronic AOTF AOTFnC-400.650-TN). The AOTF is used to select the wavelengths, control intensities and synchronize to the spatial light modulator (SLM) which generates the lattice patterns. Following the AOTF, two pairs of cylindrical lens (25 mm FL/12.5 mm dia, Edmund NT68-160 and 200 mm FL/25.4 mm dia, Thorlabs, ACY254-200-A to expand the beam in  $x$ , and 250 mm FL/25.4 mm dia, ThorLabs, ACY254-250-A and 50 mm FL/25.4 mm dia, Thorlabs, ACY254-050-A to contract the beam in  $z$ ) are positioned to expand the beam elliptically with  $1/e^2$  minor and major semi-axis of 0.5 and 20 mm, respectively. This expanded beam uniformly illuminates a thin strip of the SLM on which the lattice light sheet pattern is displayed. If wider SLM patterns are used, or if a more uniform illumination intensity is desired, the second set of cylindrical lenses contracting the beam in  $z$  may be omitted. The SLM itself is composed of 1280 x1024 ferroelectric-liquid-crystal pixels (Forth Dimension, SXGA-3DM), which together with a polarizing beam splitter cube (Newport, 10FC16PB.3) and a half-wave-plate (Bolder Vision Optik, BVO AHWP3) provide a 0 or  $\pi$  phase shift in the diffracted beam depending on the pixel state (61). The diffracted light from the SLM is then focused though a 500 mm focal length lens (500 mm FL/40 mm dia, Edmund 49-283) onto an annular mask (Photo Sciences Inc). The annular mask physically filters out the zeroth and higher order, unwanted, diffracted light caused by the finite-sized pixels of the SLM. After passing through the mask, the desired diffraction orders are demagnified .75X through relay lenses (80 mm FL/12.5 mm dia, Edmund NT47-670, 60 mm FL/12.5 mm dia, Edmund NT47-668) and conjugated to a scanning system composed of 2 3 mm galvos (Cambridge Technology, 6215H) and one pair of matched focal length achromatic relay lenses (25 mm FL/12.5 mm dia, Edmund NT47-662) in a 4f arrangement. As each galvo is aligned conjugate to the back pupil of the excitation objective, this system provides scanning along the  $x$  and  $z$  axis at the sample. After passing through the scanning system, the image of the annular mask is re-magnified 3.2X through relay lenses (125 mm FL/25 mm dia, Edmund NT49-361, 400 mm FL/25 mm dia, Edmund 47-650) and conjugated to the back focal plane of a custom manufactured excitation objective (Special Optics, 0.65 NA, 3.74 mm WD). Thus, the SLM and excitation focus, and the annular mask, scanning galvos, and the back pupil form two sets of conjugate planes in the illumination path. After the lattice light sheet is projected onto the focal plane of the excitation objective, the excited fluorescence of the sample is collected by an orthogonally mounted detection objective (Nikon, CFI Apo LWD 25XW, 1.1 NA, 2 mm WD)

whose focal plane is coincident with lattice light sheet illumination. The fluorescence signal is then imaged through an emission filter onto an sCMOS camera (Hamamatsu, Orca Flash 4.0 v2 sCMOS) by a 500 mm tube lens (500 mm FL/25 mm dia, Edmund 47-651) to provide an overall magnification of 62.5X. Two inspection cameras (AVT Guppy F-146 CCD camera, FireWire.A, Edmund 59-731), located in planes conjugate to either the back pupil of the excitation objective or to the sample, aid in alignment and verification of the lattice light sheet pattern.

## 4. SLM Operation

### *a. SLM basics*

The SLM displays binary images on the device in a user programmable “Running Order”. The timing of each image displayed in a Running Order is governed by its Sequence. The Sequences used in our software consist of a Reload time (401  $\mu$ s), Positive image, Invert time (60  $\mu$ s) and Negative image. Both the Positive and Negative images on the SLM display result in the same illumination intensity at the sample, but cause a 0 or  $\pi$  phase inversion of the electric field. The duration of the Positive image and Negative image times are user programmable, but the physics of the ferroelectric SLM device require each pixel to spend an approximately equal duration in each state. During Reload and Invert times, the SLM is changing state and should not be used for imaging. A single digital output hardware line (LED Enable) is set high when the SLM is in the Positive or Negative image state (Figure S15). An SLM sequence cannot be interrupted once it has begun. This makes external clocking of each SLM image a poor choice for high speed applications. Therefore, the SLM is run with internal timing and is chosen as the master time source for the lattice light sheet microscope.

### *b. SLM synchronization*

Within a single image acquisition, the SLM pattern, the AOTF frequency, power and blanking, the camera exposure, and the x- and z-galvo, sample piezo and objective piezo waveforms must all be synchronized. To accomplish this, the control software reads the LED Enable line from the SLM. However, since the SLM does not provide a way to query which part of the Running Order (i.e. which image is currently being displayed), the current SLM state must be obtained by counting the number of LED Enable pulses from a known starting point. To set the SLM to the beginning of a Running Order, the following is performed prior to the start of a scan: 1) the SLM is placed into a deactivated state, 2) the Running Order is loaded, 3) the first step of the Running Order is programmed to await a hardware Start trigger signal, 4) the hardware trigger Start signal is sent from the FPGA to the SLM to initiate the Running Order. By recording the number of LED Enable line transitions, the state of the SLM is known and deterministic (Figure S16).

### *c. Camera synchronization*

The camera operates in external trigger mode in the rolling shutter readout mode. When the camera receives an external trigger, it begins a readout of the sensor. The readout time is determined by the number of sensor rows in the region of interest and the readout rate (~4.8  $\mu$ s/row). During the camera readout, the Timing output 1 (Camera Fire) digital line goes low. Otherwise the Camera Fire line is set high. For volumetric scanning, we require all emission photons within a specific time window to be recorded by a single camera readout (i.e. when the sample/objective-piezo are at specific planes, or when a specific pattern is displayed on the SLM), thus the readout time of the camera is generally not usable and we perform all illumination only when Camera Fire is high. In order to maximize imaging efficiency, it is advantageous to overlap the readout time of the camera with the reload time of the SLM (Figure S17).

### *d. SLM synchronized acquisition*

The FPGA is preloaded with the timing information for the Running Order, and the readout time of the camera. The FPGA triggers the camera, so that the camera readout ends when the SLM LED Enable is triggered. This maximizes imaging efficiency. A rising Camera Fire line begins the playback of the output scan waveforms. These waveforms control the x-galvo, z-galvo, objective-piezo, sample-piezo, AOTF frequency, and AOTF power. The AOTF blanking channel is independently synchronized with the LED Enable signal of the SLM. This ensures that the laser is off during the Invert time of the SLM, which is typically small compared to a camera exposure (Figure S18).

## 5. Sample Preparation

### *a. Mammalian cell culture and imaging*

All mammalian cells were cultured on pre-cleaned 5 mm diameter cover slips coated with 10 micrograms/ml of fibronectin (Millipore, FC010) to aid adhesion. For comparison of the various imaging modes (Bessel vs. lattice light sheet, dithered mode vs. SIM, **Fig. 2**, movies 1, S3-S5,) HeLa cells were transiently transfected with mEmerald-Lifeact using an Amaxa 96 well shuttle system (Lonza) with 1 ug DNA per 400,000 cells with nucleofection solution and program optimized for the individual cell line per the manufactures instructions. Imaging was performed at 37°C in L15 medium without phenol red (Life Technologies) with 10% fetal bovine serum (Life Technologies).

For PALM imaging (**Fig. 3F-H**, movie S10), U2OS cells were transiently transfected with Dendra2-lamin A/C using an Amaxa 96 well shuttle system (Lonza) with 1ug DNA per 400,000 cells, cultured for 12 hours prior to fixing in a solution of 4% paraformaldehyde (Electron Microscopy Sciences), and 0.1% gluteraldehyde (Electron Microscopy Sciences) in PHEM buffer containing 60mM PIPES, 25mM HEPES, 10mM EGTA and 2mM MgCl<sub>2</sub> (all from

Sigma) for 1 hr. Samples were then rinsed 3 times in phosphate buffered saline prior to imaging in phosphate buffered saline at room temperature for the duration of the experiment.

For three color imaging of organelles during mitosis (**Fig. 4B**, movie 6), LLCPK1 cells stably expressing mEmerald-Calnexin and mApple-H2B were labeled with MitoTracker Deep Red dye (Life Technologies) as per the manufacturer's instructions and imaged at 37 °C in L15 medium (Life Technologies) without phenol red with 10% fetal bovine serum.

For tracking microtubule dynamics (**Fig. 4A**, figs. S8, S9, movies 5, S11-S12), HeLa cell clones (A1) stably expressing GFP-EB1 and Tag-RFP-H2B (evrogen) were plated on coverslips for approximately 12 hours prior to imaging at 37°C in L15 medium without phenol red with 10% fetal bovine serum. The HeLa cell clones were established as described in (62).

*b. Mouse embryonic stem cell culture and imaging*

Mouse D3 (ATCC) ES cells stably expressing halo-Sox2 were cultured on 0.1% gelatin coated plates in the absence of feeder cells. See (22) for details of stable cell line construction. The ES cell medium was prepared by supplementing knockout DMEM (Life Technologies) with 15% FBS, 1mM glutamax, 0.1mM nonessential amino acids, 1mM sodium pyruvate, 0.1mM 2-mercaptoethanol and 1000 units of LIF (Millipore). One day before imaging, cells were plated onto a clean cover glass pre-coated with Matrigel (BD). Imaging experiments were performed in the ES cell imaging medium, which was prepared by supplementing FluoroBrite medium (Invitrogen) with 10% FBS, 1mM glutamax, 0.1mM nonessential amino acids, 1mM sodium pyruvate, 10mM Hepes (pH 7.2~7.5), 0.1mM 2-mercaptoethanol and 1000 units of LIF (Millipore) at 37 °C. Before imaging, we treated samples with 1nM haloTag-TMR ligand (Promega: G8251) for 10mins. Under this sparse labeling condition, Sox2 single-molecules were immediately visible under the microscope without extensive pre-bleaching (**Fig. 3A-E**, movies S8, S9).

*c. Generation of Mouse Cytotoxic T Cells and Cell Culture.*

OT-I splenocytes were stimulated with 10 nM OVA257-264 peptide for 3 days in RPMI medium 1640 supplemented with 10% FCS, 50 mM  $\beta$ -mercaptoethanol, 10 U/mL human recombinant IL-2, L-glutamine, sodium pyruvate, and 50 U/mL penicillin and streptomycin (Gibco). After 3 days, cells were washed and seeded into fresh media with IL2 daily. EL4 target cells stably expressing a plasma membrane marker fused to tagRFP were maintained in Dulbecco's Modified Eagle's Medium (DMEM) supplemented with 10% FCS, L-glutamine, and 50U/mL penicillin and streptomycin (Gibco).

OT-I T cells were transfected with plasmid DNA coding for mEmerald-Lifeact 5-7 days after primary stimulation using the AMAXA mouse T cell nucleofector kit (Lonza) according to the manufacturer's protocol. Cells were used for experiments 18-24 hours after nucleofection.

Prior to imaging, EL4 target cells were pulsed with 1  $\mu$ M OVA peptide for 1 hour at 37 °C, washed twice in DMEM (GIBCO) and plated onto 5mm coverslips coated with 1 $\mu$ g/ml murine ICAM-1/FC (R&D Systems) overnight at 4°C. Target cells were allowed to settle for 5 minutes before the media was replaced with an imaging buffer of RPMI lacking phenol red (Gibco) supplemented with 10% FCS, and 50 U/mL penicillin/streptomycin at 37 °C. Approximately 2 million OT-I were centrifuged at 1600RPM for 3 minutes and resuspended in 50  $\mu$ l of imaging medium. T cells were added drop-wise over target cells and were allowed to settle and adhere for 3 minutes. Imaging was performed within 10 minutes of T cell introduction. T cells migrating toward target cells were identified, and the cell pair was imaged during the formation of the immunological synapse (**Fig. 5A-C**, movie 8).

*d. Neutrophil migration studies*

mCherry-utrophin HL-60 cells were derived by lentiviral transduction of ATCC cell line #CCL-240, and were grown in medium RPMI 1640 supplemented with 15% FBS, 25mM Hepes, and 2.0g/L NaHCO<sub>3</sub>, and at 37C with 5% CO<sub>2</sub>. Lentivirus was produced in HEK293T grown in 6-well plates and transfected with equal amounts of the lentiviral backbone vector (a protein expression vector derived from pHRSIN-CSGW (63), by cloning the actin-binding domain of utrophin (64) followed by a flexible linker (amino acid sequence: GDLELSRILTR) to the N-terminus of mCherry), pCMV $\Delta$ 8.91 (encoding essential packaging genes) and pMD2.G (encoding VSV-G gene to pseudotype virus). After 48hr, the supernatant from each well was removed, centrifuged at 14,000g for 5 minutes to remove debris and then incubated with ~1 x 10<sup>6</sup> HL-60 cells suspended in 1mL complete RPMI for 5-12 hours. Fresh medium was then added and the cells were recovered for 3 days to allow for target protein expression, and expressing cells were selected fluorescence-activated cell sorting (FACS). Prior to imaging, HL-60 cells were differentiated by treatment with 1.3% DMSO for 5 days. For 2D migration, differentiated HL-60 cells were allowed to adhere to fibronectin-coated coverslips for 30 minutes before coverslip was moved to the imaging chamber (movie 10). For 3D migration, cells were over-layed onto coverslips containing pre-formed 1.7% collagen matrix polymerized as

described (65) using 50% FITC-collagen (Sigma) and allowed to migrate into the network for one hour before removing the coverslip to the imaging chamber (**Fig. 5D-F**, movie 9). Cells were imaged in 1X HBSS supplemented with 3% FBS, 1X pen/strep, and 40 nM of the tripeptide formyl-MLP (to stimulate migration).

*e. Dictyostelium discoideum and Tetrahymena thermophila cell culture and imaging*

Vegetative *D. discoideum* cells expressing GFP-tubulin (66) (movie 2) were grown in HL5 media (MP Biomedicals) and imaged in DB buffer at 22 °C. *D. discoideum* cells expressing GFP-dajumin (67) (movie S7) were imaged in 20 mM PBS (pH 6.6) buffer at 22°C. *D. discoideum* cells expressing GFP-LimE (67) (movie 3) were imaged in DB buffer at 22 °C.

*D. discoideum* cells expressing RFP-LimE were grown in HL5 media. Cells were starved for 5 hrs in DB buffer and plated onto a 5 mm dia cover slip prior to imaging. Their migration and aggregation in response to natural oscillations of cAMP were then imaged (fig. S11, movie S14) in DB buffer at 22 °C.

To prepare the *T. thermophila* specimen, the scramblase coding sequence (TTERM\_00264820) was amplified by PCR from genomic DNA and cloned into the ‘donor’ plasmid pENTR D-TOPO, which was subsequently cloned by the Gateway (Clonase) method into the ‘destination’ vector pIGF-gtw (55). This vector includes the *T.t.* rDNA with a point change in the 17S rRNA for paromomycin resistance (positive selection of *T.t.* transformants), the MTT1 promoter (inducible by Cd++), and the GFP cds upstream of the Clonase-mediated recombination site. Conjugating *T.t.* cells (CU427 X CU428) were transformed with the vector (pIGF :: *T.t.*Scr1) by electroporation 9 hours after the initiation of conjugation, and transformed exconjugants selected with 100 µg/ml paromomycin. Expression of the GFP-Scr1 fusion protein in transformants was induced by the addition of 1.5 µg/ml CdCl2. Expressing cells were embedded in 0.5% low melting point agarose (Fisher). A single specimen trapped in a small pocket (**Fig. 4C**, fig. S10, movies 7, S13) was imaged in Dryl’s buffer at 22 °C.

*f. Caenorhabditis elegans culture and imaging*

*C. elegans* embryos imaged in the three-fold stage (movies S6, S15) were strain OD95 (Strain information: OD95 unc-119(ed3)III;ItIs37[pAA64;pie-1/mCherry::his-58;unc-119(+)]IV;ItIs38[pAA1;pie-1/GFP::PH(PLC1delta1); unc-119(+)], (68) expressing GFP-PH (a plasma membrane marker) and mCherry-H2B. Samples were imaged in M9 buffer at 24°C.

*C. elegans* embryos expressing GFP-AIR2, mCherry-H2B, and mCherry-PH, a (**Fig. 6A**, fig. S12, movie 11) were imaged in M9 buffer at 20°C.

*C. elegans* embryos expressing eGFP-Lifeact (**Fig. 6B**, fig. S13, movie 12) were rapidly affixed to coverslips with BD Cell-Tak adhesive (BD Biosciences) after dissection and imaged in M9 buffer at 22°C.

*g. Drosophila melanogaster culture and imaging*

*D. melanogaster* embryos were dechorionated using 50 % bleach and desiccated ~3 minutes for alignment and imaging. They were immersed in Schneider's S2 medium (Sigma) supplemented with a 100 fold dilution of 100x antibiotic/antimycotic (Life Technologies) at room temperature for the duration of imaging. The fly lines used in these experiments include the following. A ubiquitously expressed DE-cadherin-eGFP (69) and Gal4-UAS driven RFP-Moe-ABD (actin binding domain of Moesin) expressed in the epidermis using the e22c-Gal4 driver (Bloomington #1973) (70), (**Fig. 6C**, movie S16). Although both cadherin and moesin were acquired in a 2 color dataset, only cadherin is shown. An endogenously GFP-labeled zipper, nonmuscle myosin-II recovered from an exon trap screen (Flytrap #CC01626) (71), (**Fig. 6D**, movie 13). GFP-Moe-ABD expressed under the control of the sqh promoter enhancer cassette (a.k.a. sGMCA) to visualize actin (72) and mCherry-nonmuscle myosin light chain also expressed under the control of the sqh promoter enhancer cassette (73) (**Fig. 6E, F**, movie S17). Although both sGMCA and myosin light chain were acquired in a 2 color dataset, only sGMCA is shown.

## SUPPLEMENTARY FIGURES

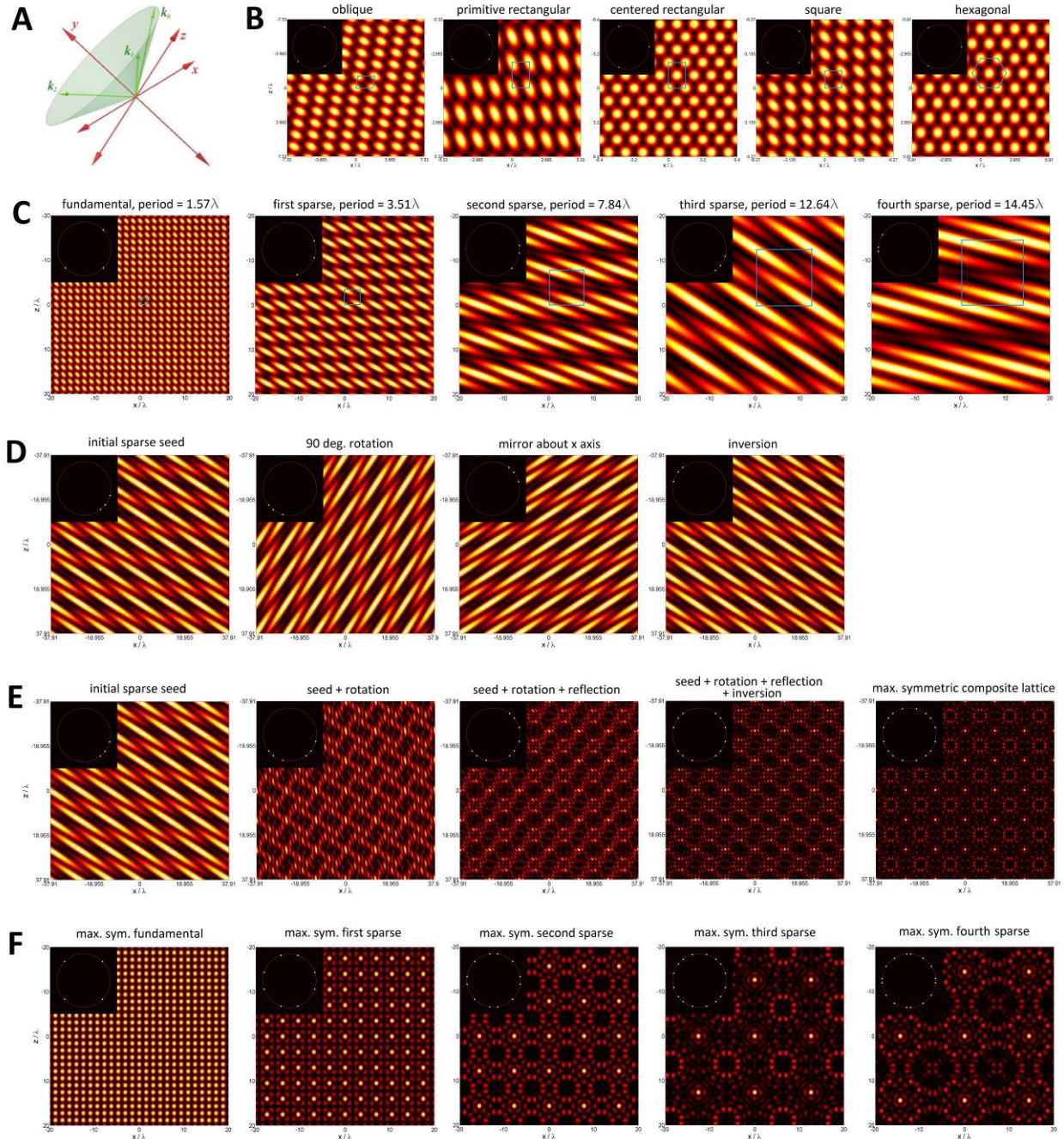


**Fig. S1. Principles and definitions for two-dimensional optical lattices.** (A) All wavevectors  $\mathbf{k}_n$  of any 2D optical lattice lie on the surface of a single cone. (B) Fundamental 2D optical lattices for each of the five possible Bravais lattice symmetries. Insets show the locations (white) of the light beams in the rear pupil (red) that are needed produce the wavevectors that generate the corresponding lattice. (C) The five shortest period 2D sparse optical lattices of square symmetry. Scaling assumes 0.6 NA excitation. (D) Generation of new sparse 2D optical lattices by applying one of the symmetry transformations valid for that lattice type to an existing sparse lattice. (E) Composite lattices formed by stepwise addition of the wavevector sets from the different sparse lattices of the same

symmetry and period from (D). The rightmost example shows the maximally symmetric composite lattice created by applying all symmetry operations of a square Bravais lattice to the sparse lattice at left. (F) The five shortest period 2D maximally symmetric composite lattices of square symmetry, derived from the sparse lattices in (C).

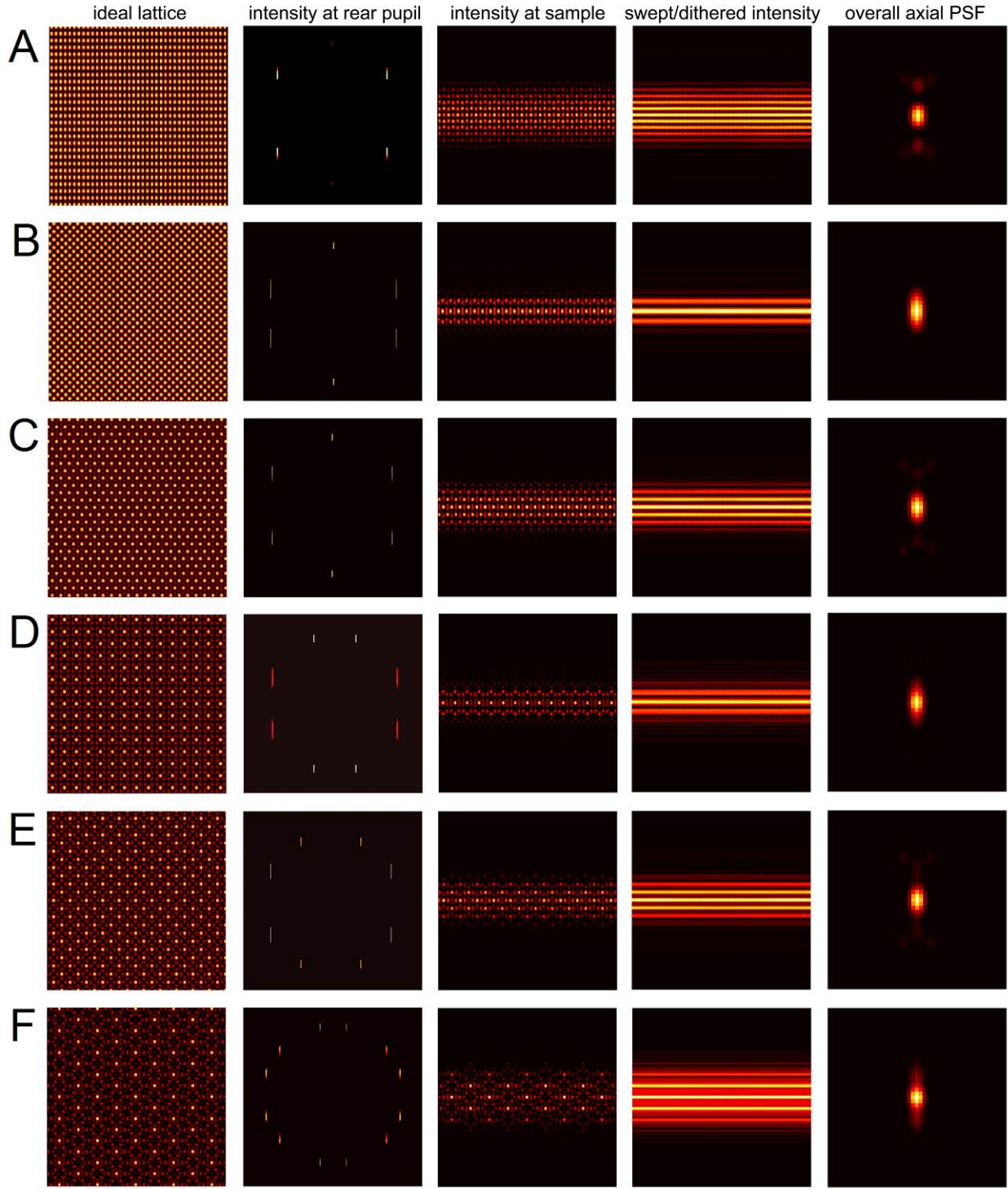


**Fig. S2. Lattices optimized for the dithered mode.** Calculated examples of lattices where the axial bounding has been optimized to produce high resolution in the  $z$  direction when used in the dithered lattice mode. Columns from left to right: the ideal 2D lattice in the  $xz$  plane upon which light sheet is based; the intensity pattern at the rear pupil of the excitation objective that produces the light sheet; the  $xz$  cross-sectional intensity profile of the stationary lattice light sheet at the sample; the  $xz$  cross-sectional intensity after the light sheet is dithered; and the overall point spread function (PSF) defined by the product of the dithered intensity profile and the PSF of the detection. (A)

Maximally symmetric fundamental rectangular lattice, with  $z$  period =  $1.5 \times x$  period, where  $x$  period =  $2.641 \times NA_{exc} \times \lambda_{exc} / n$ , and  $NA_{exc}$  and  $\lambda_{exc}$  are the numerical aperture and free space wavelength, respectively, of the light used to create the ideal lattice, and  $n$  is the refractive index of the imaging medium. The ideal lattice is comprised of four wavevectors. **(B)** Maximally symmetric fundamental square lattice, rotated to place two of the four wavevectors of the ideal lattice along the  $x$  axis. These two wavevectors become two vertical bands in the bound lattice, which are then clipped by the annulus to create four smaller vertical bands in the rear pupil.  $x$  period =  $4.828 \times NA_{exc} \times \lambda_{exc} / n$ . **(C)** Maximally symmetric fundamental hexagonal lattice, rotated to place two of the six wavevectors of the ideal lattice along the  $z$  axis. The ideal lattice is comprised of six wavevectors.  $x$  period =  $4.896 \times NA_{exc} \times \lambda_{exc} / n$ . **(D)** Maximally symmetric first order sparse square lattice.  $x$  period =  $6.952 \times NA_{exc} \times \lambda_{exc} / n$ . **(E)** Maximally symmetric first order sparse square lattice, rotated  $45^\circ$  with respect to (D). The ideal lattice is comprised of eight wavevectors.  $x$  period =  $9.485 \times NA_{exc} \times \lambda_{exc} / n$ . **(F)** Maximally symmetric first order sparse hexagonal lattice,  $x$  period =  $20.92 \times NA_{exc} \times \lambda_{exc} / n$ . The ideal lattice is comprised of twelve wavevectors.

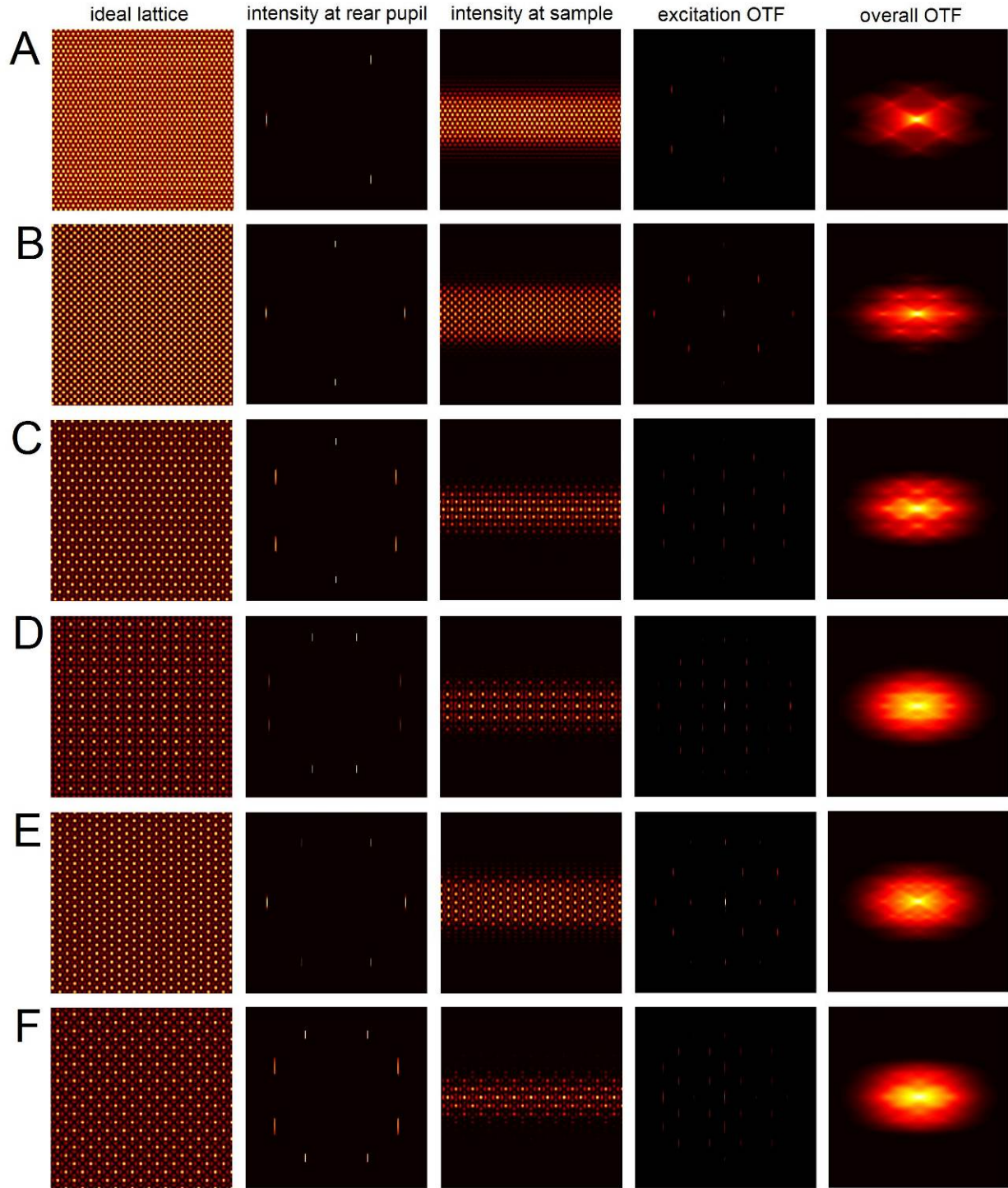


**Fig. S3. Lattices optimized for the SIM mode.** Calculated examples of lattices where the axial modulation depth and spatial frequency have been optimized to produce high resolution in the  $z$  direction when used in the structured illumination mode. Columns from left to right: the ideal 2D lattice in the  $xz$  plane; the intensity pattern at the rear pupil of the excitation objective that produces the lattice light sheet; the  $xz$  cross-sectional intensity profile of the light sheet at the sample; the optical transfer function (OTF) of the light sheet excitation in the  $xz$  plane; and the

overall  $xz$  OTF defined by the convolution of the excitation and detection OTFs. **(A)** Fundamental hexagonal lattice, comprised of three wavevectors, rotated to place one of the wavevectors on the x axis. The pattern requires three phase-stepped images for SIM reconstruction. **(B)** Maximally symmetric fundamental square lattice of the same type as in fig. S2B, but with less axial confinement for optimization in the SIM mode. Five phase-stepped images are required for SIM reconstruction. **(C)** Maximally symmetric fundamental hexagonal lattice of the same type as in fig. S2C, but also with reduced axial confinement. Five phase-stepped images are required for SIM reconstruction. **(D)** Maximally symmetric first order sparse square lattice of the same type as in fig. S2D, except with reduced axial confinement. Seven phase-stepped images are required for SIM reconstruction. **(E)** Maximally symmetric fundamental hexagonal lattice, rotated  $90^\circ$  with respect to the lattice in (C). Nine phase-stepped images are required for SIM reconstruction. **(F)** Maximally symmetric first order sparse square lattice, of the same type and orientation as in fig. S2E. Nine phase-stepped images are required for SIM reconstruction.

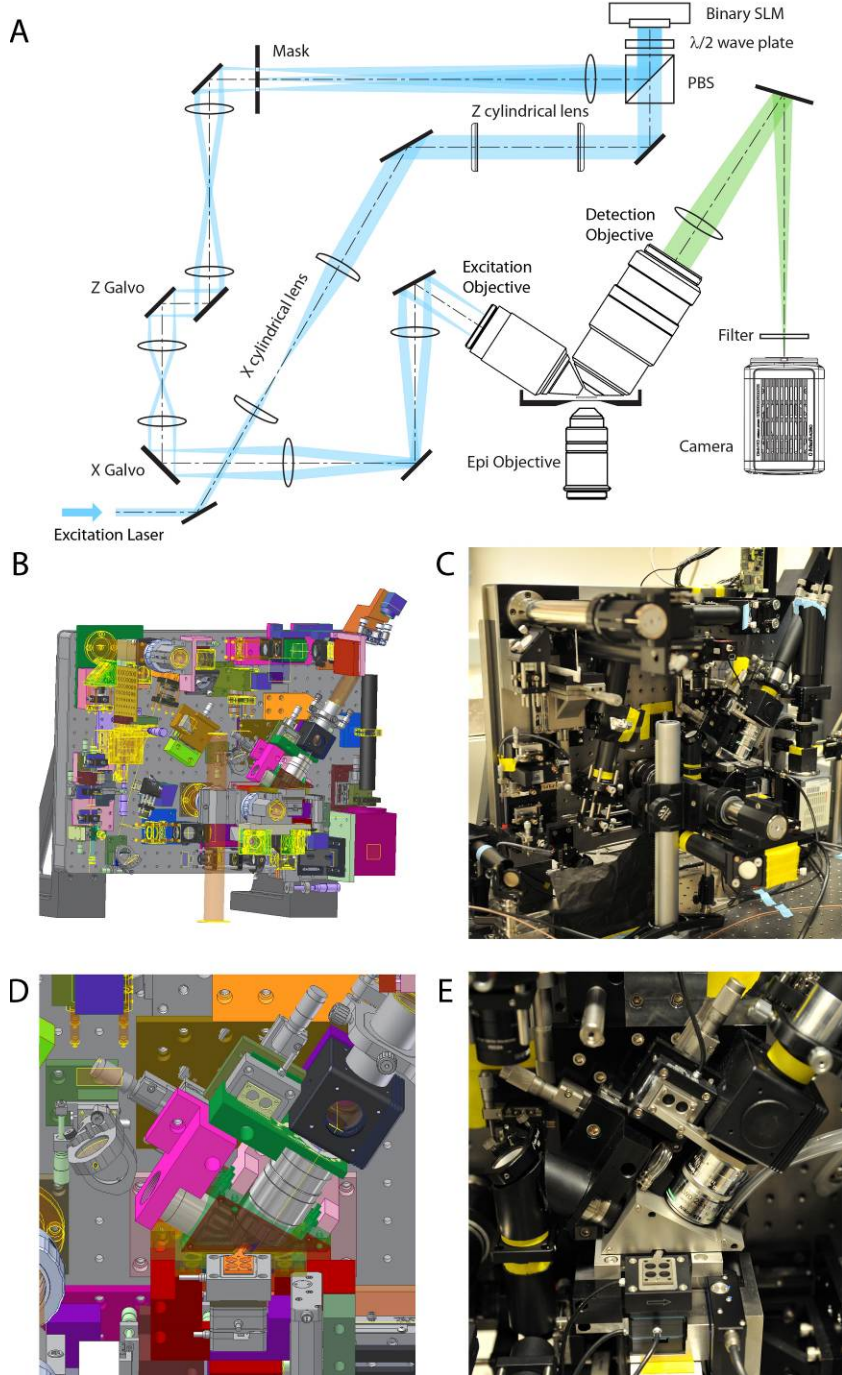


**Fig. S4. Schematic, mechanical design, and implementation of the lattice light sheet microscope.**

(A) Schematic of the optical path through the microscope. A linearly polarized circular input beam is stretched by a pair of cylindrical lenses in the  $x$  direction and compressed by another pair in the  $z$  direction, illuminating a thin stripe across the center of a binary, ferroelectric spatial light modulator (SLM), upon which the desired lattice pattern is projected. The light reflected from the SLM then passes through a transform lens, creating a Fourier diffraction pattern at an opaque mask containing a transparent annulus. The mask filters out unwanted diffraction orders and enforces maximum and minimum NA of illumination that dictate the  $y$  extent of the eventual lattice light sheet. The mask is serially conjugate to  $x$  and  $z$  galvanometers as well as the rear pupil of the excitation objective, so that the light sheet can be translated in  $x$  and  $z$  and rapid oscillated in  $x$  for the dithered mode of operation. The SLM itself is then conjugate to the sample plane, so that the lattice pattern projected on the SLM is imaged within the sample. The lattice light sheet generates fluorescence in a plane within the sample, which is imaged via a 1.1

NA detection objective and tube lens onto an sCMOS camera. Although the light sheet and objective can be translated in  $z$  to acquire a 3D volume, we more commonly use a piezoelectric flexure stage to translate the sample through the light sheet. (B) 3D solid model of the microscope. All components (except lasers) are mounted on an 18 x 24 inch breadboard which is in turn vertically mounted on an optical table. The sample itself is then horizontal in the shallow, media filled bath. (C) Photograph of the assembled microscope. (D, E) Magnified views of the sample chamber region, showing: the two objectives surrounded by temperature control blocks; the media bath; the sample holder; and the sample translation subassembly underneath.

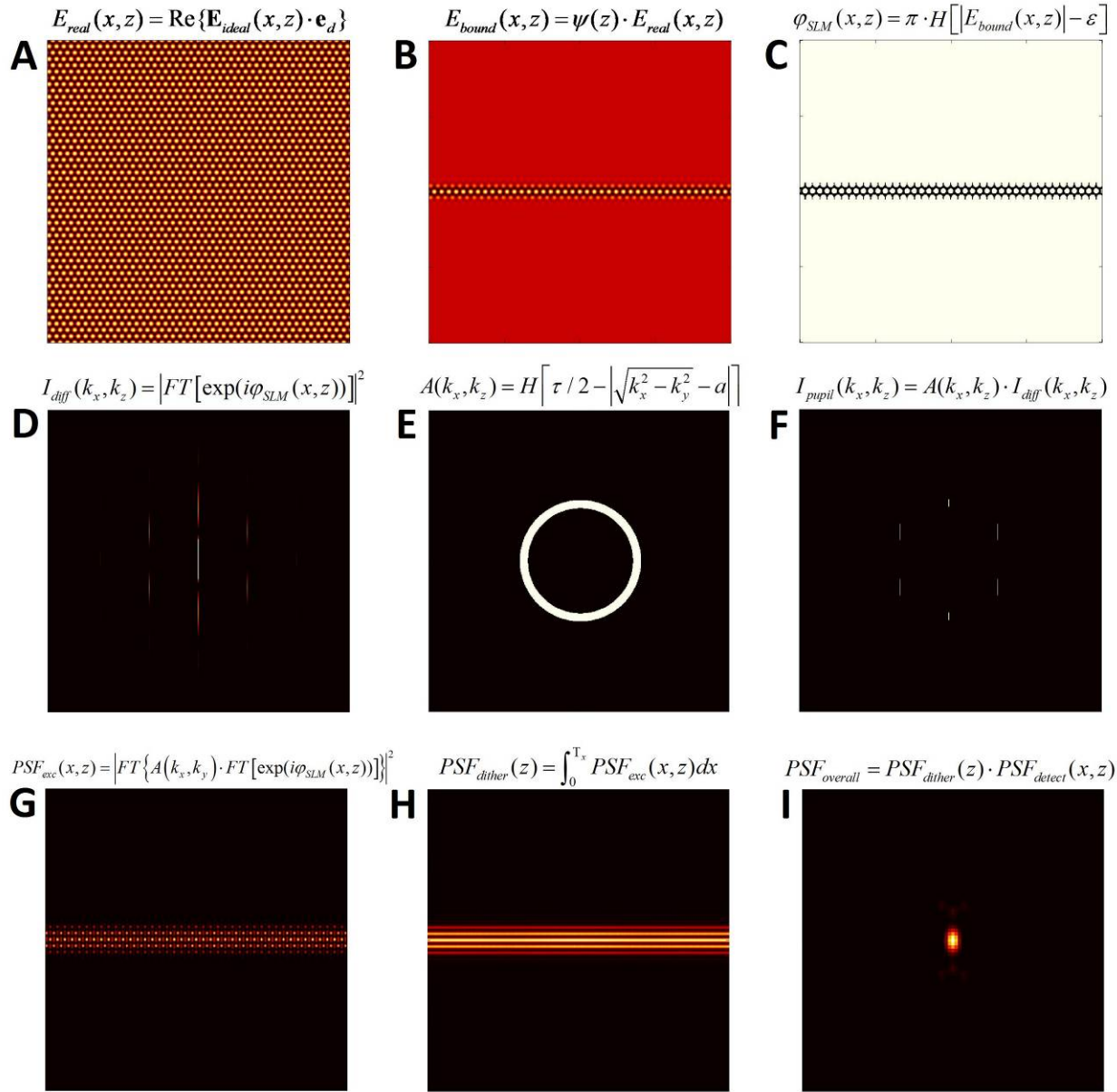


**Fig. S5. Generation of the SLM pattern for a specific lattice light sheet.** (A) Real part of the electric field  $E$  of an ideal 2D lattice serving as the seed for a particular desired lattice light sheet. (B)  $E$  field of the bound lattice obtained after multiplication by a bounding function  $\psi(z)$ . (C) SLM pattern created via  $0/\pi$  binarization of the bound lattice  $E$  field. (D) Predicted diffraction pattern impinging upon the annular mask. (E) Annular filter mask that is conjugate to the rear pupil of the excitation objective. (F) Predicted illumination pattern at the rear pupil. (G) Predicted  $xz$  excitation cross-section of the lattice light sheet. (H) Predicted cross-section of the dithered lattice light sheet. (I) Predicted overall PSF for the lattice light sheet in the dithered mode.

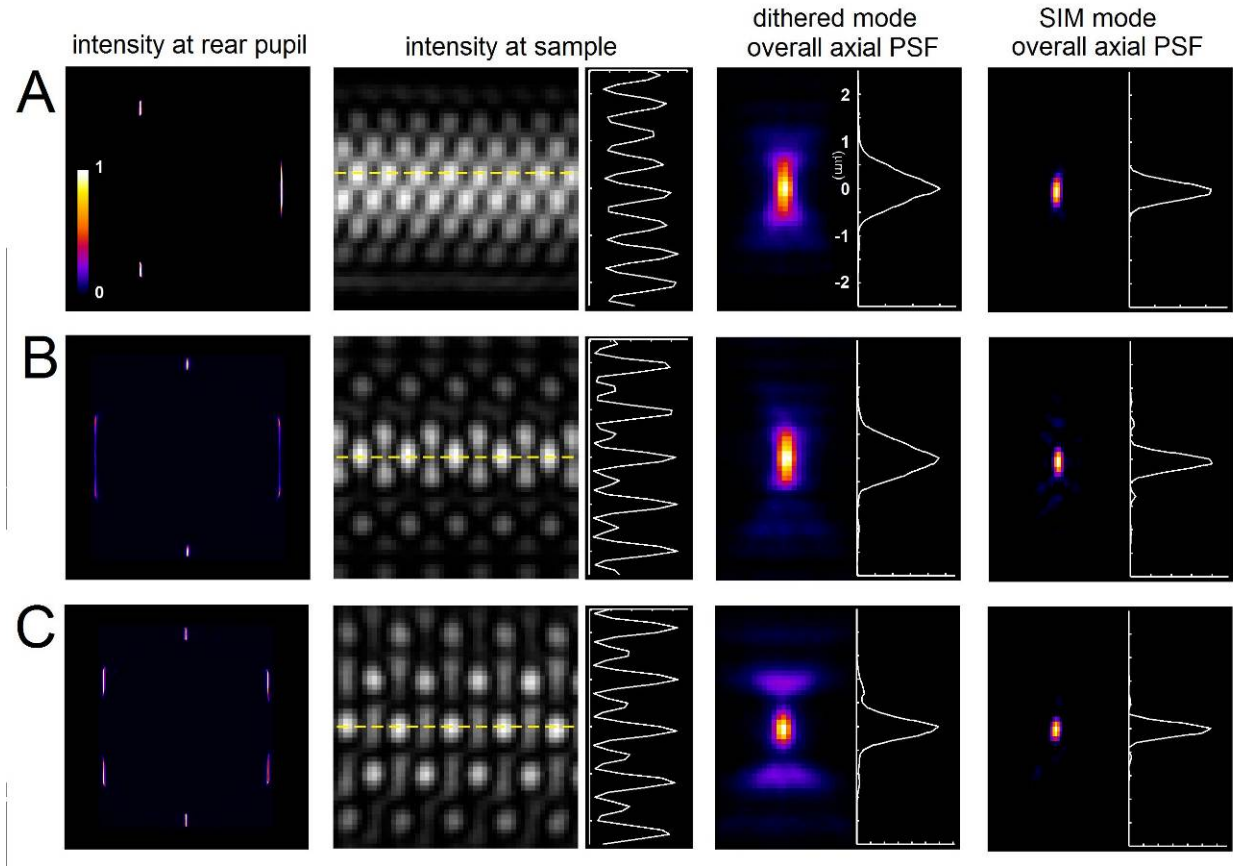


**Fig. S6. Experimental measurement of lattice light sheet parameters.** Experimentally measured parameters for light sheets derived from three different optical lattices. Columns, from left to right: the intensity pattern at the rear pupil of the excitation objective that produces the light sheet; the  $xz$  cross-sectional intensity profile of the lattice light sheet at the sample; the overall PSF in the  $xz$  plane for the dithered mode of operation; and the overall reconstructed PSF in the  $xz$  plane in the SIM mode of operation. Data in columns two, three, and four were measured using 100 nm fluorescent beads. **(A)** Fundamental hexagonal lattice, comprised of three wavevectors, optimized for fast SIM (*cf.*, fig. S3A). **(B)** Maximally symmetric fundamental square lattice, comprised of four wavevectors, optimized to confine excitation to a single plane, *e.g.*, for single molecule studies (*cf.*, fig. S2B). **(C)** Maximally symmetric fundamental hexagonal lattice, comprised of six wavevectors, optimized for high axial resolution in either the dithered or SIM modes (*cf.*, figs. S2C, S3C).

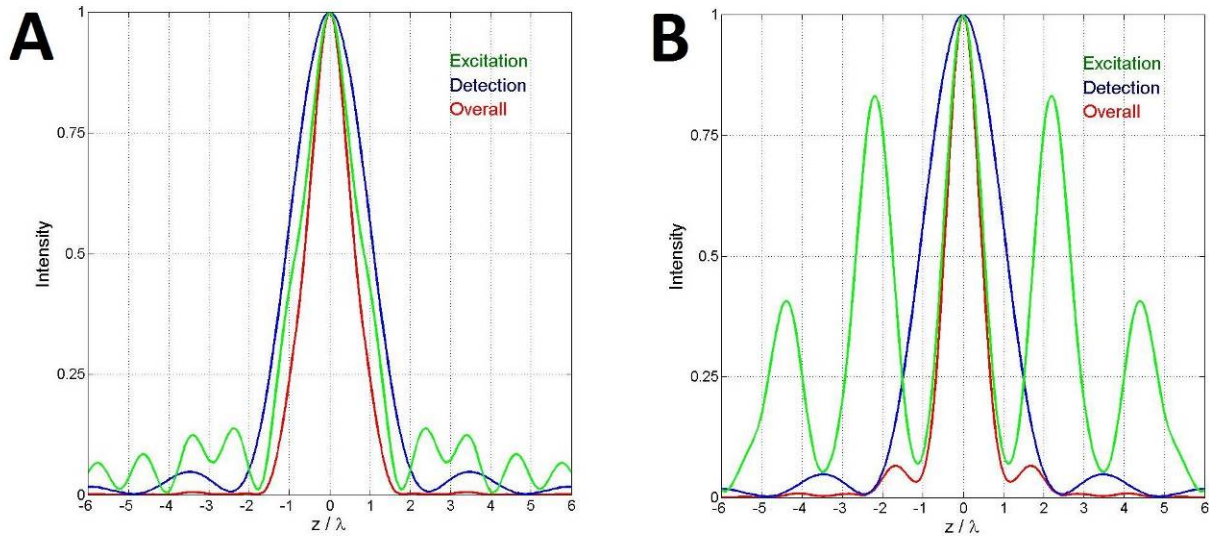


**Fig. S7. Axial confinement and point spread functions of two dithered lattice light sheets.** (A) Maximally symmetric first sparse square lattice optimized to confine the axial excitation (green) to a single plane. (B) Maximally symmetric fundamental hexagonal lattice optimized to minimize the axial width of the overall axial point spread function (red). Both cases assume restriction of the rear pupil illumination to an NA range of 0.57 to 0.65. NA 1.1 is assumed for the axial detection PSF (blue).

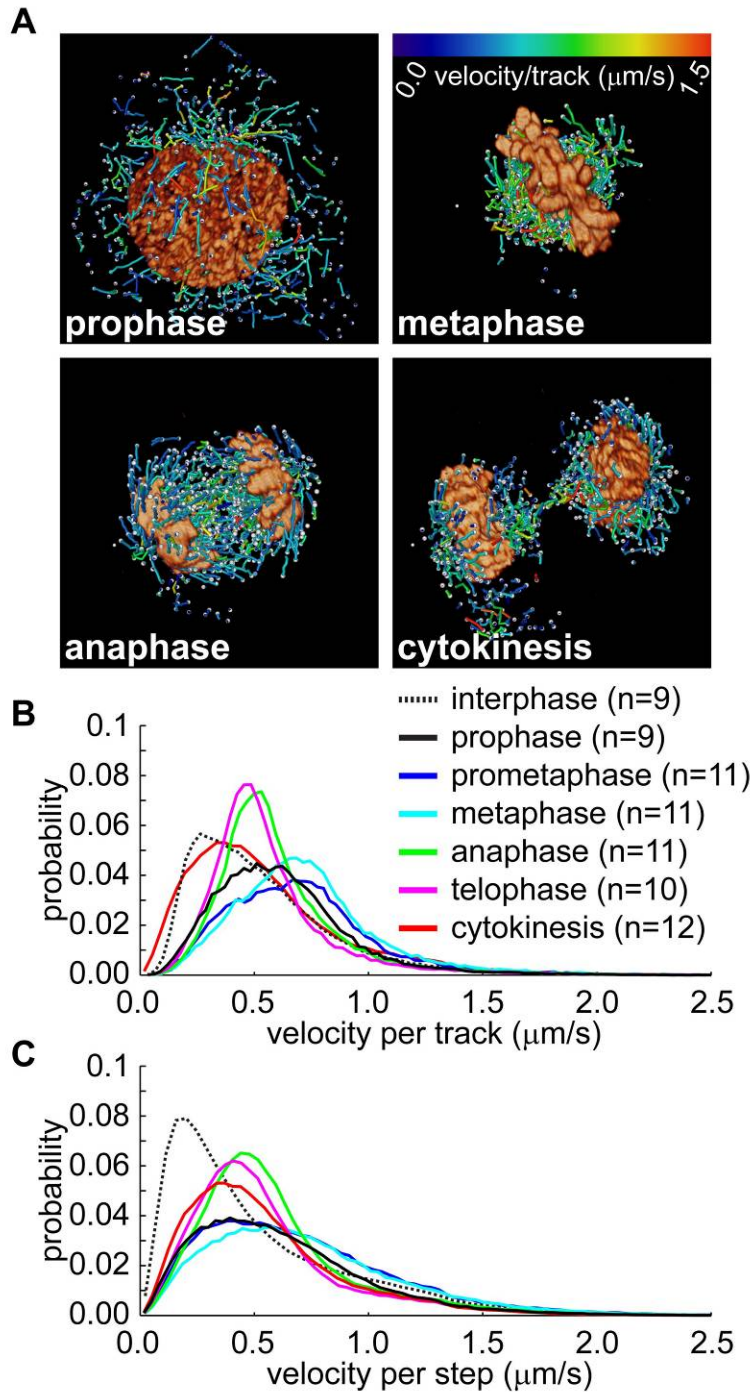


**Fig. S8. 3D quantification of microtubule growth during mitosis.** (A) Trajectories of the endpoints of growing microtubules in HeLa cells expressing GFP-EB1 at four different time points during division of a HeLa cell, color coded by velocity, from a 4D data set covering 500 time points. (B) Distributions of the mean velocity of each growth track, collated over nine to eleven different cells at seven different stages before and during mitosis. Velocities increase from interphase to metaphase, and then decrease back to the interphase level during cytokinesis. (C) Distributions of the velocities of the endpoints as measured between successive time points. Trends are the same as in (B).

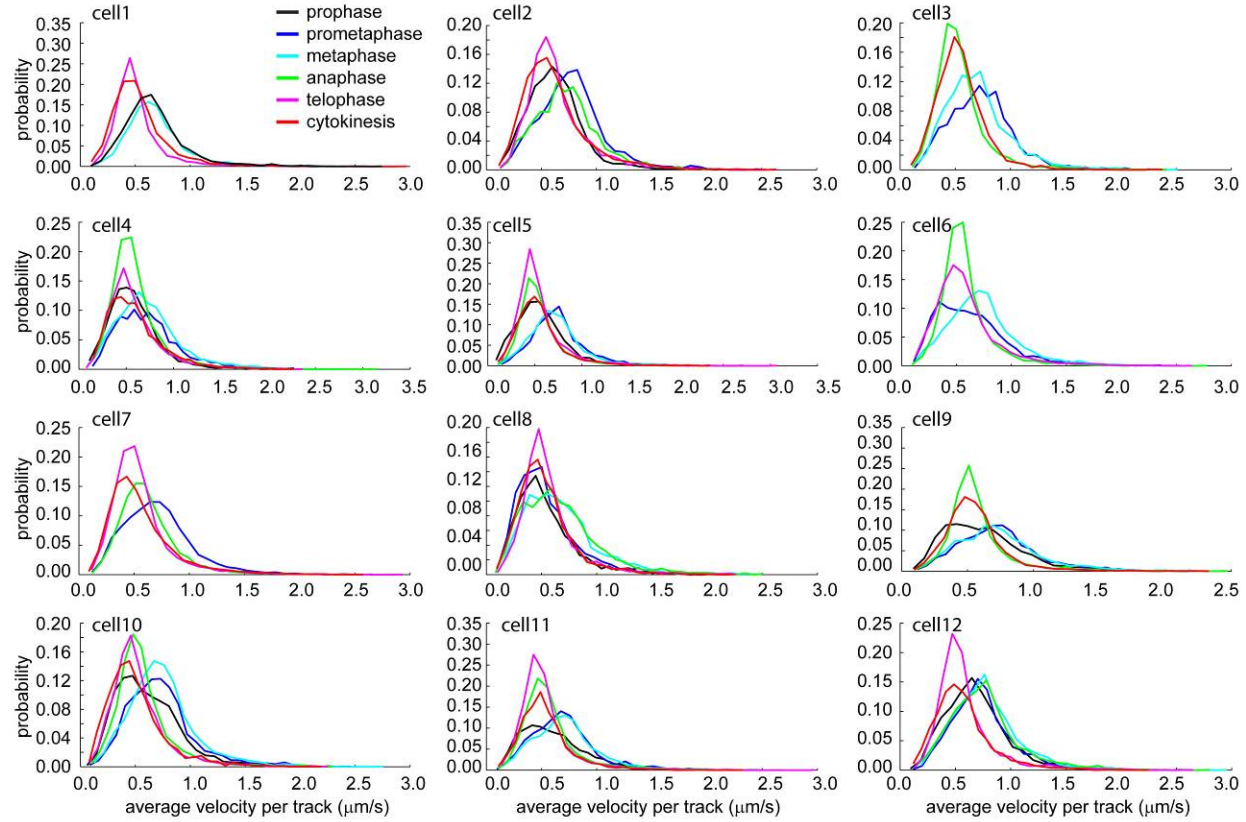


**Fig. S9. Microtubule growth rates in individual cells during mitosis.** Distribution of microtubule growth rates at different stages of mitosis show the same trends when compared across twelve different cells.

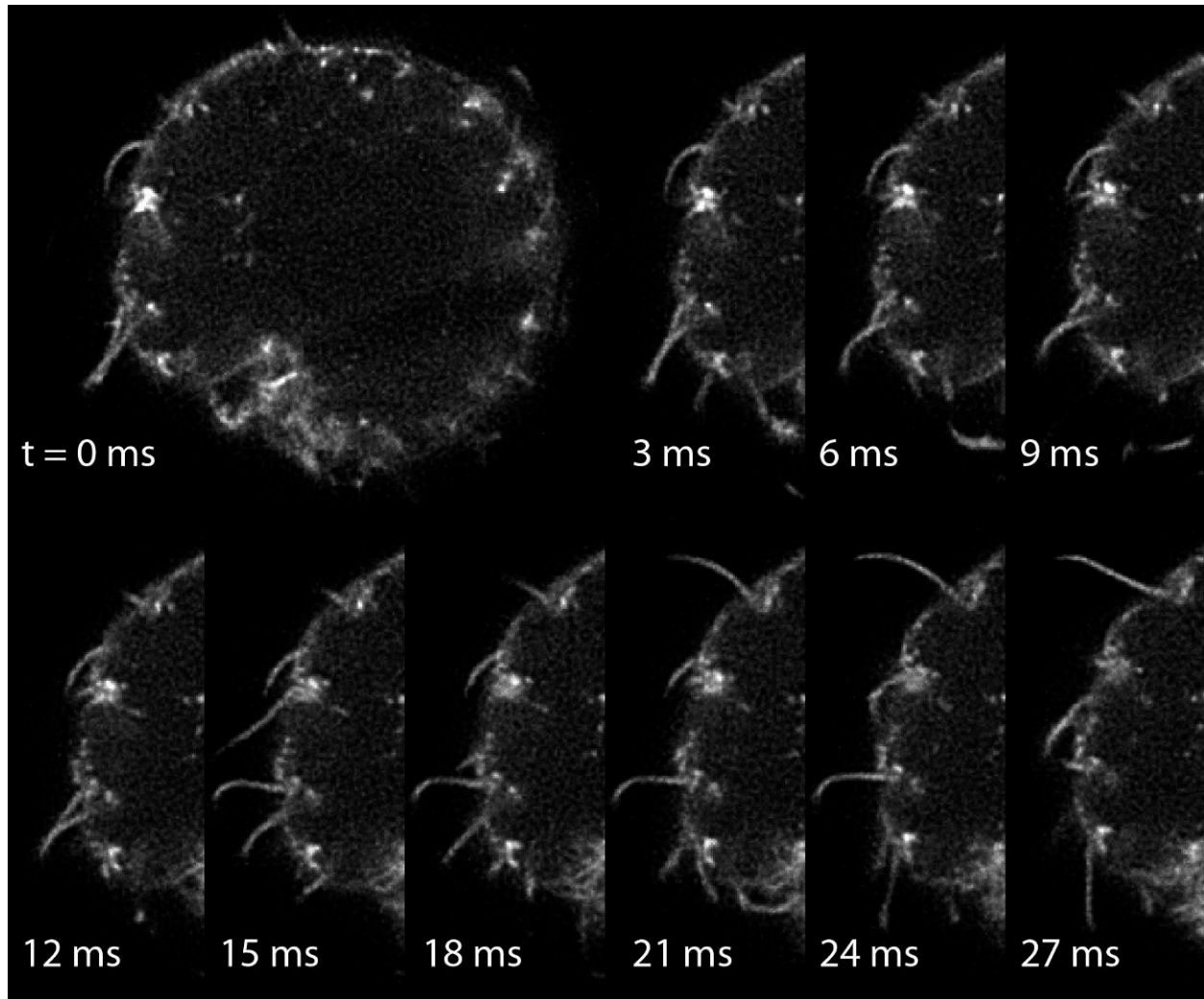


**Fig. S10. Cilia motion in *Tetrahymena*.** 2D imaging at a fixed plane through the protozoan *T. thermophila*. When the specimen is nearly at rest, imaging at 3ms intervals is fast enough to follow the shape and motion of beating cilia.

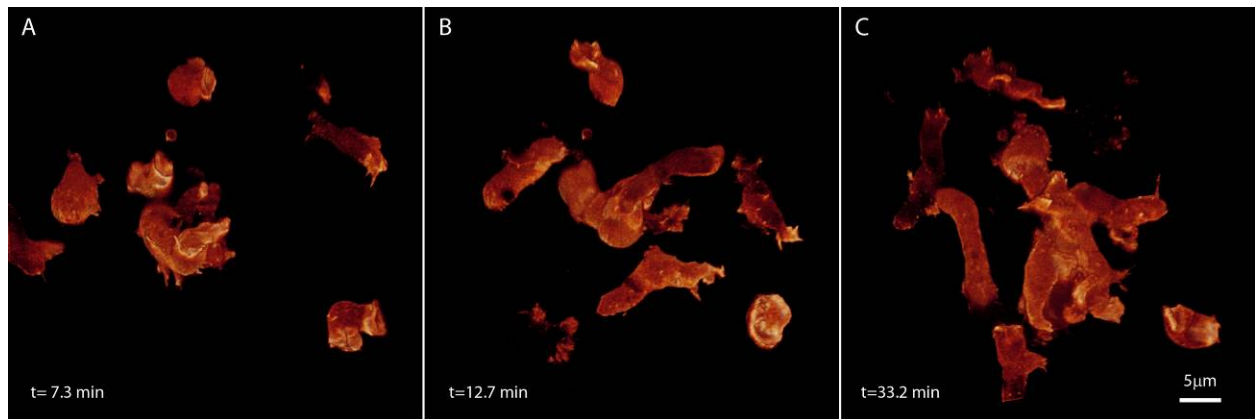


**Fig. S11. Initial aggregation of starved *D. discoideum*.** Volume renderings at three time points from a 4D data set of 300 time points showing the chemotaxis of starved amoeboid cells expressing RFP-LimE as they aggregate in the initial stages of forming a multicellular fruiting body.

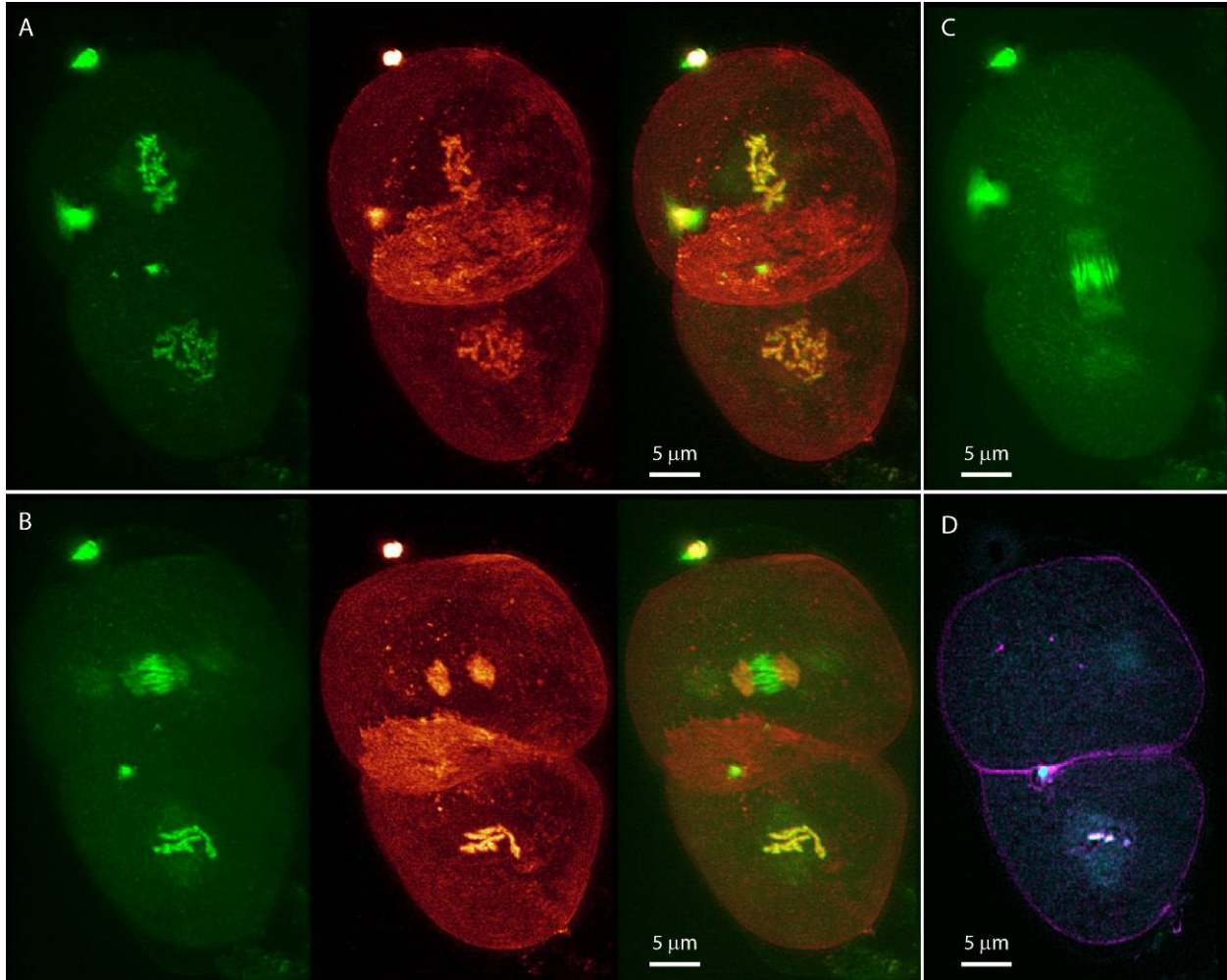


**Fig. S12. Distribution of AIR-2 during early embryogenesis of *C. elegans*.** (A) Volume renderings of GFP-AIR-2 localized at condensed chromosomes during prophase and metaphase at one time point from a 4D data stack covering 50 time points. Left to right: GFP-AIR-2, green channel; mCherry-H2B and PH (chromosomes and plasma membrane), red channel; overlay. (B) Volume renderings of GFP-AIR-2 present on microtubules in the spindle midzone of the AB cell and on the midbody, chromosomes, and the pericentriolar material at a slightly later time point. (C) Volume rendering of GFP-AIR-2 highlighting astral microtubules. A-C, also show AIR2, H2B, and PH localization at the polar bodies (bright spots at the top of the embryos). (D) 2D orthoslice showing the GFP-AIR-2 midbody remnant (magenta) in the extracellular space between the plasma membranes of AB and P1 cells after the first division.

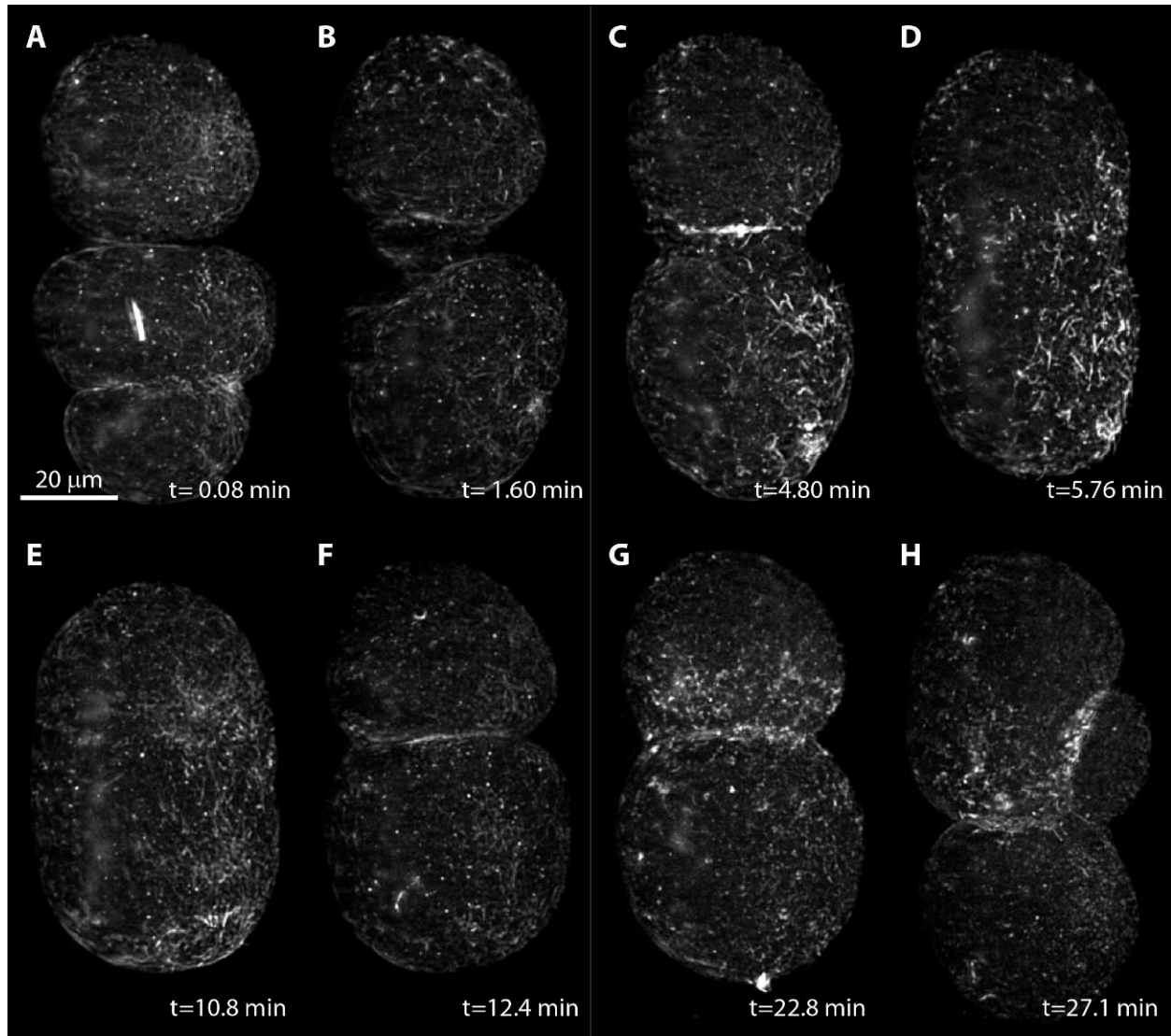


**Fig. S13. Distribution of actin during early embryogenesis of *C. elegans*.** Maximum intensity projections in an xy view of the top half of a developing embryo expressing GFP-Lifeact, at eight time points from a 4D data set covering 300 time points. (A) Single cell during pseudocleavage ingression, showing an intracellular actin comet. (B, C) Relaxation of the pseudocleavage furrow. (D) Bright cortical actin bundles present in maintenance phase during pronuclear meeting. (E) Smooth embryo, presumably near the time of nuclear centration or initial spindle displacement. (F) During and (G) after the first division. (H) After division of the AB cell.

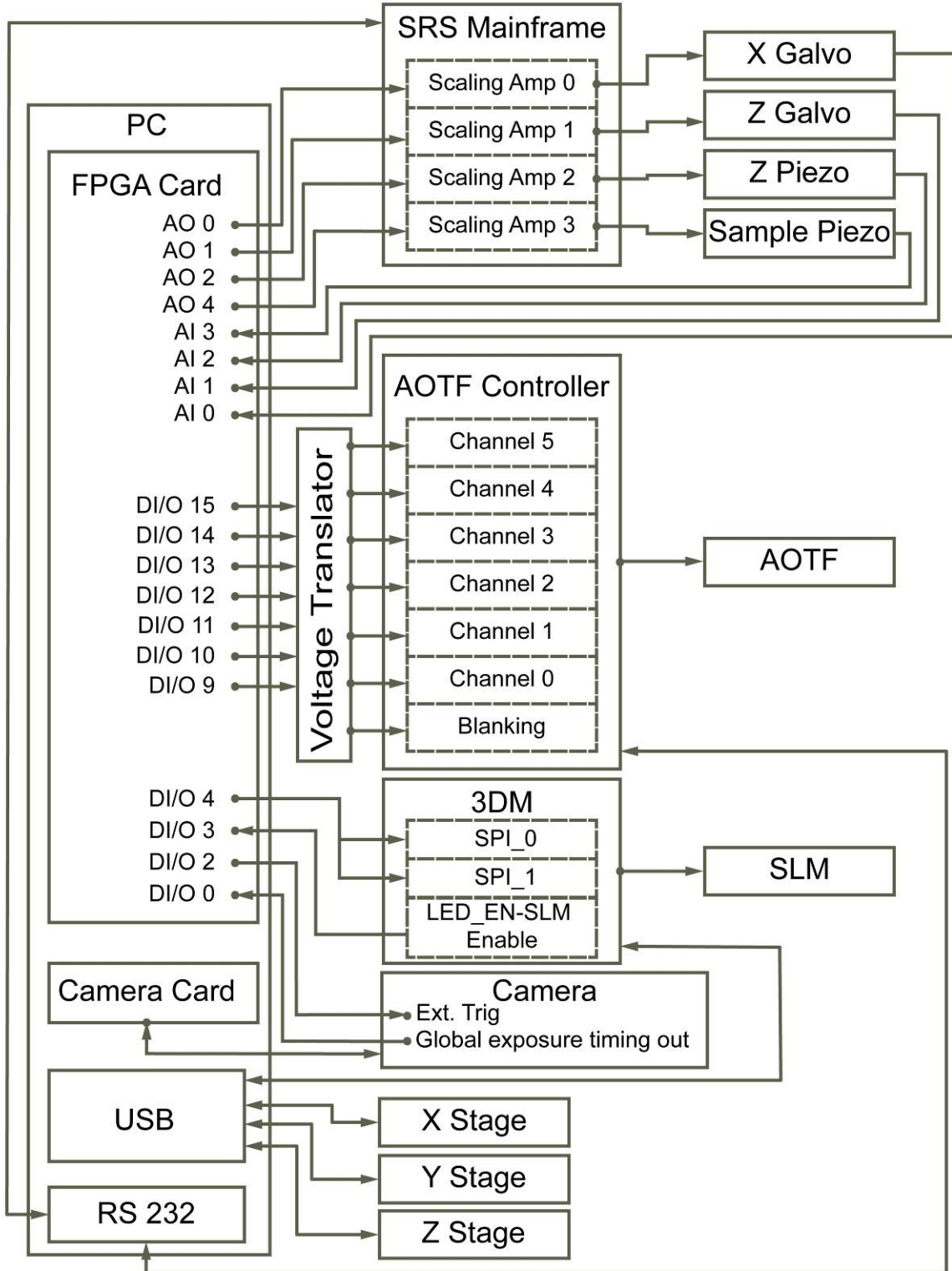


**Fig. S14. Control schematic for the microscope.** The SLM LED Enable output is used as the master clock source, but the FPGA provides the analog /digital outputs to control most of the other electronics critical to image acquisition. Additional boards in the computer receive the data from the sCMOS and inspection cameras, and control the sample positioning stages.

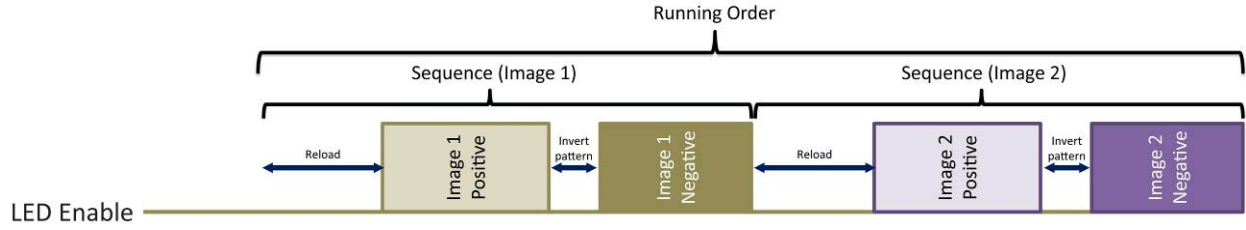


**Fig. S15. SLM Operation.** The SLM is loaded with a series of images known as a Running Order. Once triggered, these are displayed in order, with each image displayed first in positive ( $0/\pi$ ) and then negative ( $\pi/0$ ) form to preserve the ferroelectric liquid crystal. The desired diffraction pattern is produced with either form, but not during the transition between them, or when the next image in the Running Order is loaded. Thus, an LED Enable digital output is provided to signal to the FPGA those times when imaging can be performed.

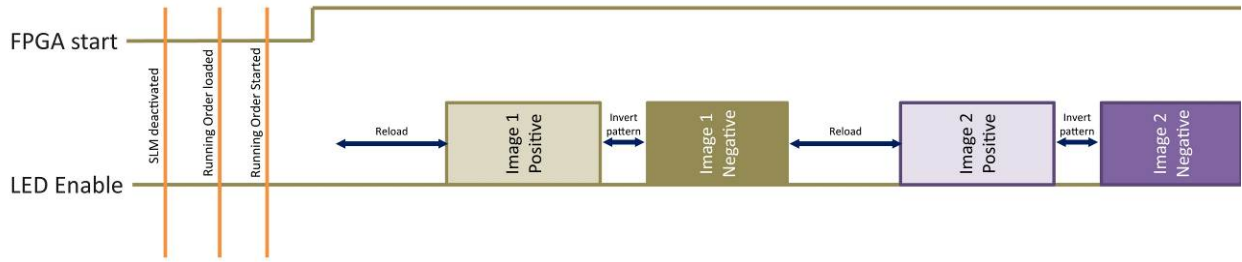


**Fig. S16. Initialization of the SLM.** The sequence of commands to load and then trigger a Running Order for the SLM.

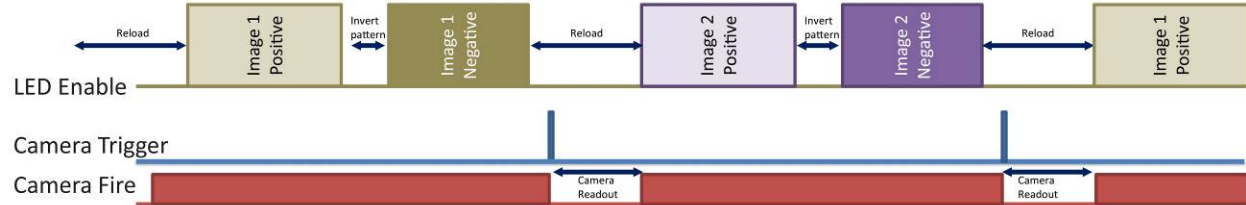


**Fig. S17. Camera Synchronization.** Timing of the external trigger and exposure sequences for the sCMOS image acquisition camera relative to the image display sequences on the SLM. To optimize speed, the camera readout occurs during the load of the next SLM image in the Running Order.

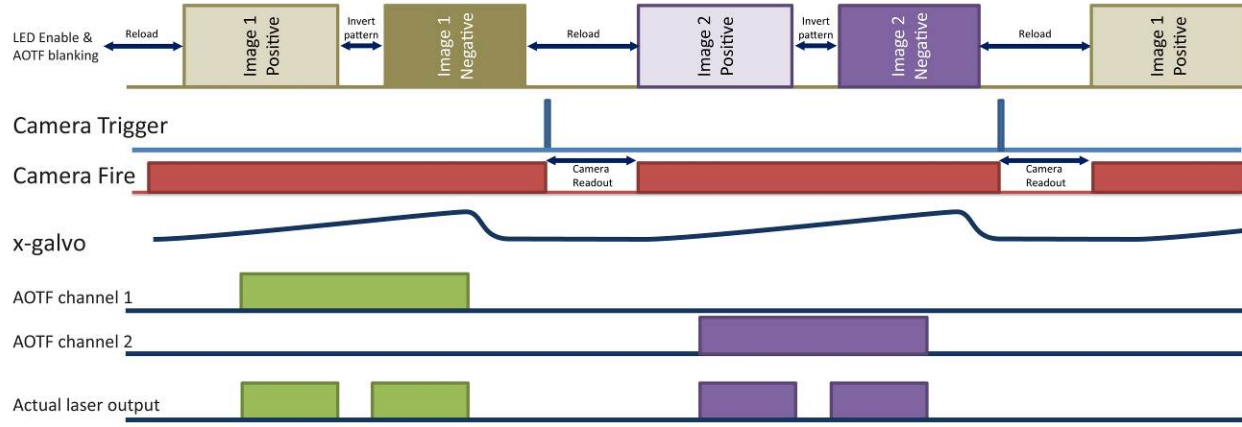


**Fig. S18. FPGA control signals.** Galvo and AOTF control signals as synchronized to the SLM during the acquisition of a single plane of data in two colors in the dithered mode.

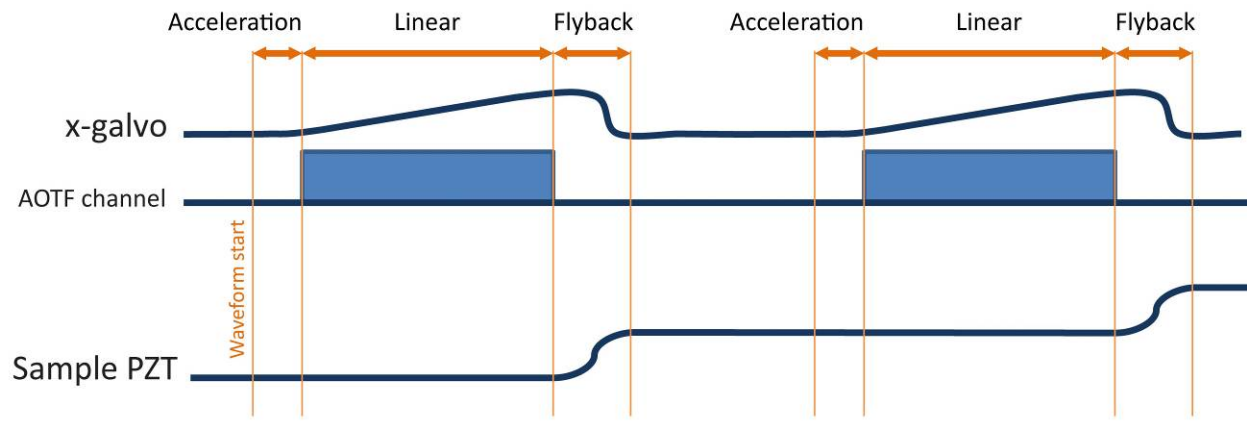


**Fig. S19. Galvo and piezo waveforms.** Acceleration, deceleration, and flyback of the galvos and piezos are controlled independently. Data acquisition occurs during the linear ramp (constant velocity) portion of the waveforms.

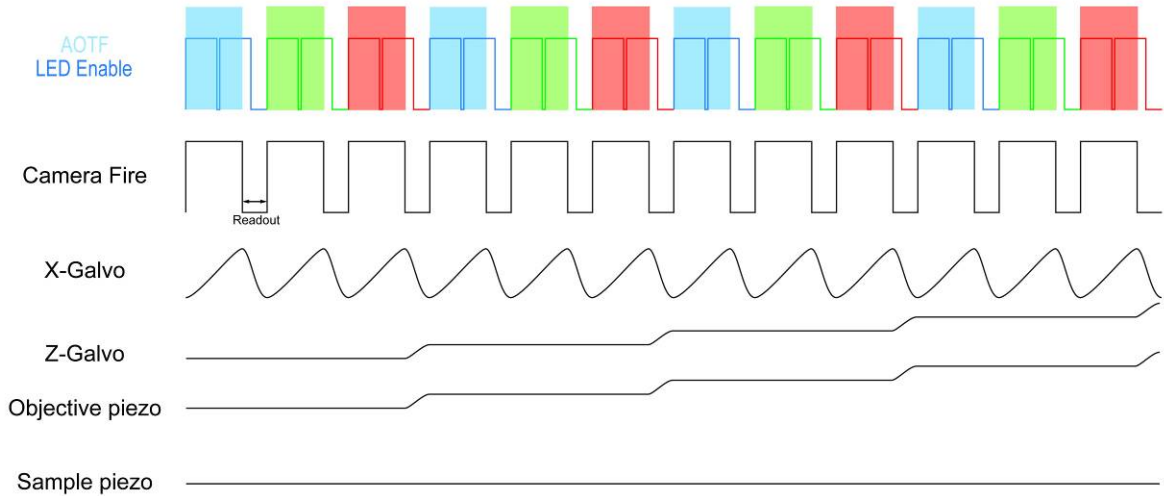


**Fig. S20.** Timing diagram for three color objective scan imaging with a dithered lattice light sheet.

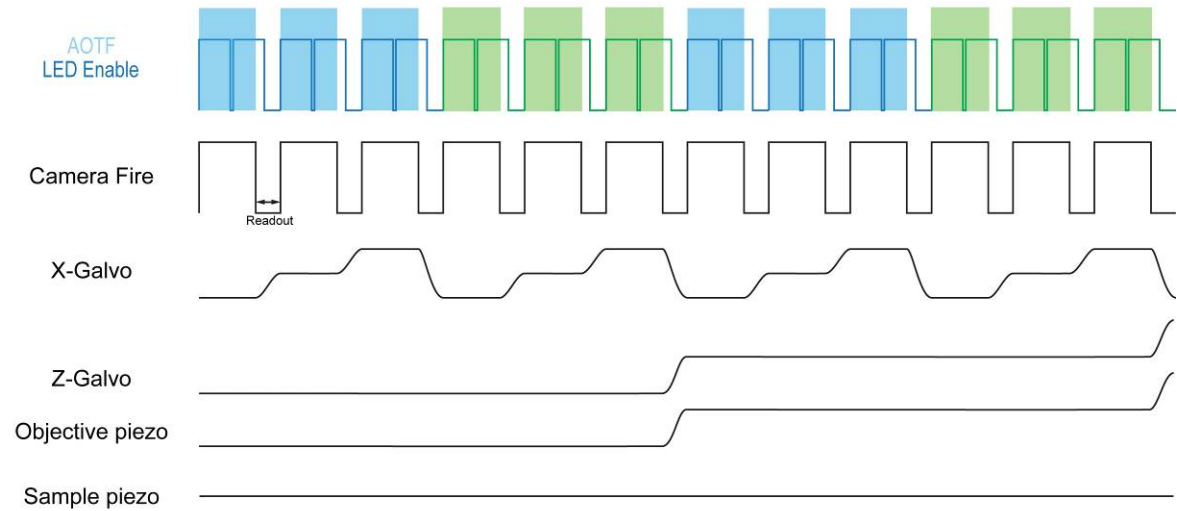


**Fig. S21.** Timing diagram for two color objective scan imaging in the three phase SIM mode.

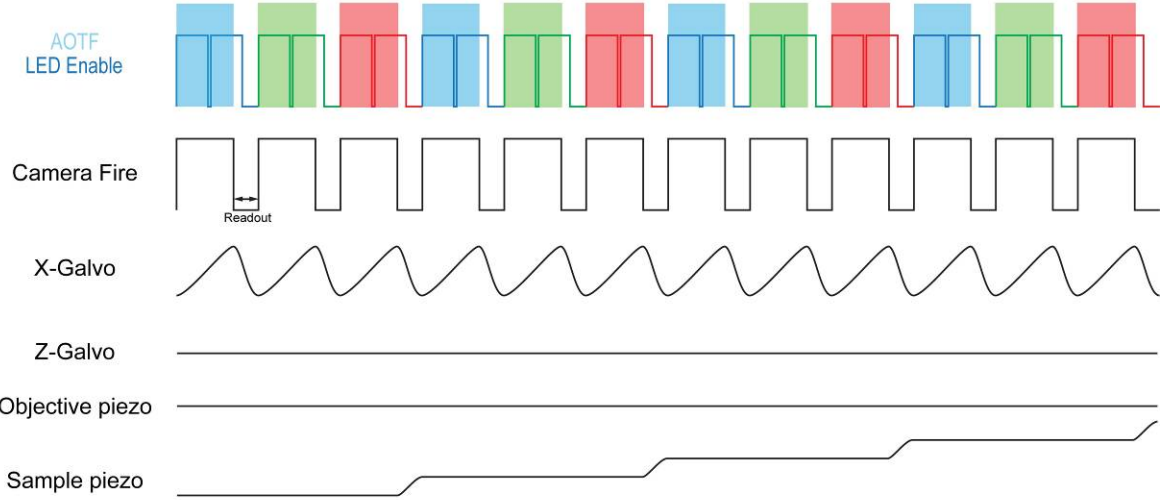


**Fig. S22.** Timing diagram for three color sample scan imaging with a dithered lattice light sheet.

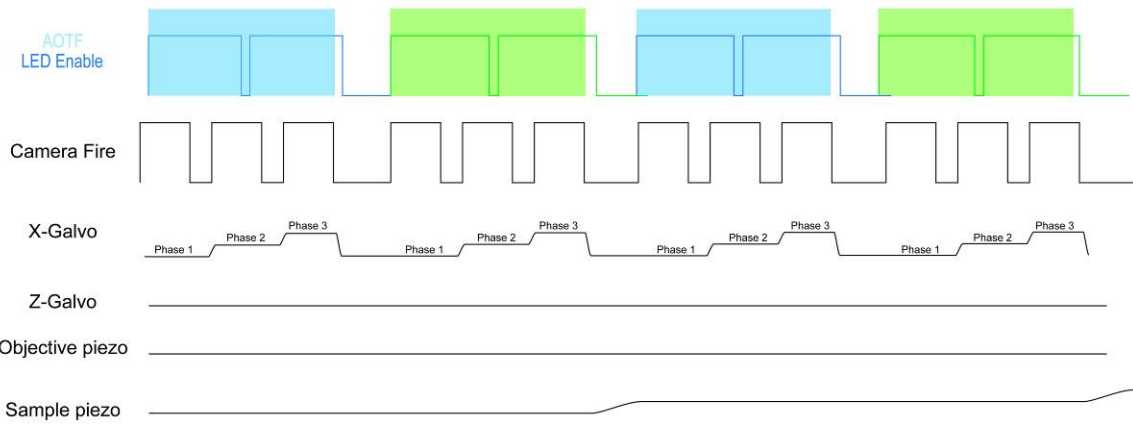


**Fig. S23.** Timing diagram for two color sample scan imaging in the three phase SIM mode.

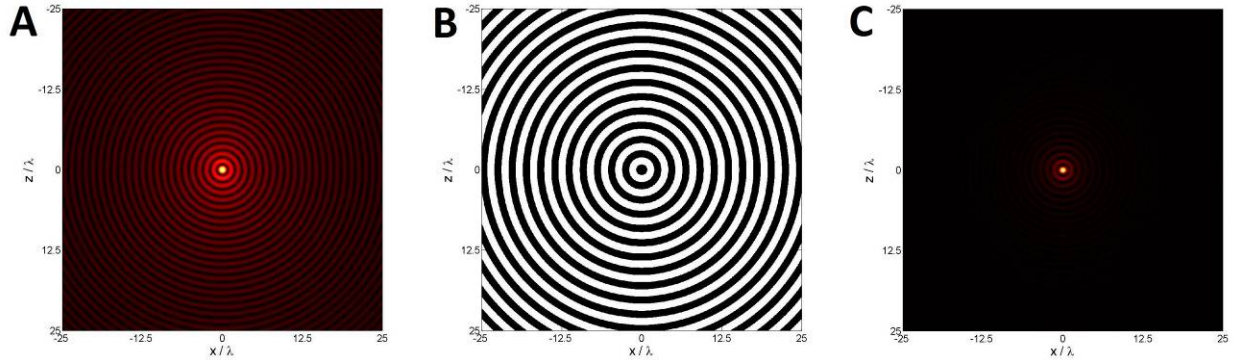


**Fig. S24. Properties of an ideal Bessel beam.** (A) Magnitude of the electric field  $E$  of an ideal Bessel beam. (B) Phase of the beam. Since  $E$  is real, the pattern consists of concentric rings of alternating opposite phase ( $0/\pi$ ). (C) Intensity of the beam.

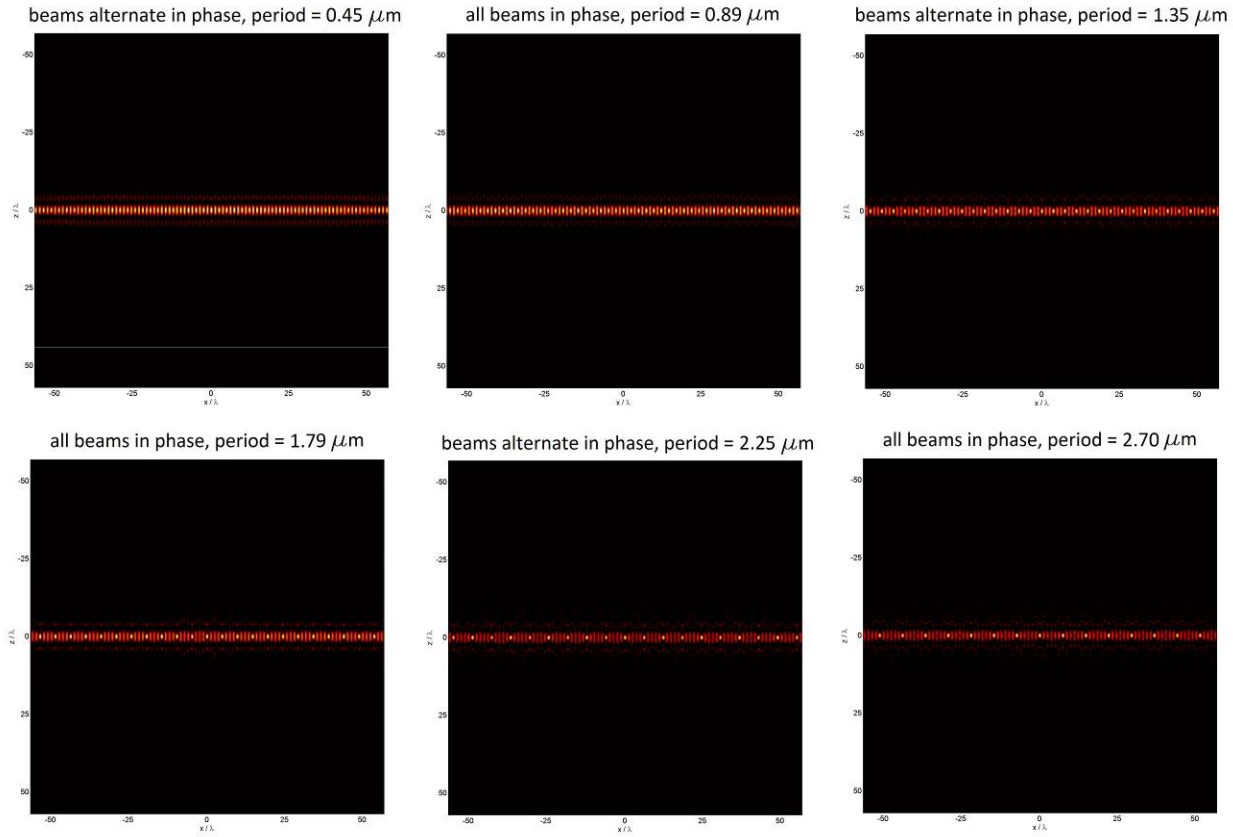


**Fig. S25. Tightly confined light sheets derived from linear arrays of coherent Bessel-Gauss beams.** The six shortest period linear arrays of Bessel-Gauss beams of either identical or alternate opposite phase that produce optimally confined light sheets (*cf.*, movie S18). At these specific periods, the side lobes of adjacent beams are in phase in the  $xy$  plane. All cases assume a maximum NA of 0.60, and a minimum NA of 0.54.

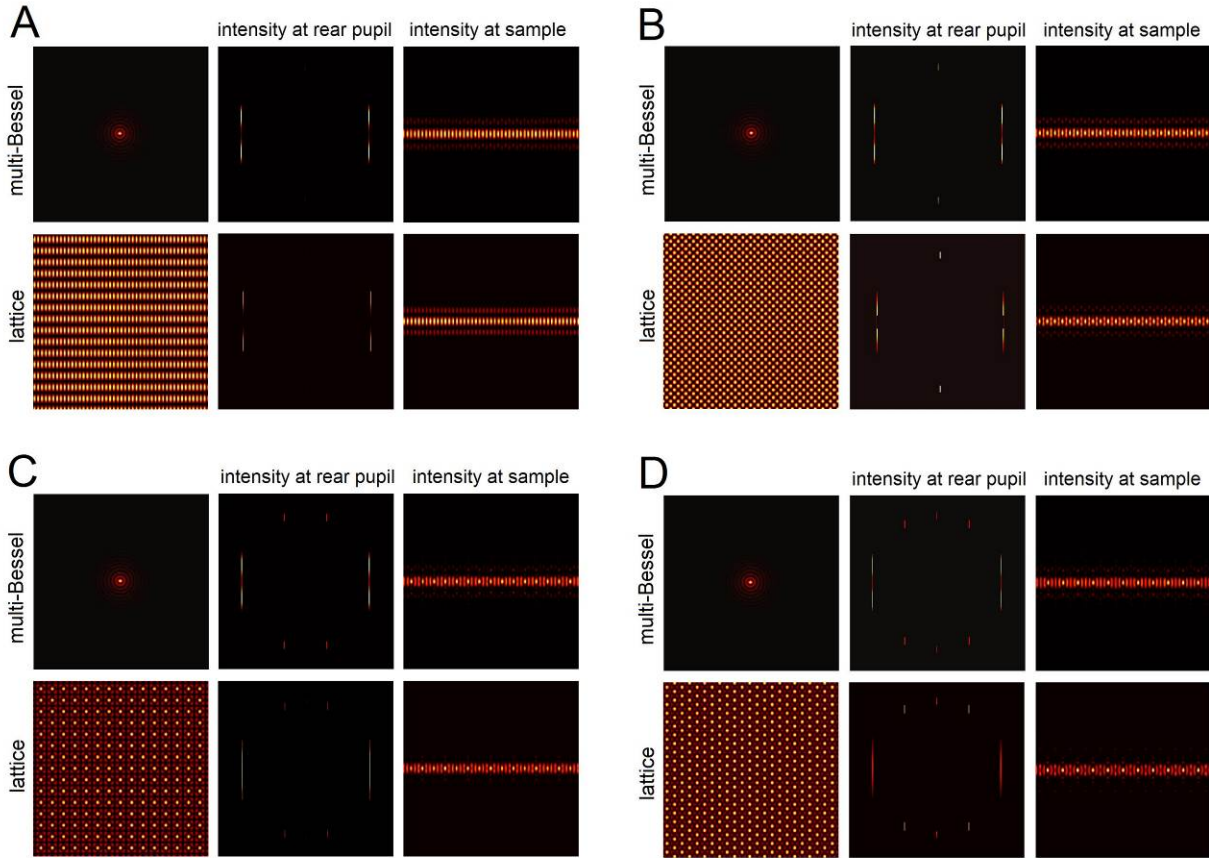


**Fig. S26. Optimally confined Bessel-Gauss beam arrays are bound 2D optical lattices.** The four shortest period linear Bessel-Gauss beam arrays of optimal confinement and the corresponding bound 2D optical lattices that produce nearly identical light sheets from nearly identical rear pupil illumination patterns. (A) 0.45  $\mu\text{m}$  period array of beams of alternating opposite phase, compared to a lattice light sheet derived from the maximally symmetric primitive rectangular lattice of aspect ratio 3:1. (B) 0.89  $\mu\text{m}$  period array of beams of identical phase, compared to a lattice light sheet derived from the maximally symmetric fundamental square lattice. (C) 1.35  $\mu\text{m}$  period array of beams of alternating opposite phase, compared to a lattice light sheet derived from the maximally symmetric first sparse square lattice. (D) 1.79  $\mu\text{m}$  period array of beams of identical phase, compared to a lattice light sheet derived from the maximally symmetric fundamental hexagonal lattice.

## SUPPLEMENTARY TABLE

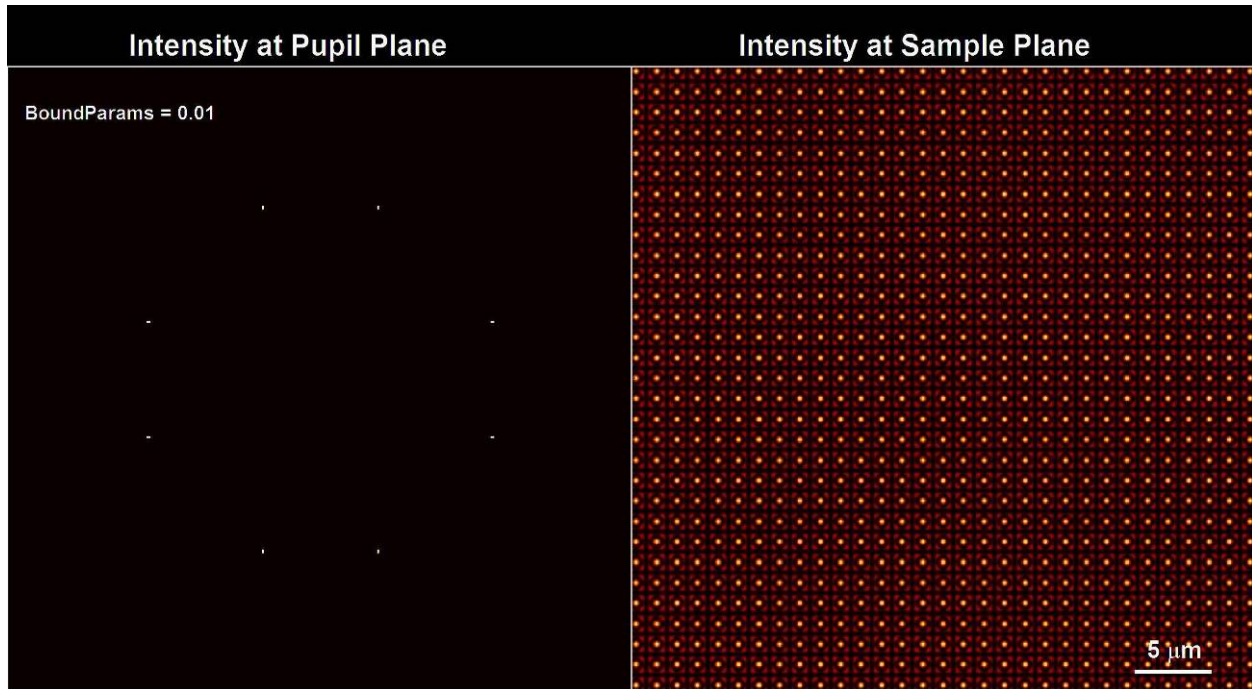
**Table S1.** Imaging conditions for all experiments.

	Mode	Sample (imaging T, °C)	Fluorescent label	Ext λ (nm)	Voxel volume (dx, dy, dz/ds nm³)	Image pixels (x, y, z)	Exposure time (ch1, ch2...) (# time pts) (image + test)	Power (μW)	Excitation N.A. (outer, inner) beam length (μm)	Photo-bleaching correction
Fig 2A	hex lattice 5 phase SIM sample scan	HeLa (37)	mEmerald-LifeAct	488	72x104x190/350	512x256x150 RAW 512x869x150 DSKW	5ms 3.40pts (3.75s+3.75s)	93	0.55 , 0.48 15	Image J – histogram matching
Fig 2B	single Bessel 5 phase SIM sample scan	HeLa (37)	mEmerald-LifeAct	488	72x104x190/350	512x256x150 RAW 512x869x150 DSKW	20ms 3.2pts (15s+1.5s)	93	0.55 , 0.48 15	Image J – histogram matching
Fig 2C	hex lattice dithered	HeLa (37)	mEmerald-LifeAct	488	104x104x240/443	512x256x150 RAW 512x815x150 DSKW	5ms 3.00pts (0.75s+0.75s)	93	0.55 , 0.48 15	Image J – histogram matching
Fig 2D	single Bessel dithered	HeLa (37)	mEmerald-LifeAct	488	104x104x240/443	512x256x150 RAW 512x815x150 DSKW	5ms 3.00pts (0.75s+0.75s)	93	0.55 , 0.48 15	Image J – histogram matching
Fig 3ABC	square lattice dithered single plane	Mouse ESC spheroid (37)	Halo-Tag TMR-SOX2	560	100x100	512x512	10ms 1000pts	900	0.55 , 0.44 10	no
Fig 3FGH	square lattice dithered	U2OS (25)	Dendra2-LaminA	560	100x100x271/500 10x10x20 PALM	512x256x61 RAW 512x512x61 DSKW 3001x2001x301 PALM	95ms 31658pts	5000	0.5 , 0.42 15	no
Fig 4A	square lattice dithered objective scan	HeLa (37)	GFP-EB1 tagRFP-H2B	488 568	104x104x200	320x320x101	5ms,5ms 400pts (1s+0.25s)	13,10	0.50 , 0.42 15	no
Fig 4B	square lattice dithered	LLCPK1 (37)	mEmerald-Calnexin mCherry-H2B mitotracker deep red-mito	488 568 640	104x104x190/350	576x256x201 RAW 576x847x201 DSKW	5ms 3.00pts (3s+0.5s)	6,3,12	0.50 , 0.42 15	99.9 <sup>th</sup> percentile
Fig 4C	square lattice dithered objective scan	Tetrahymena (25)	GFP-scramblase	488	104x104x1000	512x512x151	3ms 1250pts (0.15s+0.11s)	6	0.4 , 0.325 20	99.9 <sup>th</sup> percentile
Fig 5ABC	square lattice dithered objective scan	T cell/Target cell (37)	mEmerald-LifeAct(T cell) tagRFP-PM(target)	488 568	104x104x200	512x300x131	5ms,5ms 150pts (1.0s+1s)	20,10	0.55 , 0.48 15	no

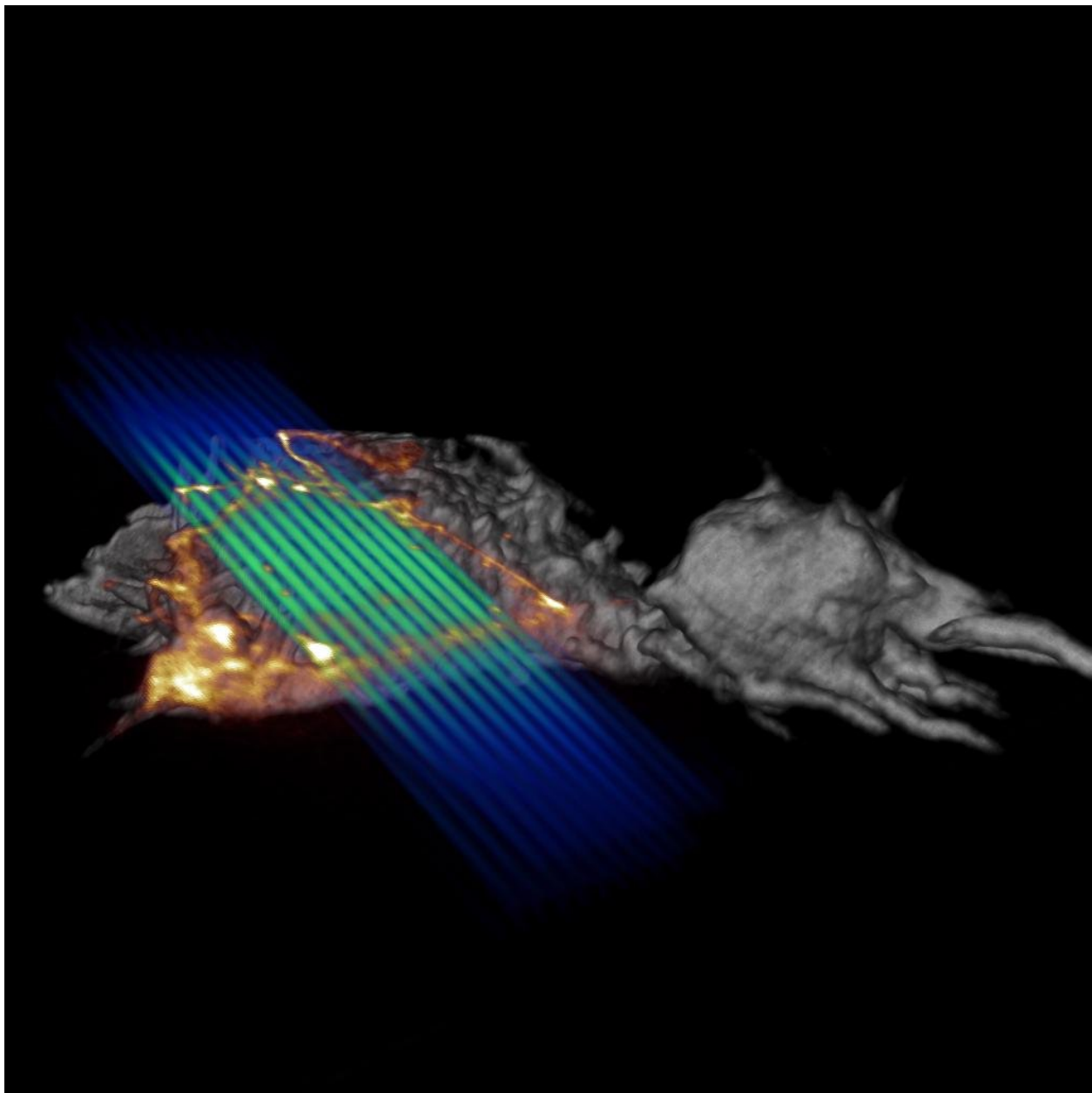
Fig 5DEF	square lattice dithered objective scan	HL60/collagen (37)	FITC-collagen mCherry-Utrophin	488 568	104x104x250	672x352x141	5ms,5ms 250pts (1.3s+0.1s)	20, 10	0.4, 0.325 20	Image J – histogram matching
Fig 6A	square lattice dithered objective scan	C elegans (25)	GFP-AIR2 mCherry-PM + H2B	488 568	104x104x300	512x416x11	50ms,50ms 62pts (11s+52s)	53, 33	0.50, 0.442 20	Image J – histogram matching
Fig 6B	square lattice dithered objective scan	C elegans (25)	GFP Lifeact	488	104x104x300	576x352x51	95ms 369pts	NM	0.4, 0.325 20	99.9 <sup>th</sup> percentile
Fig 6C	square lattice dithered sample scan	Drosophila (25)	eGFP-Cadherin RFP-moesin	488	100x100x206/328	896x652x158 RAW 896x1087x158 DSKW	20ms,20ms 841pts (5.05s+3s)	NM	0.4, 0.325 20	no
Fig 6D	square lattice dithered sample scan	Drosophila (25)	eGFP-myosin	488	100x100x206/328	896x512x263 RAW 896x1237x263 DSKW	15ms 1000pts (4.56s+0.5s)	NM	0.4, 0.325 20	99.9 <sup>th</sup> percentile
Fig 6EF	square lattice dithered sample scan	Drosophila (25)	eGFP-sGMCAmCherry-Sos	488 560	100x100x206/328	1024x512x263 RAW 1024x1237x263 DSKW	20ms,20ms 639pts (7.98s+4s)	NM	0.4, 0.325 20	no
Fig S8, S9	square lattice dithered objective scan	HeLa (25)	GFP-EB1 RFP-H2B	488 568	104x104x200	320x320x101	5ms,5ms 400pts (15s+0.25s)	13,10	0.50, 0.42 15	no
Fig S10	square lattice dithered single plane	Tetrahymena (25)	GFP-scramblase	488	104x104	512x512	3ms 18000pts	6	0.4, 0.325 20	no
Fig S11	square lattice dithered sample scan	Starving dicty (25)	GFP-LimE	488	104x104x240/443	672x352x201 RAW 672x1100x201 DSKW	10ms 400pts (2s+8s)	13	0.4, 0.325 20	Image J – histogram matching
Fig S12	square lattice dithered objective scan	C elegans (25)	GFP-AIR2 mCherry-PM + H2B	488 568	104x104x300	512x416x11	50ms,50ms 62pts (11s+52s)	53,33	0.50, 0.442 20	Image J – histogram matching

Fig S13		Corresponding to Fig6B						
Mov 1	square lattice dithered sample scan hex lattice 5 phase SIM sample scan	HeLa (37)	mEmerald-LifeAct	488	104x104x190/350	512x256x150 RAW 512x697x150 DSKW	5ms 100pts (3.75s+3.75s)	93      0.55 , 0.48 15
Mov 2	square lattice dithered objective scan	HeLa (37)	mEmerald-LifeAct	488	72x104x190/350	512x256x150 RAW 869x512x150 DSKW	5ms 750pts (0.75s+0.25s)	3      0.55 , 0.48 15
Mov 3	square lattice dithered objective scan	Dicty (25)	GFP-microtubules	488	104x104x200	512x320x151	10ms 1460pts (1.5s+0.5s)	10      0.4 , 0.325 20
Mov 4								Image J – histogram matching
Mov 5								Image J – histogram matching
Mov 6								Image J – histogram matching
Mov 7								Image J – histogram matching
Mov 8								Image J – histogram matching
Mov 9	square lattice dithered sample scan	HL60 (37)	GFP-LifeAct	488	104x104x210/388	672x252x201 RAW 672x908x201 DSKW	5ms 143pts (1s+0.25s)	10      0.55 , 0.48 15
Mov 10								no
Mov 11								Corresponding to FigS12
Mov 12								Corresponding to FiggB
Mov 13								Corresponding to FiggD
Mov S3								Corresponding to Fig2A and Fig2B
Mov S4								Corresponding to Fig2A and Fig2B

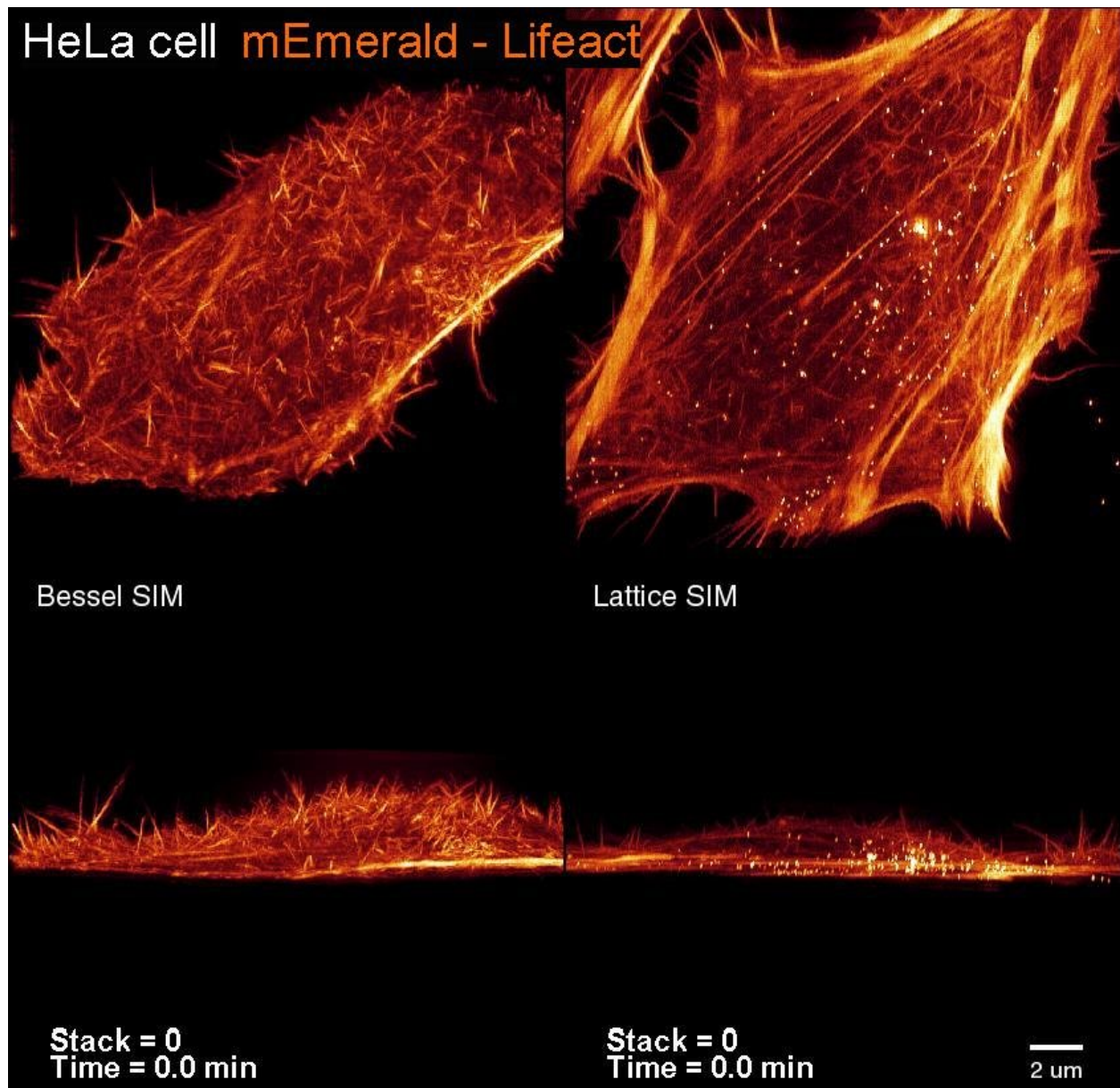


**CAPTIONS FOR SUPPLEMENTARY MOVIES**

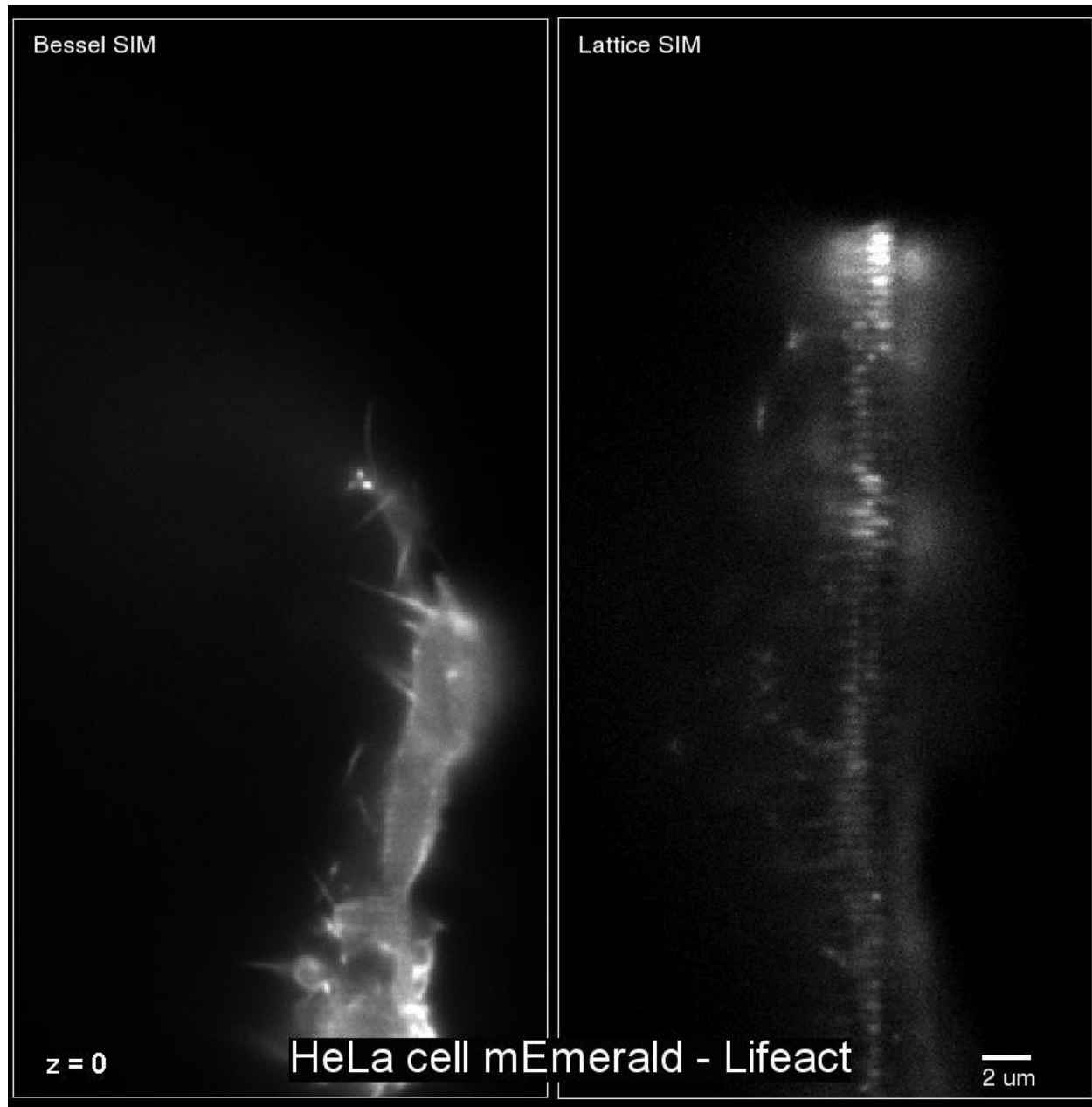
**Movie S1.** Transition from an infinite 2D optical lattice to an axially bound lattice light sheet, as seen in views of the illumination pattern in the rear pupil of the excitation objective (left) and the cross-sectional intensity profile of the resulting light sheet at the specimen (right).



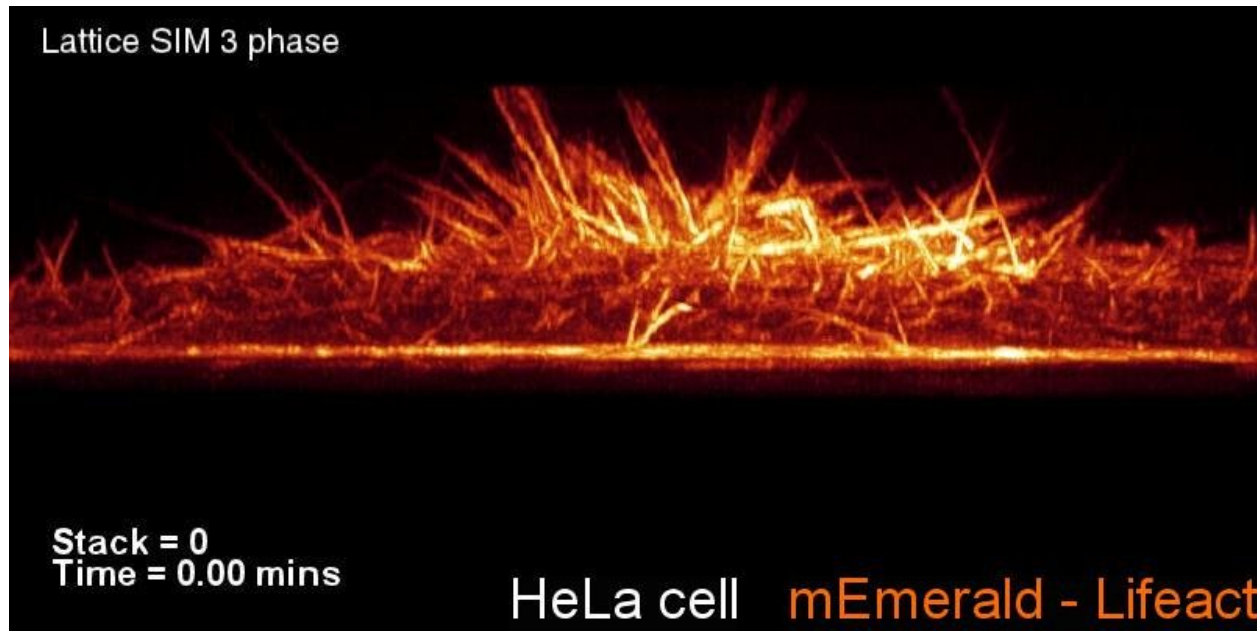
**Movie S2.** Animation of the image acquisition process, showing a lattice light sheet (blue/green) intersecting a cell (gray) to produce fluorescence (orange). As the cell is swept through the light sheet, a series of 2D images of the fluorescence are recorded to build up a 3D image of the cell. The lattice is dithered in its patterned direction to mimic a continuous light sheet.



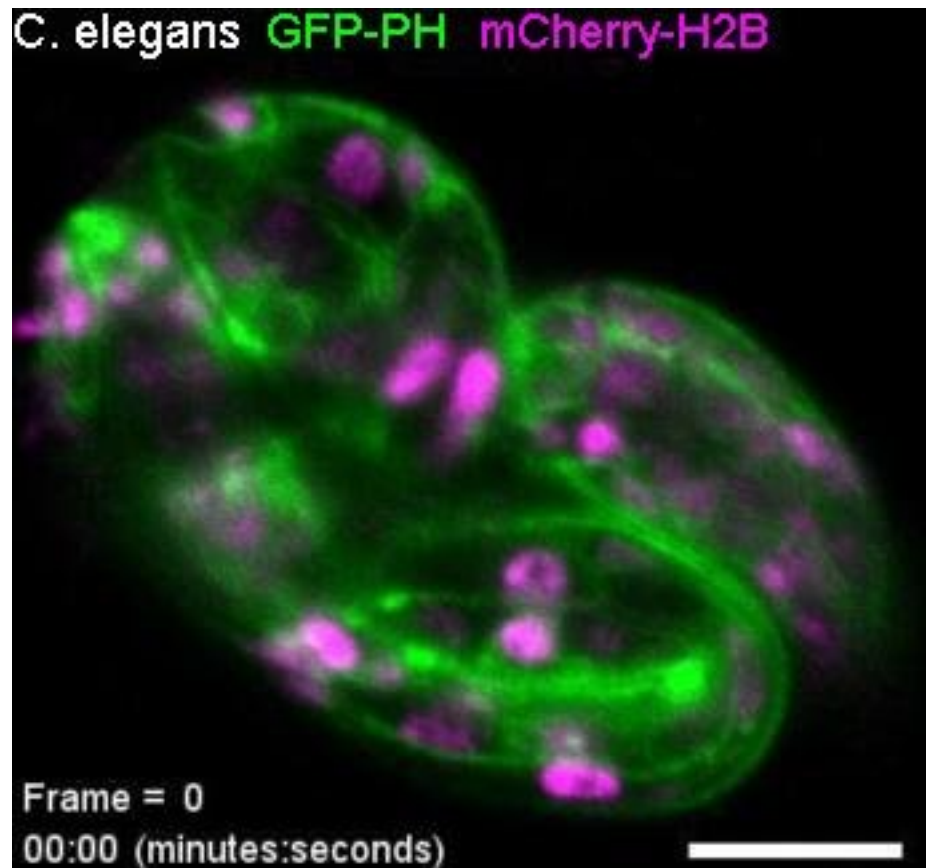
**Movie S3.** Top and side view volume renderings of HeLa cells expressing mEmerald-Lifeact, demonstrating the higher speed and reduced phototoxicity of the lattice light (right) compared to Bessel beam plane illumination (left) when each is applied to super-resolution structured illumination microscopy (SR-SIM).



**Movie S4.** Raw 2D image frames during acquisition of a 3D data volume in the SR-SIM mode for two HeLa cells expressing mEmerald-Lifeact, demonstrating the higher modulation amplitude and lower background obtained with a lattice light sheet (right) as opposed to a stepped Bessel beam (left).

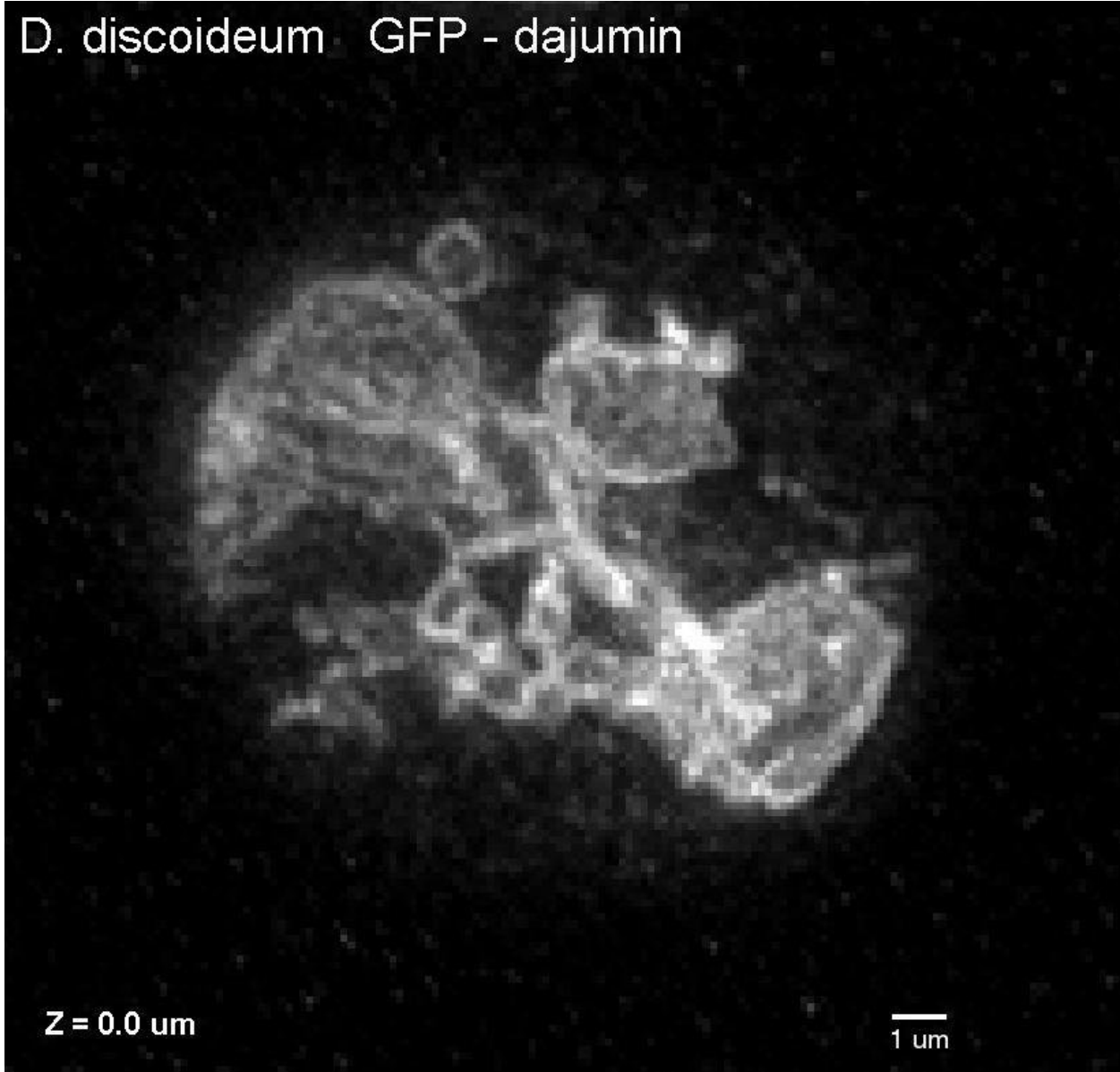


**Movie S5.** Side view volume rendering of filopodia dynamics at 4.0 sec intervals on the dorsal surface of a HeLa cell expressing mEmerald-Lifeact, acquired in the SR-SIM mode using a three phase hexagonal lattice light sheet.

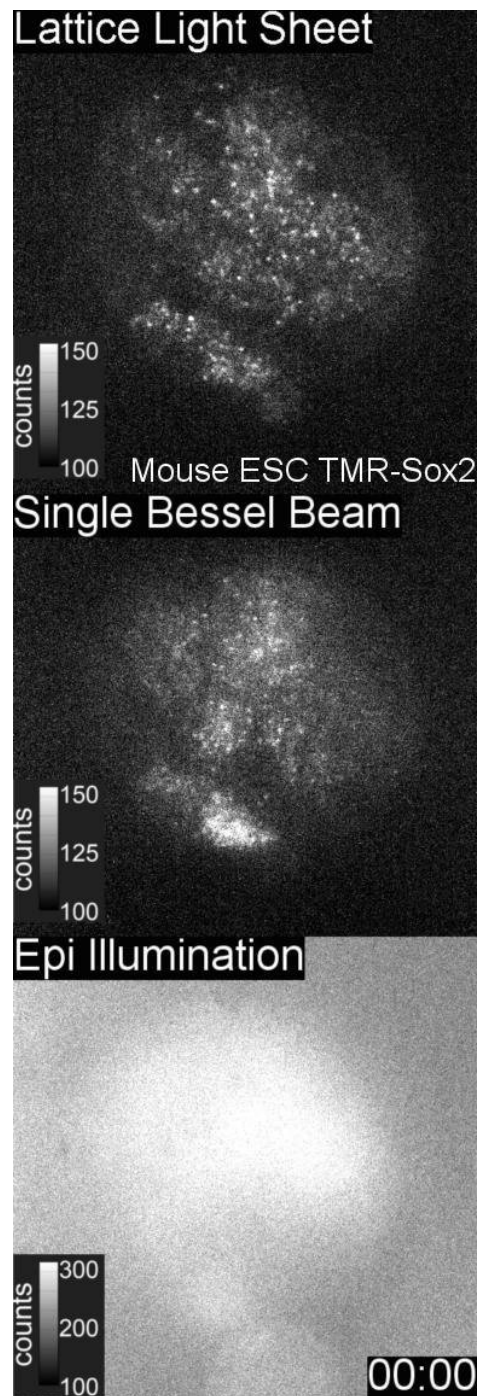


**Movie S6.** Rapid muscle contractions in a *C. elegans* embryo in the three-fold stage, with labeled GFP-PH domains (green) and mCherry-histones (magenta), as recorded in a single 2D optical section at 50 frames/sec. Scale bar, 10  $\mu$ m.

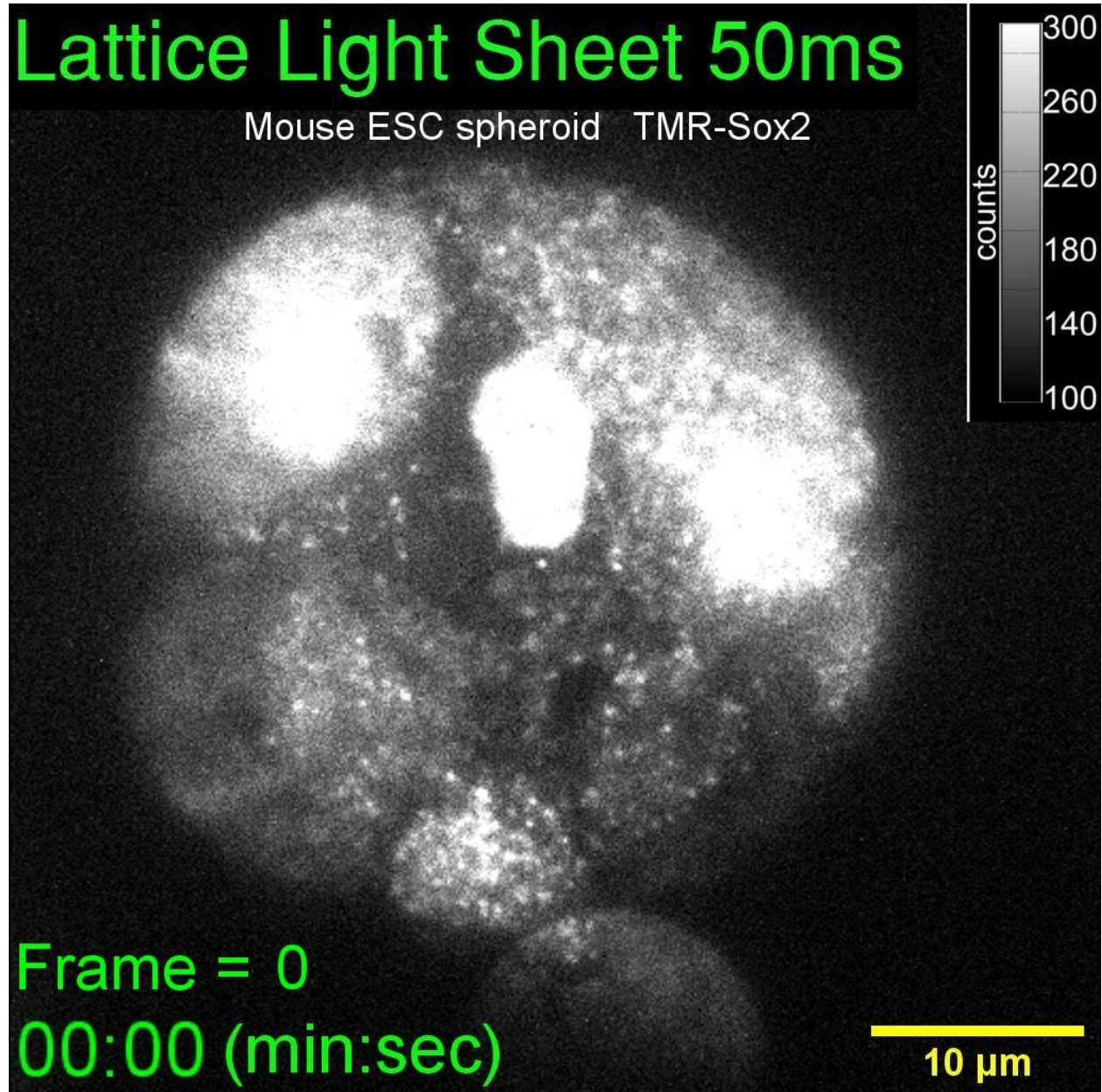
D. discoideum GFP - dajumin



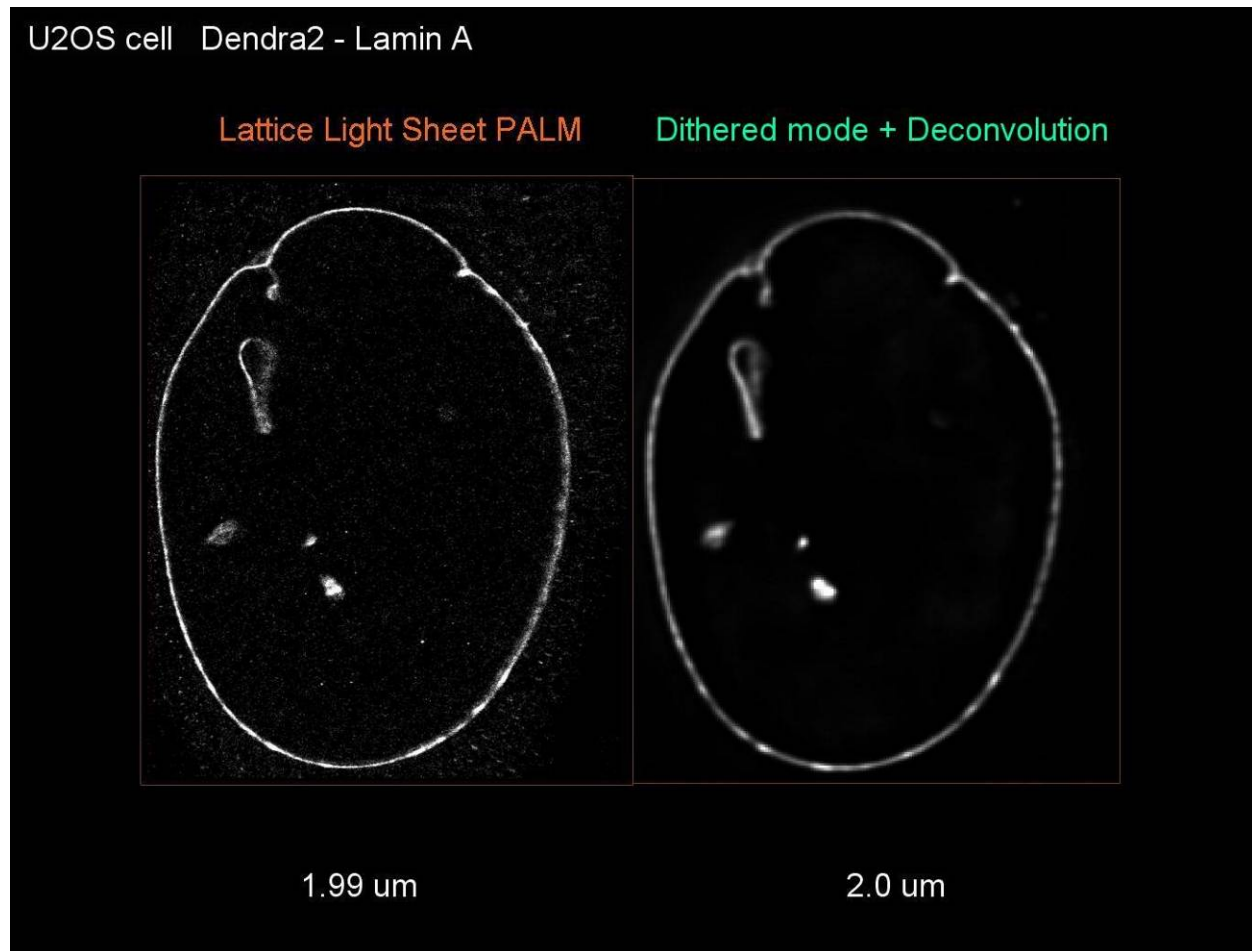
**Movie S7.** Volume rendering of GFP-dajumin in a *D. discoideum* cell, highlighting the rapid dynamics of the osmoregulatory contractile vacuole network over 400 time points at 0.6 sec intervals. A slight rocking is present in the viewer perspective during the time lapse to illustrate 3D depth.



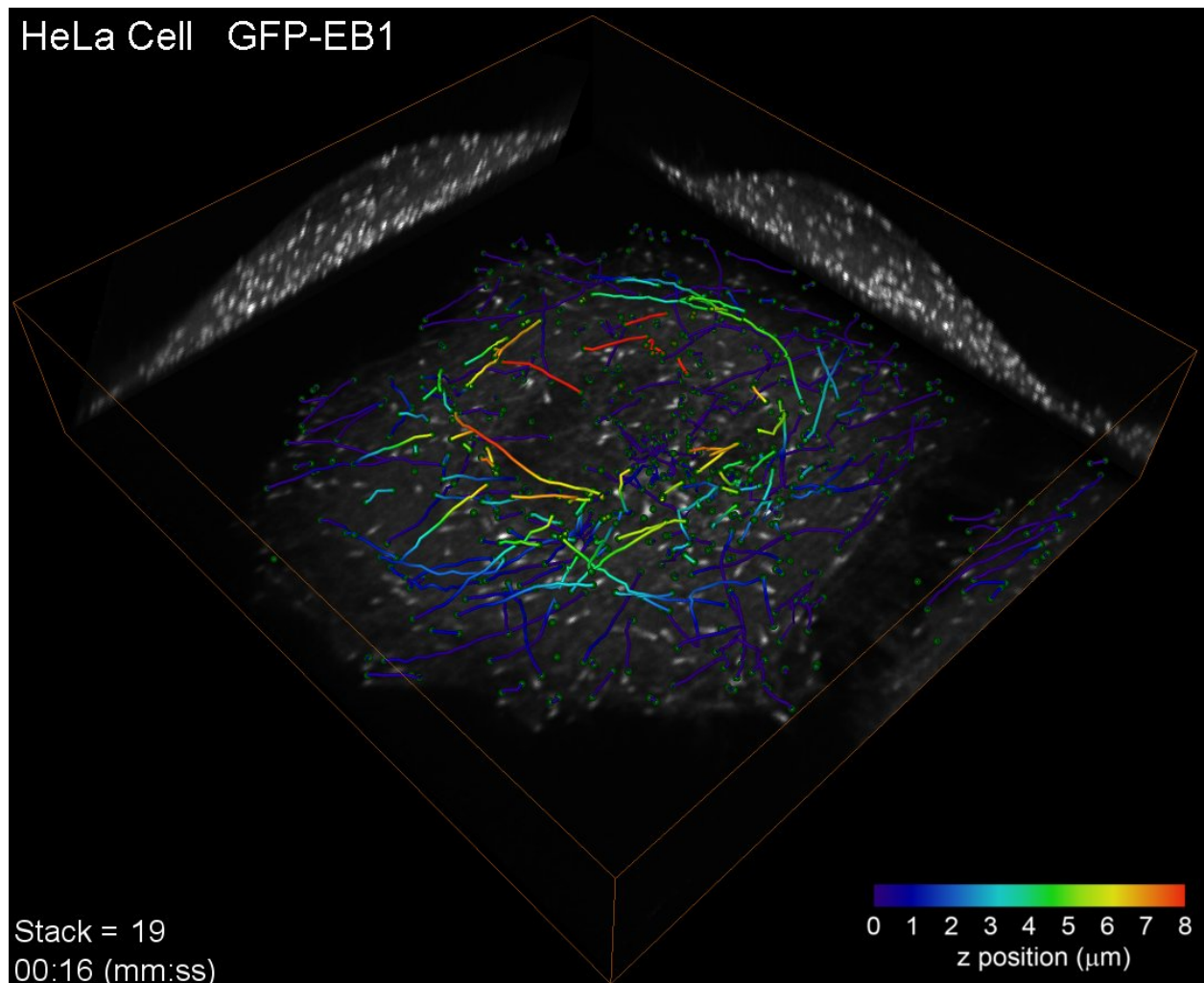
**Movie S8.** Single molecule tracking of TMR-labeled Sox2 transcription factors in an ~35  $\mu\text{m}$  diameter spheroid of mouse embryonic stem cells, as seen by a dithered lattice light sheet at a fixed plane (top), a single Bessel beam scanned across the same plane (middle), and widefield, epi-illumination across the entire specimen (bottom).



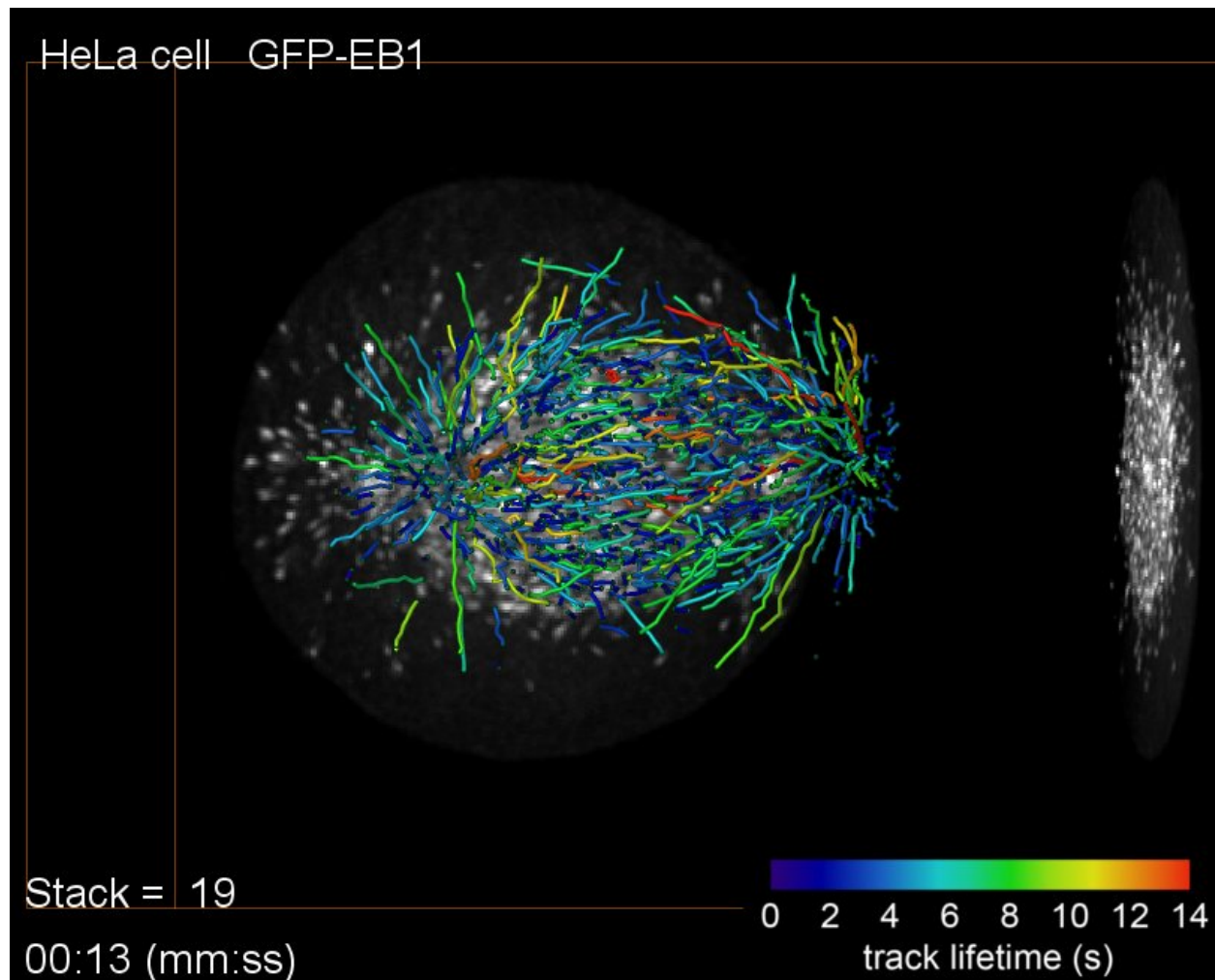
**Movie S9.** SNR as a function of exposure time when tracking single TMR-labeled Sox2 transcription factors in one plane across a stem cell spheroid illuminated by a dithered lattice light sheet.



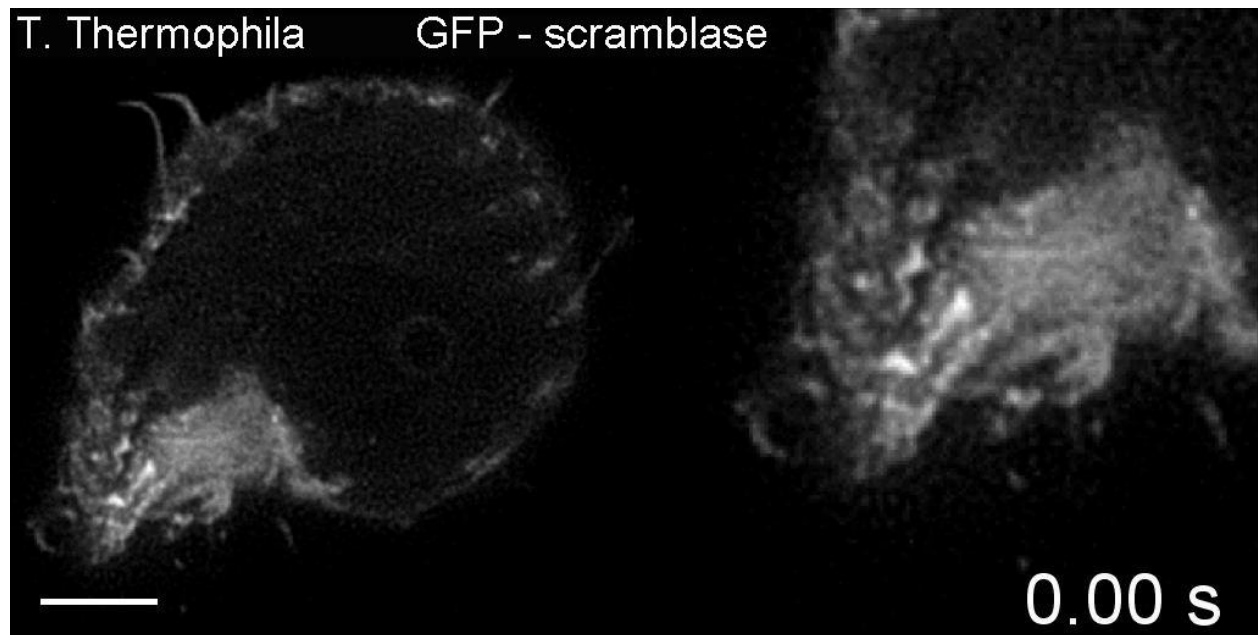
**Movie S10.** Orthoslices and volume renderings of the nuclear envelope of a U2OS cell labeled with Dendra2-lamin A as imaged by lattice-based super-resolution 3D PALM (left) and diffraction-limited lattice light sheet microscopy (right).



**Movie S11.** Maximum intensity projections and measured GFP-EB1 trajectories for a single HeLa cell in interphase. Growing microtubule endpoints and tracks are color coded by z-position above the substrate. Bounding box,  $47 \times 50 \times 11 \mu\text{m}$ .



**Movie S12.** Maximum intensity projections and measured GFP-EB1 trajectories for a single HeLa cell in metaphase. Growing microtubule endpoints and tracks are color coded by growth phase lifetime. Bounding box, 29 x 36 x 26  $\mu\text{m}$ .



**Movie S13.** Imaging *T. thermophila* expressing GFP-scramblase in a single 2D plane at 3 ms intervals reveals the motions of individual cilia (cf., fig. S10). Magnified view is shown at right.

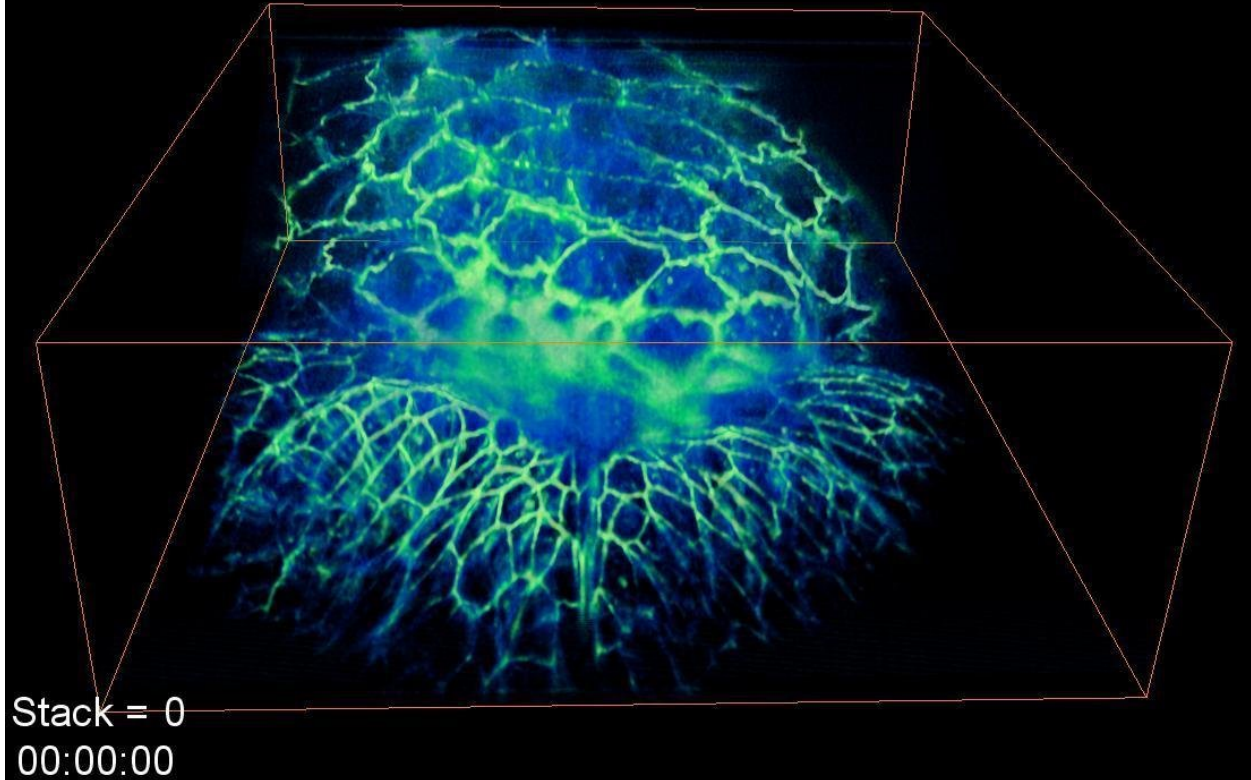


**Movie S14.** Top and oblique view volume rendering of the mutual chemotaxis of starved *D. discoideum* cells expressing RFP-LimE, marking their transition from unicellular to multicellular morphology (*cf.*, fig. S11).

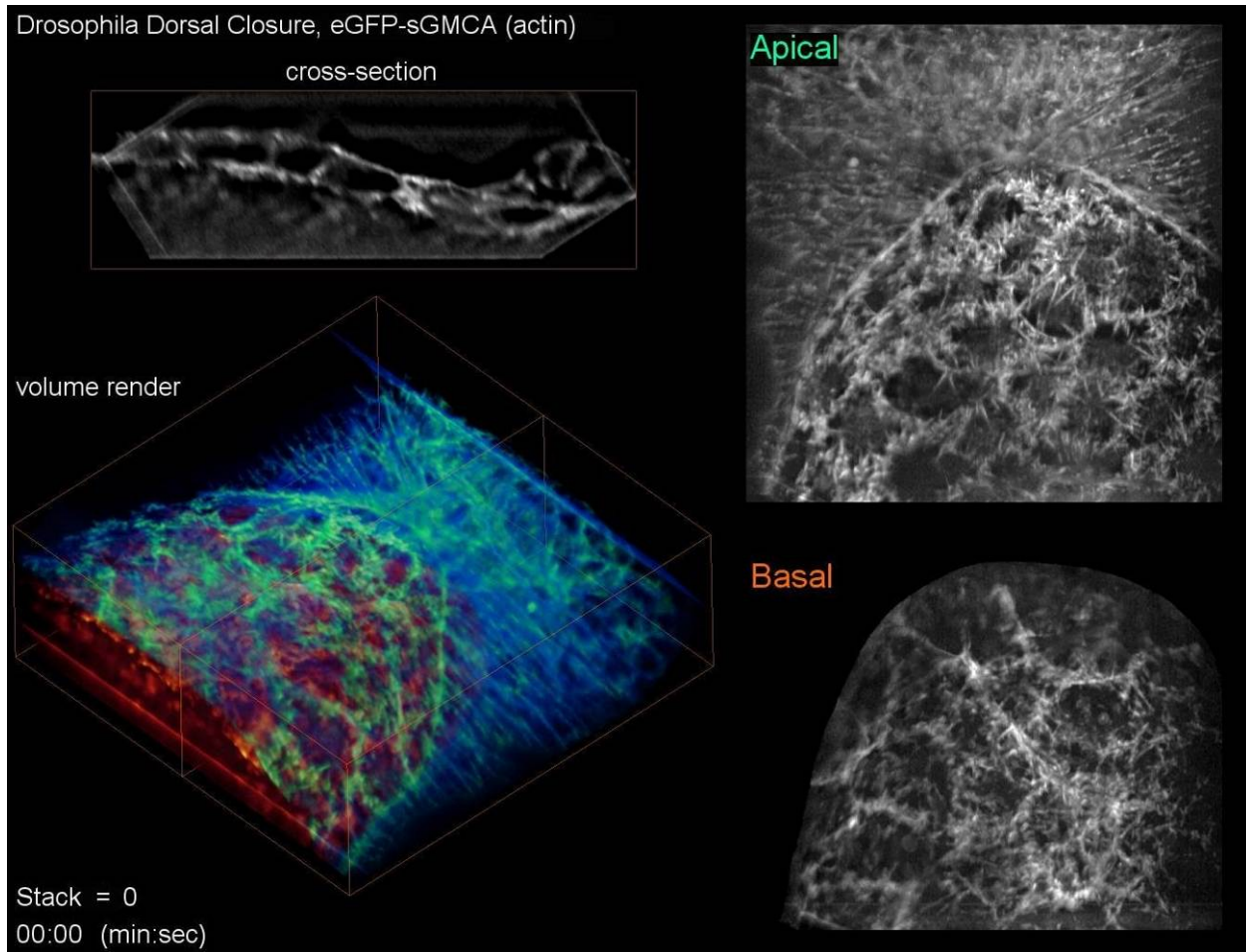


**Movie S15.** Volume rendering of GFP-PH domains (green) and mCherry-H2B (orange) in a *C. elegans* embryo at the three-fold stage, after the onset of muscle contractions. Bounding box, 41 x 39 x 60  $\mu\text{m}$ .

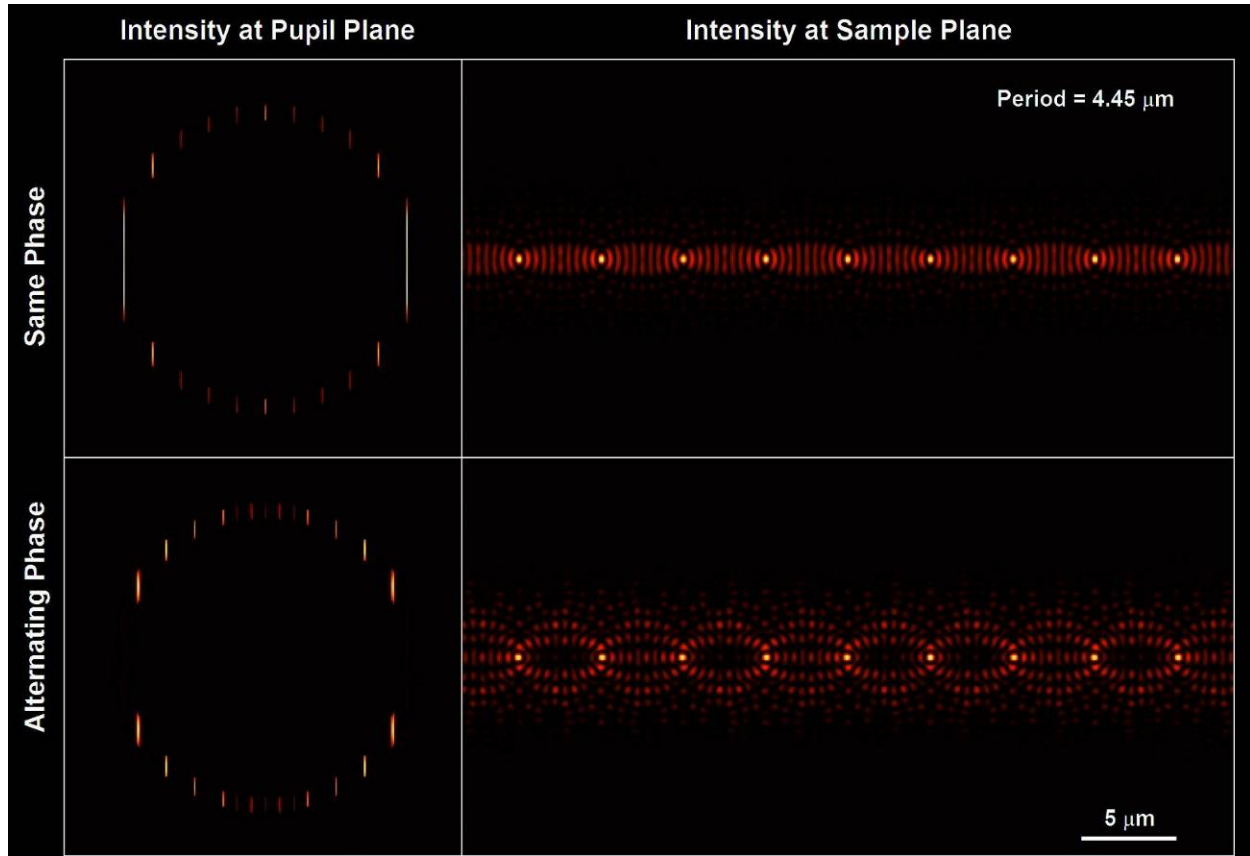
### Drosophila Dorsal Closure, eGFP - Cadherin



**Movie S16.** Volume rendering of the amnioserosa and the encroaching epithelium during dorsal closure in a *D. melanogaster* embryo expressing GFP/DE-cadherin to highlight cell-cell junctions, over 840 time points at 8 sec intervals (*cf.*, Fig. 6C). Bounding box, 86 x 80 x 31  $\mu\text{m}$ .



**Movie S17.** Various views of dorsal closure in a *D. melanogaster* embryo expressing sGMCA, a marker of filamentous actin at the plasma membrane, over 639 time points at 12.0 sec intervals. Top left: orthoslice through the center of the amnioserosa. Top right: maximum intensity projection through a thin rectangular slab encompassing the apical surface of the amnioserosa. Bottom right: MIP through a similar slab encompassing the basal surface of the amnioserosa. Bottom left, volume rendering, with the apical surface in blue/green and the basal surface in orange/red (cf., Fig. 6E, F). Bounding box, 73 x 73 x 26  $\mu\text{m}$ .



**Movie S18.** Rear pupil excitation pattern (left) and cross-sectional intensity at the sample (right) for a linear array of mutually interfering Bessel-Gauss beams, as a function of the period of the array. Top: all beams have the same phase; Bottom: adjacent beams have opposite phase.

## References and Notes

1. D. B. Murphy, M. W. Davidson, *Fundamentals of Light Microscopy and Electronic Imaging* (Wiley-Blackwell, Hoboken, NJ, ed. 2, 2013).
2. D. J. Stephens, V. J. Allan, Light microscopy techniques for live cell imaging. *Science* **300**, 82–86 (2003). [Medline doi:10.1126/science.1082160](#)
3. J. Huisken, D. Y. Stainier, Selective plane illumination microscopy techniques in developmental biology. *Development* **136**, 1963–1975 (2009). [Medline doi:10.1242/dev.022426](#)
4. J. Huisken, J. Swoger, F. Del Bene, J. Wittbrodt, E. H. Stelzer, Optical sectioning deep inside live embryos by selective plane illumination microscopy. *Science* **305**, 1007–1009 (2004). [Medline doi:10.1126/science.1100035](#)
5. U. Krzic, S. Gunther, T. E. Saunders, S. J. Streichan, L. Hufnagel, Multiview light-sheet microscope for rapid *in toto* imaging. *Nat. Methods* **9**, 730–733 (2012). [Medline doi:10.1038/nmeth.2064](#)
6. R. Tomer, K. Khairy, F. Amat, P. J. Keller, Quantitative high-speed imaging of entire developing embryos with simultaneous multiview light-sheet microscopy. *Nat. Methods* **9**, 755–763 (2012). [Medline doi:10.1038/nmeth.2062](#)
7. T. A. Planchon, L. Gao, D. E. Milkie, M. W. Davidson, J. A. Galbraith, C. G. Galbraith, E. Betzig, Rapid three-dimensional isotropic imaging of living cells using Bessel beam plane illumination. *Nat. Methods* **8**, 417–423 (2011). [Medline doi:10.1038/nmeth.1586](#)
8. L. Gao, L. Shao, C. D. Higgins, J. S. Poulton, M. Peifer, M. W. Davidson, X. Wu, B. Goldstein, E. Betzig, Noninvasive imaging beyond the diffraction limit of 3D dynamics in thickly fluorescent specimens. *Cell* **151**, 1370–1385 (2012). [Medline doi:10.1016/j.cell.2012.10.008](#)
9. M. G. Gustafsson, L. Shao, P. M. Carlton, C. J. Wang, I. N. Golubovskaya, W. Z. Cande, D. A. Agard, J. W. Sedat, Three-dimensional resolution doubling in wide-field fluorescence microscopy by structured illumination. *Biophys. J.* **94**, 4957–4970 (2008). [Medline doi:10.1529/biophysj.107.120345](#)
10. R. Gräf, J. Rietdorf, T. Zimmermann, Live cell spinning disk microscopy. *Adv. Biochem. Eng. Biotechnol.* **95**, 57–75 (2005). [Medline doi:10.1007/b102210](#)
11. E. Betzig, Sparse and composite coherent lattices. *Phys. Rev. A* **71**, 063406 (2005). [doi:10.1103/PhysRevA.71.063406](#)
12. K. I. Petsas, A. B. Coates, G. Grynberg, Crystallography of optical lattices. *Phys. Rev. A* **50**, 5173–5189 (1994). [Medline doi:10.1103/PhysRevA.50.5173](#)
13. I. Bloch, Ultracold quantum gases in optical lattices. *Nat. Phys.* **1**, 23–30 (2005). [doi:10.1038/nphys138](#)
14. M. Campbell, D. N. Sharp, M. T. Harrison, R. G. Denning, A. J. Turberfield, Fabrication of photonic crystals for the visible spectrum by holographic lithography. *Nature* **404**, 53–56 (2000). [Medline doi:10.1038/35003523](#)

15. E. Betzig, Excitation strategies for optical lattice microscopy. *Opt. Express* **13**, 3021–3036 (2005). [Medline doi:10.1364/OPEX.13.003021](#)
16. I. Tikhonenko, D. K. Nag, D. N. Robinson, M. P. Koonce, Microtubule-nucleus interactions in *Dictyostelium discoideum* mediated by central motor kinesins. *Eukaryot. Cell* **8**, 723–731 (2009). [Medline doi:10.1128/EC.00018-09](#)
17. G. Jung, M. A. Titus, J. A. Hammer 3rd, The *Dictyostelium* type V myosin MyoJ is responsible for the cortical association and motility of contractile vacuole membranes. *J. Cell Biol.* **186**, 555–570 (2009). [Medline doi:10.1083/jcb.200810147](#)
18. S. Diez, G. Gerisch, K. Anderson, A. Müller-Taubenberger, T. Bretschneider, Subsecond reorganization of the actin network in cell motility and chemotaxis. *Proc. Natl. Acad. Sci. U.S.A.* **102**, 7601–7606 (2005). [Medline doi:10.1073/pnas.0408546102](#)
19. M. Coelho, N. Maghelli, I. M. Tolić-Nørrelykke, Single-molecule imaging in vivo: The dancing building blocks of the cell. *Integr. Biol.* **5**, 748–758 (2013). [Medline doi:10.1039/c3ib40018b](#)
20. J. G. Ritter, R. Veith, J. P. Siebrasse, U. Kubitscheck, High-contrast single-particle tracking by selective focal plane illumination microscopy. *Opt. Express* **16**, 7142–7152 (2008). [Medline doi:10.1364/OE.16.007142](#)
21. M. Tokunaga, N. Imamoto, K. Sakata-Sogawa, Highly inclined thin illumination enables clear single-molecule imaging in cells. *Nat. Methods* **5**, 159–161 (2008). [Medline doi:10.1038/nmeth1171](#)
22. J. Chen, Z. Zhang, L. Li, B. C. Chen, A. Revyakin, B. Hajj, W. Legant, M. Dahan, T. Lionnet, E. Betzig, R. Tjian, Z. Liu, Single-molecule dynamics of enhanceosome assembly in embryonic stem cells. *Cell* **156**, 1274–1285 (2014). [Medline doi:10.1016/j.cell.2014.01.062](#)
23. J. C. Gebhardt, D. M. Suter, R. Roy, Z. W. Zhao, A. R. Chapman, S. Basu, T. Maniatis, X. S. Xie, Single-molecule imaging of transcription factor binding to DNA in live mammalian cells. *Nat. Methods* **10**, 421–426 (2013). [Medline doi:10.1038/nmeth.2411](#)
24. E. Betzig, Proposed method for molecular optical imaging. *Opt. Lett.* **20**, 237–239 (1995). [Medline doi:10.1364/OL.20.000237](#)
25. F. Celli Zanacchi, Z. Lavagnino, M. Perrone Donnorso, A. Del Bue, L. Furia, M. Fareta, A. Diaspro, Live-cell 3D super-resolution imaging in thick biological samples. *Nat. Methods* **8**, 1047–1049 (2011). [Medline doi:10.1038/nmeth.1744](#)
26. M. Speidel, A. Jonás, E. L. Florin, Three-dimensional tracking of fluorescent nanoparticles with subnanometer precision by use of off-focus imaging. *Opt. Lett.* **28**, 69–71 (2003). [Medline doi:10.1364/OL.28.000069](#)
27. H. P. Kao, A. S. Verkman, Tracking of single fluorescent particles in three dimensions: Use of cylindrical optics to encode particle position. *Biophys. J.* **67**, 1291–1300 (1994). [Medline doi:10.1016/S0006-3495\(94\)80601-0](#)
28. E. Betzig, G. H. Patterson, R. Sougrat, O. W. Lindwasser, S. Olenych, J. S. Bonifacino, M. W. Davidson, J. Lippincott-Schwartz, H. F. Hess, Imaging intracellular fluorescent

- proteins at nanometer resolution. *Science* **313**, 1642–1645 (2006). [Medline](#) [doi:10.1126/science.1127344](#)
29. J. Ellenberg, E. D. Siggia, J. E. Moreira, C. L. Smith, J. F. Presley, H. J. Worman, J. Lippincott-Schwartz, Nuclear membrane dynamics and reassembly in living cells: Targeting of an inner nuclear membrane protein in interphase and mitosis. *J. Cell Biol.* **138**, 1193–1206 (1997). [Medline](#) [doi:10.1083/jcb.138.6.1193](#)
30. Y. Mimori-Kiyosue, N. Shiina, S. Tsukita, The dynamic behavior of the APC-binding protein EB1 on the distal ends of microtubules. *Curr. Biol.* **10**, 865–868 (2000). [Medline](#) [doi:10.1016/S0960-9822\(00\)00600-X](#)
31. K. T. Applegate, S. Besson, A. Matov, M. H. Bagonis, K. Jaqaman, G. Danuser, plusTipTracker: Quantitative image analysis software for the measurement of microtubule dynamics. *J. Struct. Biol.* **176**, 168–184 (2011). [Medline](#) [doi:10.1016/j.jsb.2011.07.009](#)
32. A. Khodjakov, C. L. Rieder, Imaging the division process in living tissue culture cells. *Methods* **38**, 2–16 (2006). [Medline](#) [doi:10.1016/j.ymeth.2005.07.007](#)
33. N. Taguchi, N. Ishihara, A. Jofuku, T. Oka, K. Mihara, Mitotic phosphorylation of dynamin-related GTPase Drp1 participates in mitochondrial fission. *J. Biol. Chem.* **282**, 11521–11529 (2007). [Medline](#) [doi:10.1074/jbc.M607279200](#)
34. L. Lu, M. S. Ladinsky, T. Kirchhausen, Cisternal organization of the endoplasmic reticulum during mitosis. *Mol. Biol. Cell* **20**, 3471–3480 (2009). [Medline](#) [doi:10.1091/mbc.E09-04-0327](#)
35. D. Wloga, J. Frankel, From molecules to morphology: Cellular organization of *Tetrahymena thermophila*. *Methods Cell Biol.* **109**, 83–140 (2012). [Medline](#) [doi:10.1016/B978-0-12-385967-9.00005-0](#)
36. A. T. Ritter, K. L. Angus, G. M. Griffiths, The role of the cytoskeleton at the immunological synapse. *Immunol. Rev.* **256**, 107–117 (2013).
37. D. Dormann, C. J. Weijer, Imaging of cell migration. *EMBO J.* **25**, 3480–3493 (2006). [Medline](#) [doi:10.1038/sj.emboj.7601227](#)
38. P. H. Wu, A. Giri, S. X. Sun, D. Wirtz, Three-dimensional cell migration does not follow a random walk. *Proc. Natl. Acad. Sci. U.S.A.* **111**, 3949–3954 (2014). [Medline](#) [doi:10.1073/pnas.1318967111](#)
39. P. Friedl, S. Borgmann, E. B. Bröcker, Amoeboid leukocyte crawling through extracellular matrix: Lessons from the *Dictyostelium* paradigm of cell movement. *J. Leukoc. Biol.* **70**, 491–509 (2001). [Medline](#)
40. A. B. Hauert, S. Martinelli, C. Marone, V. Niggli, Differentiated HL-60 cells are a valid model system for the analysis of human neutrophil migration and chemotaxis. *Int. J. Biochem. Cell Biol.* **34**, 838–854 (2002). [Medline](#) [doi:10.1016/S1357-2725\(02\)00010-9](#)
41. W. R. Legant, J. S. Miller, B. L. Blakely, D. M. Cohen, G. M. Genin, C. S. Chen, Measurement of mechanical tractions exerted by cells in three-dimensional matrices. *Nat. Methods* **7**, 969–971 (2010). [Medline](#) [doi:10.1038/nmeth.1531](#)

42. J. N. Bembenek, K. J. Verbrugghe, J. Khanikar, G. Csankovszki, R. C. Chan, Condensin and the spindle midzone prevent cytokinesis failure induced by chromatin bridges in *C. elegans* embryos. *Curr. Biol.* **23**, 937–946 (2013). [Medline](#) [doi:10.1016/j.cub.2013.04.028](#)
43. J. M. Schumacher, A. Golden, P. J. Donovan, AIR-2: An Aurora/Ipl1-related protein kinase associated with chromosomes and midbody microtubules is required for polar body extrusion and cytokinesis in *Caenorhabditis elegans* embryos. *J. Cell Biol.* **143**, 1635–1646 (1998). [Medline](#) [doi:10.1083/jcb.143.6.1635](#)
44. M. Carmena, W. C. Earnshaw, The cellular geography of aurora kinases. *Nat. Rev. Mol. Cell Biol.* **4**, 842–854 (2003). [Medline](#) [doi:10.1038/nrm1245](#)
45. N. Velarde, K. C. Gunsalus, F. Piano, Diverse roles of actin in *C. elegans* early embryogenesis. *BMC Dev. Biol.* **7**, 142 (2007). [Medline](#) [doi:10.1186/1471-213X-7-142](#)
46. S. W. Grill, Growing up is stressful: Biophysical laws of morphogenesis. *Curr. Opin. Genet. Dev.* **21**, 647–652 (2011). [Medline](#) [doi:10.1016/j.gde.2011.09.005](#)
47. A. Sokolow, Y. Toyama, D. P. Kiehart, G. S. Edwards, Cell ingression and apical shape oscillations during dorsal closure in *Drosophila*. *Biophys. J.* **102**, 969–979 (2012). [Medline](#) [doi:10.1016/j.bpj.2012.01.027](#)
48. K. Wang, D. E. Milkie, A. Saxena, P. Engerer, T. Misgeld, M. E. Bronner, J. Mumm, E. Betzig, Rapid adaptive optical recovery of optimal resolution over large volumes. *Nat. Methods* **11**, 625–628 (2014). [Medline](#) [doi:10.1038/nmeth.2925](#)
49. G. Donnert, C. Eggeling, S. W. Hell, Major signal increase in fluorescence microscopy through dark-state relaxation. *Nat. Methods* **4**, 81–86 (2007). [Medline](#) [doi:10.1038/nmeth986](#)
50. N. Ji, J. C. Magee, E. Betzig, High-speed, low-photodamage nonlinear imaging using passive pulse splitters. *Nat. Methods* **5**, 197–202 (2008). [Medline](#) [doi:10.1038/nmeth.1175](#)
51. T. Shimozawa, K. Yamagata, T. Kondo, S. Hayashi, A. Shitamukai, D. Konno, F. Matsuzaki, J. Takayama, S. Onami, H. Nakayama, Y. Kosugi, T. M. Watanabe, K. Fujita, Y. Mimori-Kiyosue, Improving spinning disk confocal microscopy by preventing pinhole cross-talk for intravital imaging. *Proc. Natl. Acad. Sci. U.S.A.* **110**, 3399–3404 (2013). [Medline](#) [doi:10.1073/pnas.1216696110](#)
52. J. D. Sander, J. K. Joung, CRISPR-Cas systems for editing, regulating and targeting genomes. *Nat. Biotechnol.* **32**, 347–355 (2014). [Medline](#) [doi:10.1038/nbt.2842](#)
53. T. Zimmermann, J. Rieddorf, R. Pepperkok, Spectral imaging and its applications in live cell microscopy. *FEBS Lett.* **546**, 87–92 (2003). [Medline](#) [doi:10.1016/S0014-5793\(03\)00521-0](#)
54. J. Livet, T. A. Weissman, H. Kang, R. W. Draft, J. Lu, R. A. Bennis, J. R. Sanes, J. W. Lichtman, Transgenic strategies for combinatorial expression of fluorescent proteins in the nervous system. *Nature* **450**, 56–62 (2007). [Medline](#) [doi:10.1038/nature06293](#)
55. E. Lubeck, L. Cai, Single-cell systems biology by super-resolution imaging and combinatorial labeling. *Nat. Methods* **9**, 743–748 (2012). [Medline](#) [doi:10.1038/nmeth.2069](#)

56. A. M. Valm, J. L. Mark Welch, C. W. Rieken, Y. Hasegawa, M. L. Sogin, R. Oldenbourg, F. E. Dewhirst, G. G. Borisy, Systems-level analysis of microbial community organization through combinatorial labeling and spectral imaging. *Proc. Natl. Acad. Sci. U.S.A.* **108**, 4152–4157 (2011). [Medline doi:10.1073/pnas.1101134108](#)
57. L. Gao, L. Shao, B. C. Chen, E. Betzig, 3D live fluorescence imaging of cellular dynamics using Bessel beam plane illumination microscopy. *Nat. Protoc.* **9**, 1083–1101 (2014). [Medline doi:10.1038/nprot.2014.087](#)
58. B. P. English, V. Hauryliuk, A. Sanamrad, S. Tankov, N. H. Dekker, J. Elf, Single-molecule investigations of the stringent response machinery in living bacterial cells. *Proc. Natl. Acad. Sci. U.S.A.* **108**, E365–E373 (2011). [Medline doi:10.1073/pnas.1102255108](#)
59. J. Durnin, J. J. Miceli Jr., J. H. Eberly, Comparison of Bessel and Gaussian beams. *Opt. Lett.* **13**, 79 (1988). [Medline doi:10.1364/OL.13.000079](#)
60. B. Richards, E. Wolf, Electromagnetic diffraction in optical systems. 2. Structure of the image field in an aplanatic system. *Proc. R. Soc. London Ser. A* **253**, 358–379 (1959). [doi:10.1098/rspa.1959.0200](#)
61. P. Kner, B. B. Chhun, E. R. Griffis, L. Winoto, M. G. Gustafsson, Super-resolution video microscopy of live cells by structured illumination. *Nat. Methods* **6**, 339–342 (2009). [Medline doi:10.1038/nmeth.1324](#)
62. S. Nakamura, I. Grigoriev, T. Nogi, T. Hamaji, L. Cassimeris, Y. Mimori-Kiyosue, Dissecting the nanoscale distributions and functions of microtubule-end-binding proteins EB1 and ch-TOG in interphase HeLa cells. *PLOS ONE* **7**, e51442 (2012). [Medline doi:10.1371/journal.pone.0051442](#)
63. C. Demaison, K. Parsley, G. Brouns, M. Scherr, K. Battmer, C. Kinnon, M. Grez, A. J. Thrasher, High-level transduction and gene expression in hematopoietic repopulating cells using a human immunodeficiency virus type 1-based lentiviral vector containing an internal spleen focus forming virus promoter. *Hum. Gene Ther.* **13**, 803–813 (2002). [Medline doi:10.1089/10430340252898984](#)
64. B. M. Burkel, G. von Dassow, W. M. Bement, Versatile fluorescent probes for actin filaments based on the actin-binding domain of utrophin. *Cell Motil. Cytoskeleton* **64**, 822–832 (2007). [Medline doi:10.1002/cm.20226](#)
65. M. Sixt, T. Lämmermann, In vitro analysis of chemotactic leukocyte migration in 3D environments. *Methods Mol. Biol.* **769**, 149–165 (2011). [Medline doi:10.1007/978-1-61779-207-6\\_11](#)
66. E. Octaviani, J. C. Effler, D. N. Robinson, Enlazin, a natural fusion of two classes of canonical cytoskeletal proteins, contributes to cytokinesis dynamics. *Mol. Biol. Cell* **17**, 5275–5286 (2006). [Medline doi:10.1091/mbc.E06-08-0767](#)
67. M. Clarke, A. Müller-Taubenberger, K. I. Anderson, U. Engel, G. Gerisch, Mechanically induced actin-mediated rocketing of phagosomes. *Mol. Biol. Cell* **17**, 4866–4875 (2006). [Medline doi:10.1091/mbc.E06-04-0365](#)
68. A. Essex, A. Dammermann, L. Lewellyn, K. Oegema, A. Desai, Systematic analysis in *Caenorhabditis elegans* reveals that the spindle checkpoint is composed of two largely

- independent branches. *Mol. Biol. Cell* **20**, 1252–1267 (2009). [Medline](#)  
[doi:10.1091/mbc.E08-10-1047](#)
69. H. Oda, S. Tsukita, Real-time imaging of cell-cell adherens junctions reveals that *Drosophila* mesoderm invagination begins with two phases of apical constriction of cells. *J. Cell Sci.* **114**, 493–501 (2001). [Medline](#)
70. P. A. Lawrence, R. Bodmer, J. P. Vincent, Segmental patterning of heart precursors in *Drosophila*. *Development* **121**, 4303–4308 (1995). [Medline](#)
71. M. Buszczak, S. Paterno, D. Lighthouse, J. Bachman, J. Planck, S. Owen, A. D. Skora, T. G. Nystul, B. Ohlstein, A. Allen, J. E. Wilhelm, T. D. Murphy, R. W. Levis, E. Matunis, N. Srivalli, R. A. Hoskins, A. C. Spradling, The carnegie protein trap library: A versatile tool for *Drosophila* developmental studies. *Genetics* **175**, 1505–1531 (2007). [Medline](#)  
[doi:10.1534/genetics.106.065961](#)
72. K. A. Edwards, M. Demsky, R. A. Montague, N. Weymouth, D. P. Kiehart, GFP-moesin illuminates actin cytoskeleton dynamics in living tissue and demonstrates cell shape changes during morphogenesis in *Drosophila*. *Dev. Biol.* **191**, 103–117 (1997). [Medline](#)  
[doi:10.1006/dbio.1997.8707](#)
73. A. C. Martin, M. Kaschube, E. F. Wieschaus, Pulsed contractions of an actin-myosin network drive apical constriction. *Nature* **457**, 495–499 (2009). [Medline](#)  
[doi:10.1038/nature07522](#)